Validation of clinical image quantification and dosimetry using 3D printed anthropomorphic phantoms

A thesis submitted to the University of Manchester for the degree of Doctor of Philosophy in the Faculty of Science and Engineering

2019

Emlyn Price

School of Physics and Astronomy
The University of Manchester

The remainder of this page was intentionally left blank.

Contents

Final word count: 23043

The remainder of this page was intentionally left blank.

List of Figures

List of Tables

The remainder of this page was intentionally left blank.

Abbreviations

ABS	**A**crylonitrile **B**utadiene **S**tyrene
AC	**A**ttenuation **C**orrection
AIC	**A**kaike **I**nformation **C**riterion
AICc	**c**orrected **A**kaike **I**nformation **C**riterion
ACSC	**A**ttenuation **C**orrection and **S**catter **C**orrection
CAD	**C**omputer **A**ided **D**esign
CATIE	**C**hristie **A**nthropomorphic **T**omographic **I**maging **E**llipse
CT	**C**omputed **T**omography
DDSR	**D**epth **D**ependent **S**patial **R**esolution
FWHM	**F**ull **W**idth at **H**alf **M**aximum
GUM	**G**uide to the expression of **U**ncertainty in **M**easurement
GATE	**G**eant4 **A**pplication for **T**omographic **E**mission
LEHR	**L**ow **E**nergy **H**igh **R**esolution
MEGP	**M**edium **E**nergy **G**eneral **P**urpose
MRT	**M**olecular **R**adio**T**herapy
MCSC	**M**onte **C**arlo **S**catter **C**orrection
NEMA	**N**ational **E**lectrical **M**anufacturers **A**ssociation
NPL	**N**ational **P**hysical **L**aboratory
OSEM	**O**rdered **S**ubset **E**xpectation **M**aximisation
PDF	**P**robability **D**ensity **F**unction
PET	**P**ositron **E**mission **T**omography
PHA	**P**ulse **H**eight **A**nalysis
PLA	**P**oly**L**actic **A**cid
PMT	**P**hoto**M**ultiplier **T**ube
PRRT	**P**eptide **R**eceptor **R**adionuclide **T**herapy

ROI	**R**egion **O**f **I**nterest
SC	**S**catter **C**orrection
STL	**ST**ereo**L**ithography
SPECT	**S**ingle **P**hoton **E**mission **C**omputed **T**omography
TAC	**T**ime **A**ctivity **C**urve
TEW	**T**riple **E**nergy **W**indow
VOI	**V**olume **O**f **I**nterest

Abstract

Patient-specific image quantification and dosimetry are vital to optimise the delivery of molecular radiotherapy. This thesis describes the validation of image quantification using 3D printed patient-specific organ models and Monte Carlo simulations of radiation transport to calculate radiation dose. In order to calculate the radiation dose to an organ the curve describing the activity in an organ over time must be integrated. The impact of experimental noise on curve fitting in nuclear medicine is demonstrated using artificial sets of imaging data.

A set of patient-specific 3D printed organ models, comprising the liver spleen and both kidneys, based on a diagnostic CT scan, was produced. Patient-specific calibration factors for ^{177}Lu were calculated. These patient-specific calibration factors were compared to those previously reported for organ models based on the Cristy and Eckerman phantom series and a 113 ml sphere. Overestimations of recovered activity and hence dose of up to 135 % are shown. The calculation of calibration factors revealed a dependence on the position of the insert. The source of this position dependence was determined to result from the application attenuation correction. Users of reconstruction systems must ensure that the behaviour of attenuation correction on their system is understood.

Patient-specific dosimetry calculations were compared to clinical tools for ^{177}Lu and ^{131}I. These calculations demonstrate the consistency of clinical methods for ^{177}Lu if mass scaling is applied to the generic calculations. Inconsistencies in the calculations are present for ^{131}I due to the greater contribution of gamma rays to the radiation dose.

Summed exponential functions are often used to describe the activity in an organ over time. However these functions are fundamentally hard to fit to data points due to their mathematical structure. Artificial data sets representing measurements of the activity in organs over time were generated and curves fitted to them. Calculations of the area under these curves demonstrates the difficulty in fitting and calculation of uncertainty as applied to nuclear medicine.

The work on anthropomorphic calibration factors is published in Physica Medica. A paper describing the examination of the positional dependence is published in Nuclear Medicine Communications.

Declaration of Authorship

I, Emlyn Price, confirm that no portion of the work referred to in the thesis has been submitted in support of an application for another degree or qualification of this or any other university or other institute of learning.

Copyright statement

"They don't think it be like it is, but it do."

Oscar Gamble

Acknowledgements

First I would like to thank Jill, Dave C., Andrew, Ben and Dave H. for their support throughout the project. Chris, Sophia and Emma have been a great help discussing problems and debugging software. Thanks as well to those who spent many evenings filling phantoms and performing SPECT scans at the Christie.

To the other nuclear physics students, thanks for the friendship.

Finally, thanks to my family for their constant support.

The remainder of this page was intentionally left blank.

Chapter 1

Introduction

This chapter first provides a brief overview of Molecular Radiotherapy (MRT) and the work done in this thesis. Then, background information to the thesis is discussed in detail.

1.1 Overview

Molecular Radiotherapy is a form of cancer therapy in which a radiolabelled pharmaceutical is injected into a patient. The radiopharmaceutical is chosen such that it is taken up by specific tumours and organs with minimal uptake in other organs. After administration each patient will have a different uptake and distribution of radioactive material throughout their body. In order to calculate the radiation dose the patient has received, the activity distribution must be quantified for each patient. This quantification is done using external imaging. The imaging devices used must be calibrated to relate the detected radiation to the activity distribution in the patient. Clinically, simple geometries such as spheres and cylinders are used to calibrate the detector [1]. These are not patient-specific and therefore may not provide optimal calibration.

3D printing allows the imaging of known, patient-representative, activity distributions which can be used to assess the accuracy of clinical imaging. The activity distribution is then used to calculate the radiation dose distribution. This requires the total number of decays in each source region to be calculated, by fitting decay curves to multiple measurements of the patient activity distribution. Then the total number of decays in a given source region is related to the dose in a target region. Direct Monte Carlo simulation of dose deposition allows an assessment of the models used clinically to relate the number of decays to radiation dose.

The quantification of activity distributions of ^{177}Lu solution using 3D printed patient-specific phantoms is examined in Chapter 3. Patient-specific dosimetry is compared to a standard clinical method. An unexpected dependence of quantification on position is then investigated in Chapter 4. Finally, the impact of uncertainties and errors in the quantitative imaging and dosimetry processes on the calculated dose is assessed in Chapter 5.

1.2 Molecular Radiotherapy

In MRT a radionuclide is typically bound to a chemical, a radioligand, which is taken up by a specific type of cell. The choice of radioligand is informed by the type of cell to be treated and the chemistry of the radionuclide. The radionuclide is chosen based on its decay properties and half life. Targeting cell types in this way allows high radiation doses to be delivered to abnormal cells while minimising damage to healthy tissue. For example sodium iodide is administered to treat thyroid cells, and complex octreotide molecules such as DOTATATE may be used for neuroendocrine tumours [2]. In cancer treatment this type of therapy has the advantage that any metastatic tumours around the body will take up the isotope. The drawback of such treatments is that the radiation dose distribution in the patient must be calculated using external imaging. The dose distribution is calculated to ensure that the dose to healthy organs is minimised and does not exceed pre-determined dose limits. The dose to tumours must be high enough to result in cell death. These two requirements must be balanced during the treatment process [3]. Calculating the dose distribution after treatment is in contrast to external beam radiotherapy in which the dose distribution is planned ahead of time. However, external beam radiotherapy is not suitable for targeting multiple small objects located around the body.

The choice of radionuclide is made based on the purpose of the imaging or therapy and the chemical properties for binding to a suitable radioligand. If the isotope is to be used for imaging it must emit gamma rays or positrons. These emissions are chosen as most gamma rays will escape the patient without depositing a large amount of energy, minimising dose and allowing external imaging. Single Photon Emission Computed Tomography (SPECT) is used to image photons emitted in gamma decay and Positron Emission Tomography (PET) is used to image back-to-back 511 keV gamma rays from annihilation of positrons [4, 5]. For therapeutic uses the aim is to maximise the dose to diseased cells while minimising the dose to healthy tissue and beta or alpha emitters are used. The radioactive half-life of the isotope must be appropriate for the imaging and therapy process. The energy of the emitted decay radiation must be appropriate for

the imaging and/or therapy being performed. For SPECT imaging, the photon energy must be reliably detectable by a gamma camera. In therapy the required energy of decay radiation is related to the range required to deliver the dose [3]. For both uses the decays of any unstable daughter nuclides must be considered. Table 1.1 shows a selection of radionuclides used in MRT and the vector they are used with to target particular diseases.

TABLE 1.1: A selection of radionuclides used in molecular radiotherapy. The information in this table is taken from [6].

Nuclide	Vector	Indication
^{131}I	Iodide	Thyroid
^{89}Sr	Chloride	Bone metastases
^{131}I	mIBG	Neuroendocrine disease
^{90}Y	microspheres	Hepatic malignancy
^{223}Ra	dichloride	Bone metastases in castration-resistant prostate cancer
^{177}Lu	DOTATATE	Neuroendocrine tumours
^{177}Lu	DOTANOC	Somatostatin expressing tumours

One of the earliest uses of external imaging in MRT was administering ^{131}I to a patient and measuring the count rate near the thyroid with a Geiger counter [4]. This concept was then extended to rectilinear scanners which moved a scintillation detector across a patient. The gamma camera, invented by Hal Anger, uses a single large scintillation crystal in front of an array of photomultiplier tubes (PMTs) [4]. Gamma rays interact in the scintillation crystal which emits optical photons. The PMTs then detect the optical photons. Anger arithmetic is used to calculate the position of the interaction in the crystal using the output of the PMT array. An image is built up from the calculated positions [4]. Gamma cameras may be rotated around a patient and the images collected reconstructed to give a 3D image. This process is known as SPECT. Modern SPECT scanners are often operated along with an X-ray computed tomography (CT) scanner to perform hybrid imaging. A photograph of a GE Infinia Hawkeye 4 scanner is shown in Figure 1.1. The SPECT images provide functional information about the distribution of a radionuclide and the CT image provides anatomical information [4]. The details of SPECT imaging are discussed in Section 2.3. Each image provides a measurement of a snapshot of the distribution of activity in the patient. The distribution varies over time as the radionuclide decays and the radiopharmaceutical is metabolised and excreted. The rates of uptake and excretion of a radiopharmaceutical very significantly between patients, so images are acquired at multiple time points. In order to calculate the radiation dose resulting from the radioactivity in an organ, the total number of radioactive decays in that organ must be calculated. The calculation of dose is discussed in Section 2.5.2. The total number of decays in a region must be calculated by numeric integration or fitting a function to the data points and then integrating. Section 5.2 examines the calculation of the number of decays by fitting a function to data from a series of time points.

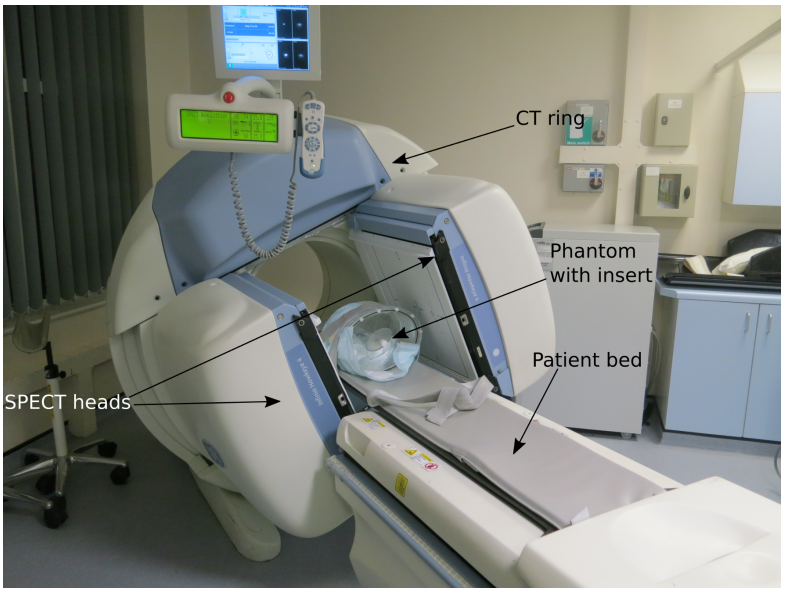

FIGURE 1.1: A photograph of the GE Infinia Hawkeye 4 scanner at the Christie Hospital. The SPECT heads, CT housing and patient bed are labelled. An elliptical Jaszczak phantom containing a 3D printed model of a generic spleen is being imaged.

This thesis focuses on the imaging and dosimetry involved in the treatment of neuroendocrine tumours using ^{177}Lu peptide receptor radionuclide therapy (PRRT). The ^{177}Lu is typically bound to DOTATATE or DOTATOC molecules. Typically, all patients are injected with 7.4 GBq of ^{177}Lu with four to six treatment cycles. The kidneys are particularly at risk in these therapies and dose limits of 23 Gy or 27 Gy to the kidneys are generally set [7]. The administration of a standard activity results in a wide range of absorbed doses to organs at risk in different patients, for instance from 14 Gy to 32 Gy to the kidneys [8]. Generally, the uncertainties involved in the measurements associated with MRT are not considered [9]. Reference [10] states that the uncertainty on dose estimates is typically a factor of two. Reference [10] also suggests that the uncertainty may perhaps be reduced to between 10 and 20 % if model-based uncertainties around data acquisition, analysis and processing are removed.

1.3 Phantoms in MRT

Phantoms are test objects used in MRT to provide a known activity distribution. They are required to perform quality control or to calibrate the scanner. There are six interrelated parameters which characterise the performance of a gamma camera: spatial resolution, non-uniformity, spatial distortion, sensitivity, count rate characteristic and energy resolution. Phantoms are used to measure these characteristics. For instance line sources such as capillary tubes are used to measure the resolution of the scanner and assess spatial distortion. Non-uniformity is assessed by filling the detector field of view

with a large plane source. Sensitivity is measured by acquiring images of a source with known activity. The count rate characteristic is calculated by measuring the count rate from a source of a known activity as the source decays. The energy resolution is measured by measuring the energy spectrum of emissions from a source and fitting Gaussian peaks to the known emissions [11]. Quality control is done at regular intervals as part of the clinical operation of the scanner. Commercial phantoms are often simple geometric objects such as cylinders, elliptical cylinders and spheres (e.g the Jaszczak phantom series [12] and the NEMA image quality phantom [13]), although anthropomorphic phantoms are available such as thorax phantoms. Examples of commercially available phantoms are shown in Figure 1.2. 3D printing allows the production of geometries which are not available commercially.

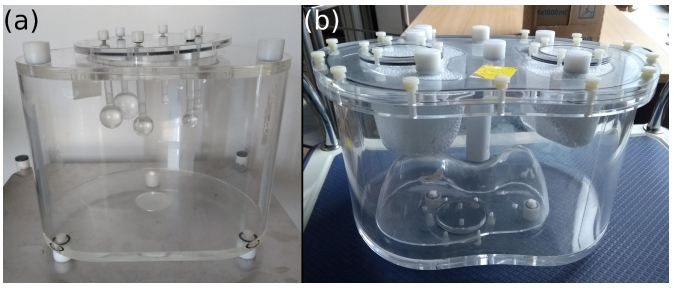

FIGURE 1.2: Two commercially available phantoms. (a) NEMA image quality phantom, (b) anthropomorphic phantom. The images in this figure are taken from [14].

1.4 3D printing

3D printing is a technique for manufacturing complex objects from 3D models. A photograph of a Prusa i3 3D printer (`www.prusa3d.com`) at The University of Manchester is shown in Figure 1.3. It allows the rapid production of geometries which would be prohibitively expensive to produce using other methods [15]. In the last 15 years 3D printing has become of increased interest in nuclear medicine for producing test phantoms [16–23]. In particular, anatomically accurate phantoms can be produced at a much lower cost than those available commercially [20]. These phantoms can then be used to perform scans of known anatomically representative activity distributions. Recent publications have demonstrated the usefulness of 3D printed phantoms in nuclear medicine [18–23]. A selection of 3D printed phantoms is shown in Figure 1.4. It has been demonstrated in the literature that 3D printed models made of plastics such as Acrylonitrile Butadiene Styrene (ABS) or Polylactic Acid (PLA) have similar attenuation properties as water and human tissues in the range of energies relevant for SPECT imaging [24].

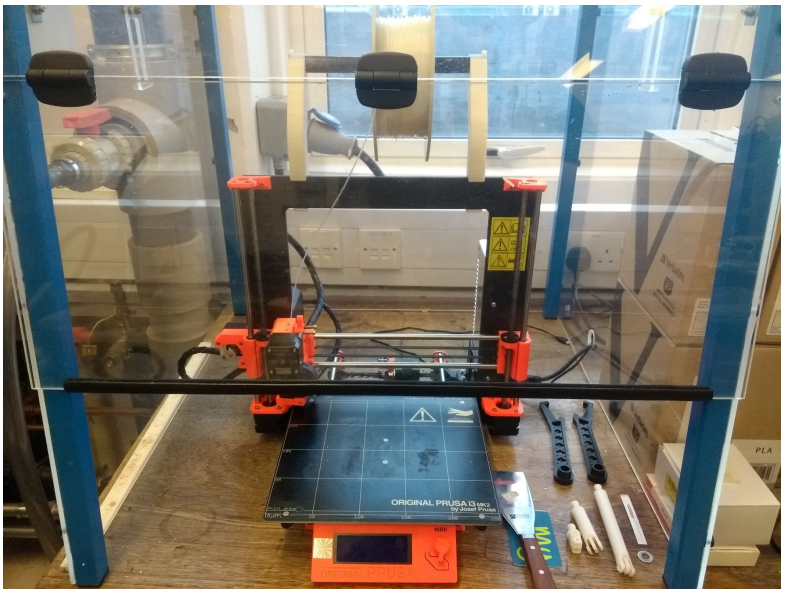

FIGURE 1.3: A photograph of a commercially available Prusa i3 3D printer.

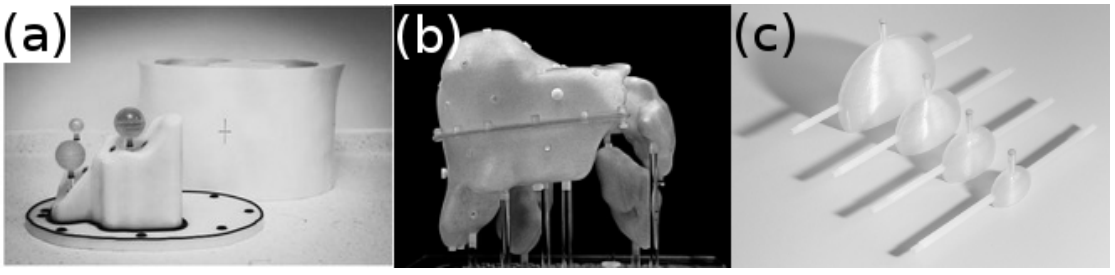

FIGURE 1.4: A selection of 3D printed phantoms for molecular radiotherapy. (a) The abdo-man phantom from reference [20]; (b) a patient specific phantom from reference [18]; (c) kidney phantoms from reference [21].

Chapter 2

Theory

2.1 Decay of relevant isotopes

This section provides a brief overview of radioactive decay and describes the decay of isotopes relevant to this thesis. The isotopes considered are ^{99m}Tc, ^{177}Lu and ^{131}I, which are commonly used in nuclear medicine.

2.1.1 Overview of radioactive decay

There are multiple methods by which unstable nuclei may decay. These include beta decay, electron capture, neutron emission, proton emission, alpha decay or fission. The daughter nucleus will often be produced in an excited state and will internally decay to its ground state by emitting a prompt gamma ray or an internal conversion electron. The isotopes considered in this thesis all beta decay, so only this decay process is discussed along with the relaxation of the daughter nuclei [3].

There are three possible types of beta decay: β^-; β^+ and electron capture. The processes for these are:

$$\mathrm{n} \rightarrow \mathrm{p} + \mathrm{e}^- + \bar{\nu}_\mathrm{e}$$
$$\mathrm{p} \rightarrow \mathrm{n} + \mathrm{e}^+ + \nu_\mathrm{e}$$
$$\mathrm{p} + \mathrm{e}^- \rightarrow \mathrm{n} + \nu_\mathrm{e}$$

In negative beta decay a neutron decays to a proton, an electron and an electron antineutrino. In positive beta decay a proton decays to a neutron, a positron and an

electron neutrino. Due to the three bodies in the final state, the emitted electron or positron has a continuous spectrum of possible energies up to a maximum given by the Q-value for the decay. In electron capture a proton absorbs an atomic electron, transforms into a neutron and emits an electron neutrino. Positive beta decay and electron capture are not possible for free protons [3, 25].

The daughter nucleus from beta decay will often be created in an excited state. The excited nucleus can decay to its ground state by emitting gamma ray(s) or atomic electrons. These processes are referred to as gamma decay and internal conversion respectively. When a nucleus gamma decays it transitions from a state with energy E_i to a state with energy E_f. A gamma ray will be emitted with energy equal to the difference between the states in the rest frame of the nucleus. In a different reference frame to the rest frame of the nucleus the energy of the gamma ray will be less than this due to the nucleus recoiling in order to conserve momentum. In internal conversion the excess nuclear energy is given to an atomic electron. If the energy given to the electron is greater than the atomic binding energy the electron will be ejected from the atom with any excess energy as kinetic energy. The resulting electron vacancy may result in the emission of X-rays as the atom de-excites [3, 25].

2.1.2 ^{99m}Tc

^{99m}Tc is an isotope commonly used in nuclear medicine for diagnostic imaging. ^{99m}Tc is a metastable state of ^{99}Tc with a half-life of 6.0072 h. It decays via gamma emission 99.9963 % of the time. The remaining possibility is negative beta decay to ^{99}Ru. The decay schemes are shown in Figures 2.1 and 2.2. The primary gamma emission is 140 keV. For the dominant beta decay the mean beta energy is 101.9 keV and the maximum beta energy is 350.6 keV [26]. While only a small percentage of decays result in the emission of beta particles, they are a significant source of radiation dose from ^{99m}Tc.

2.1.3 ^{177}Lu

^{177}Lu is used for both therapy (beta) and post-therapy imaging (gamma). ^{177}Lu decays by negative beta decay to ^{177}Hf, with 79.4 % of the decays to the ground state of ^{177}Hf. The half-life of ^{177}Lu is 6.647 d. The highest intensity gamma rays emitted from the decay of excited states of ^{177}Hf are 208 keV and 113 keV. For the dominant beta decay the mean beta energy is 149.35 keV and the maximum beta energy is 498.3 keV [27]. The decay scheme of ^{177}Lu is shown in Figure 2.3.

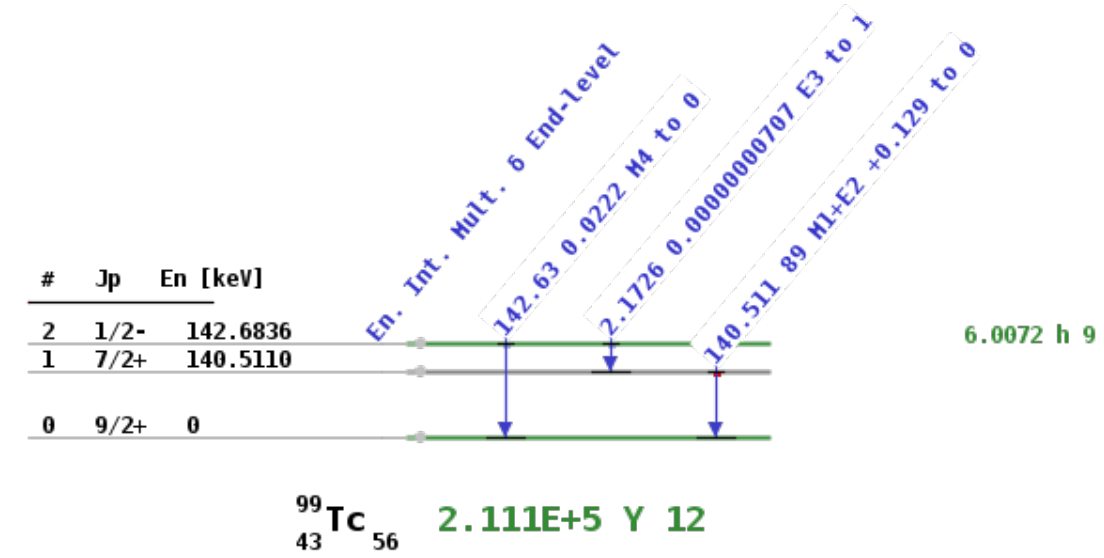

FIGURE 2.1: ^{99m}Tc gamma decay scheme. This is an internal decay to the ground state from the metastable state. This figure was generated using `https://www-nds.iaea.org/relnsd/vcharthtml/VChartHTML.html`.

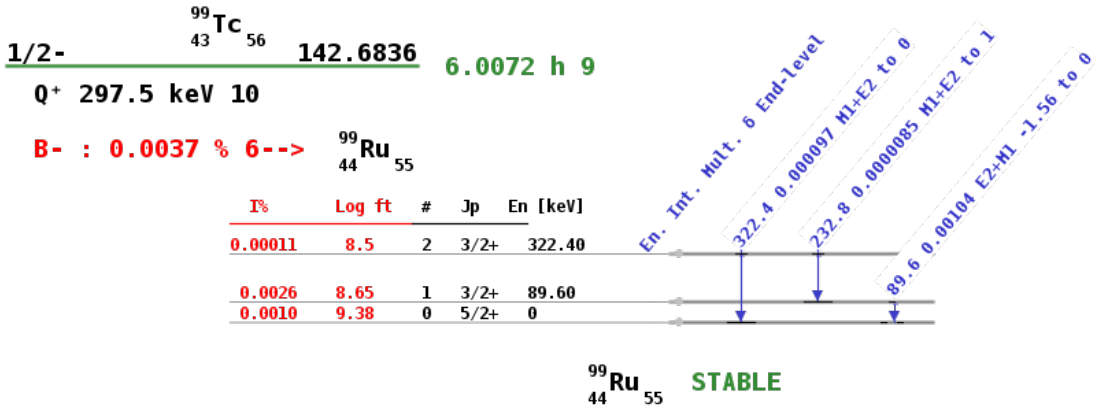

FIGURE 2.2: ^{99m}Tc beta decay scheme. This figure was generated using `https://www-nds.iaea.org/relnsd/vcharthtml/VChartHTML.html`.

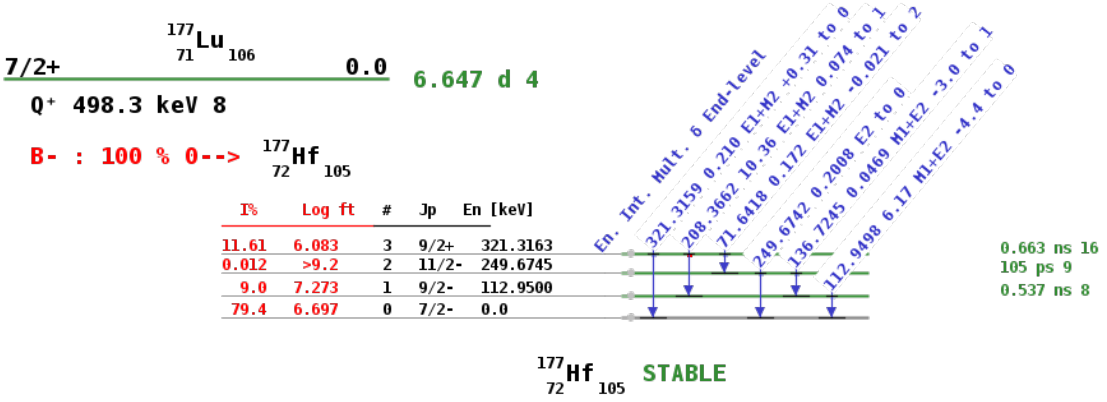

FIGURE 2.3: The decay scheme of ^{177}Lu. This is a β^- decay to ^{177}Hf followed by gamma emission. This figure was generated using `https://www-nds.iaea.org/relnsd/vcharthtml/VChartHTML.html`.

2.1.4 ^{131}I

^{131}I decays by negative beta decay to ^{131}Xe. The primary gamma emission from this decay is 364 keV. The decay scheme is shown in Figure 2.4. The mean energy of the dominant beta decay is 191.58 keV and the maximum beta energy is 606.3 keV [28]. ^{131}I is used for therapy, for instance thyroid therapies, and imaging [6].

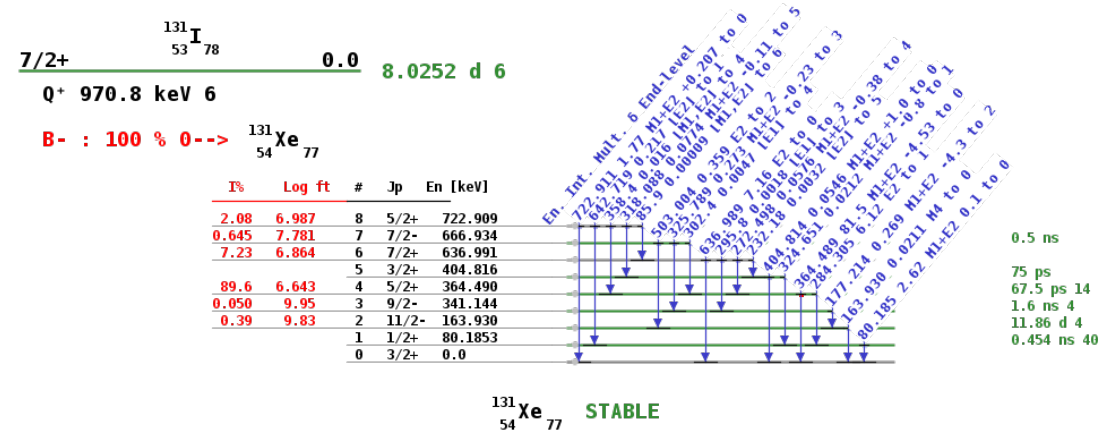

FIGURE 2.4: The decay scheme of ^{131}I. This is a β^- decay to ^{131}Xe followed by gamma emission. This figure was generated using `https://www-nds.iaea.org/relnsd/vcharthtml/VChartHTML.html`.

2.2 Radiation interactions

This section provides an overview of how the decay radiation emitted by the considered isotopes interacts as it travels through matter. The isotopes mentioned in this thesis emit

only beta and gamma rays so only the interactions of these particles are discussed.

2.2.1 Photon interactions

Cross-sections showing the likelihood of different interactions of photons are shown in Figure 2.5. None of the isotopes considered in this thesis emit gamma rays with an energy greater than 1022 keV and therefore electron pair production will not occur. There are three types of interaction photons can undergo in the energy range relevant to this thesis: Compton scatter; Rayleigh scatter and Photoelectric absorption.

Of these, photoelectric absorption is dominant below approximately 20 keV and Compton scattering is dominant above about 100 keV. Photoelectric absorption is a process in

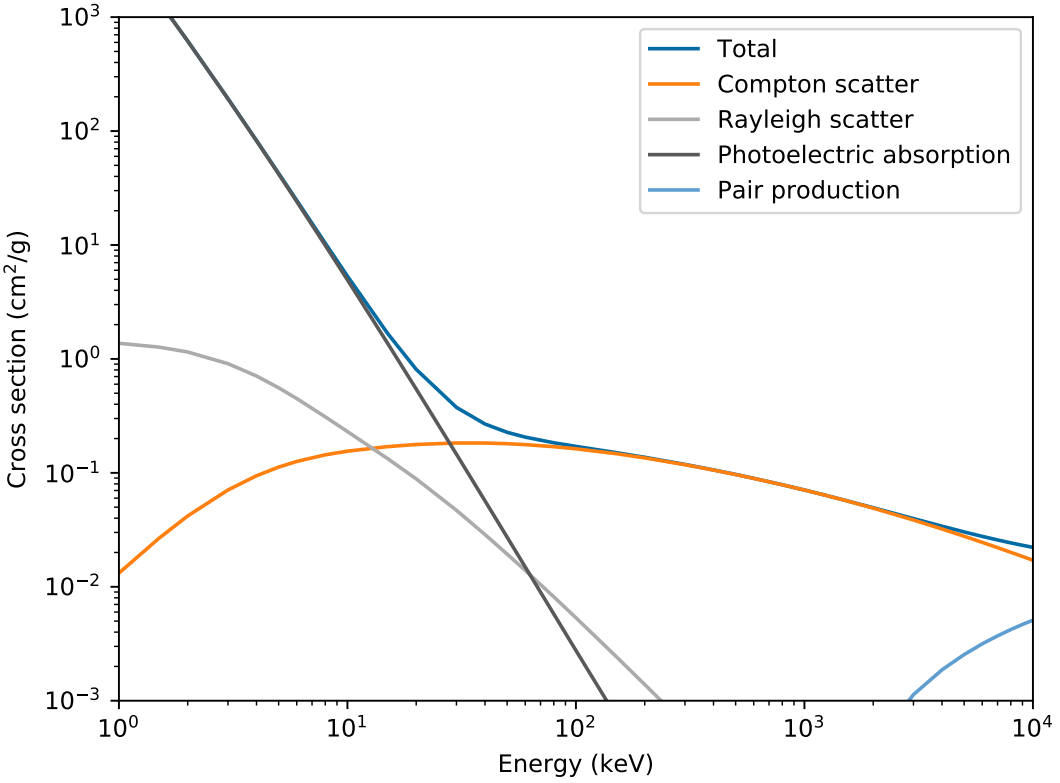

FIGURE 2.5: Photon interaction cross sections in water. The data in this figure are taken from [29].

which a photon is absorbed by an atomic electron. The electron is then ejected from the atom with kinetic energy

$$E'_e = E_\gamma - E_B - T'_{\text{rec}}, \tag{2.1}$$

where E_γ is the energy of the incident photon, E_B is the binding energy of the ejected electron and T'_{rec} is the recoil kinetic energy of the nucleus. The atom will then have an electron vacancy and therefore be in an excited state. It can de-excite by an electron

from a higher energy level filling the vacancy. In the process the atom will emit an X-ray, or eject another atomic electron in a process termed internal conversion [3, 30].

In Rayleigh scattering an incident photon is elastically scattered from an ensemble of atomic electrons. Rayleigh scattering is a classical process in which the photon can be treated as an electromagnetic wave. The incoming and scattered waves are in phase so Rayleigh scattering is also known as coherent scatter. The photon deposits no energy in the medium, so does not contribute any dose. The photon is attenuated and Rayleigh scattering is therefore relevant to modelling radiation transport [3, 30].

In contrast, Compton scattering is a quantum mechanical process of incoherent, inelastic scattering from an electron. Energy is deposited by the photon, so Compton scatter contributes to radiation dose. The energy deposited by the photon is transferred to the electron. The electron will then deposit energy as it slows. The energy of the scattered photon is given by

$$E' = \frac{E}{1 + \frac{E}{m_e c^2}(1 - \cos(\theta))}, \tag{2.2}$$

where E is the energy of the incident photon, E' is the energy of the scattered photon, m_e is the mass of the electron and θ is the angle the photon is scattered by [3, 30].

The intensity of a beam of photons travelling through a medium is given by Lambert-Beer's Law,

$$I = I_o \exp\left(-\mu \Delta x\right), \tag{2.3}$$

where I_0 is the emitted beam intensity, μ is the linear attenuation coefficient and Δx is the distance through the medium. If the beam passes through multiple materials with different attenuation coefficients Equation (2.3) is modified and I is given by

$$I = I_0 \exp\left(-\sum_{i=1}^{n} \mu_i \Delta x\right) \tag{2.4}$$

where n is the number of materials and μ_i is the attenuation coefficient of the i^{th} material [31]. It can be seen from this equation that the intensity of the photon beam will approach but never reach zero.

2.2.2 Electron interactions

Electrons are charged and deposit their energy more rapidly than photons. Being massive, electrons also slow down as their energy is deposited. The rate of energy loss of charged particles such as electrons is also known as the stopping power of a material, S. The

stopping power is given by

$$S = -\frac{dE}{dx} = \frac{4\pi e^4 z^2}{m_0 v^2} NB \tag{2.5}$$

where

$$B = Z\left[\ln\left(\frac{2m_0v^2}{I}\right) - \ln\left(1 - \frac{v^2}{c^2}\right) - \frac{v^2}{c^2}\right], \tag{2.6}$$

v is the velocity of the particle, ze is the charge of the particle, N is the number density of the material the particle is travelling through, Z is atomic number of the material, m_0 is the electron rest mass, e is the electronic charge and I is the average excitation and ionisation potential of the material. This slowing results in charged particles having a finite range in a medium. In tissue the range of electrons emitted from the isotopes discussed in this thesis is approximately 2 mm. The electron energy is lost through iterations with atomic nuclei and atomic electrons. The primary interactions are Coulomb scattering and bremsstrahlung. Coulomb scattering from atomic electrons is the dominant process of energy loss.

In collisions with orbital electrons the incident electron can lose any amount of its energy, due to both particles having the same mass. These collisions may be elastic or inelastic. All inelastic scatter results in energy being transferred to the medium. Only some elastic scatter results in energy being transferred to the medium.

When an electron interacts with a much more massive atomic nucleus it may be subject to a large change in direction. This is a large acceleration of a charged particle and such the electron emits radiation. The radiation emitted by such electrons is bremsstrahlung. The bremsstrahlung photon may be emitted with any energy up to that of the incident electron. Radiative losses are only a small fraction of the losses due to scattering [3, 25, 30].

2.3 Imaging

SPECT uses one or more gamma cameras to acquire planar images of the detected photons from a patient or test object at angular intervals around the patient or test object. The angular steps are typically between 3 and 6 degrees. These images, referred to as projections, are then reconstructed to provide a 3D image of the distribution of the radionuclide. CT uses X-rays to measure the distribution of attenuating material in a patient. The CT image is used to provide anatomical information to complement the SPECT data and in the SPECT image reconstruction process. The camera used in this project, a GE Infinia Hawkeye 4, is a hybrid SPECT/CT scanner. Hybrid scanners sequentially perform SPECT and CT imaging. The advantage of performing scans in this way is that the images are aligned, removing the need for registration of the images. In

practice patients may move between the two scans, introducing problems with registering the CT and SPECT images. For phantom scans this does not occur [31].

2.3.1 CT

CT scans pass a beam of X-rays through an object and measure the intensity of photons which have passed through. If such a beam is moved linearly across a patient and measuring the transmitted intensity a one-dimensional projection of the patient is acquired. By measuring the transmitted intensity from many different angles a set of projections is acquired. This procedure was used in the first generation of CT scanners. The most modern CT scanners use a fan-shaped beam of X-rays, but the imaging principles are the same. Reconstructing the set of projections will provide the distribution of attenuation material in a slice of the patient. Back-projection is the basis of modern CT reconstruction. Back-projection 'smears' the measured projections back in the direction of the detected radiation, as the inverse of the projection. However this leads to artefacts as shown on the left hand side of Figure 2.6. The artefacts arise because the projections are non-negative and hence non-negative values are smeared over the entire image and positive values are assigned to pixels outside the patient. This is not compensated for by the other projections, as all the projections are non-negative. Applying a filtering function to the acquired projections before back-projecting can address this problem. The filtering function is a high-pass filter, applied by convolution with each projection. The filtering introduces negative values into the projections which compensate for the positive values introduced outside the object being imaged. The result is illustrated on the right hand side of Figure 2.6. It can be seen that the artefacts are no longer present. In practice there are multiple possible filter functions which may be applied. The functional form of one such filter, the Ramachandran-Lakshminarayanan filter is shown in Figure 2.7 as an example [31–33].

In nuclear medicine it is conventional to scale the measured attenuation coefficients of the patient to that of water. This gives the attenuation in Hounsfield units or CT number [32]. The scaling is defined as

$$\text{CT number} = \frac{\mu_{\text{tissue}} - \mu_{\text{water}}}{\mu_{\text{water}}} \times 1000. \tag{2.7}$$

Air has a CT number of -1000 and water a CT number of 0. Modern CT scanners typically acquire data by continuously rotating an X-ray tube around the patient as the patient is moved past. In hybrid SPECT/CT imaging low dose CT images are acquired to minimise the radiation dose the patient receives. These images are of lower quality than a diagnostic CT but are adequate for attenuation correction and organ localisation [31, 32].

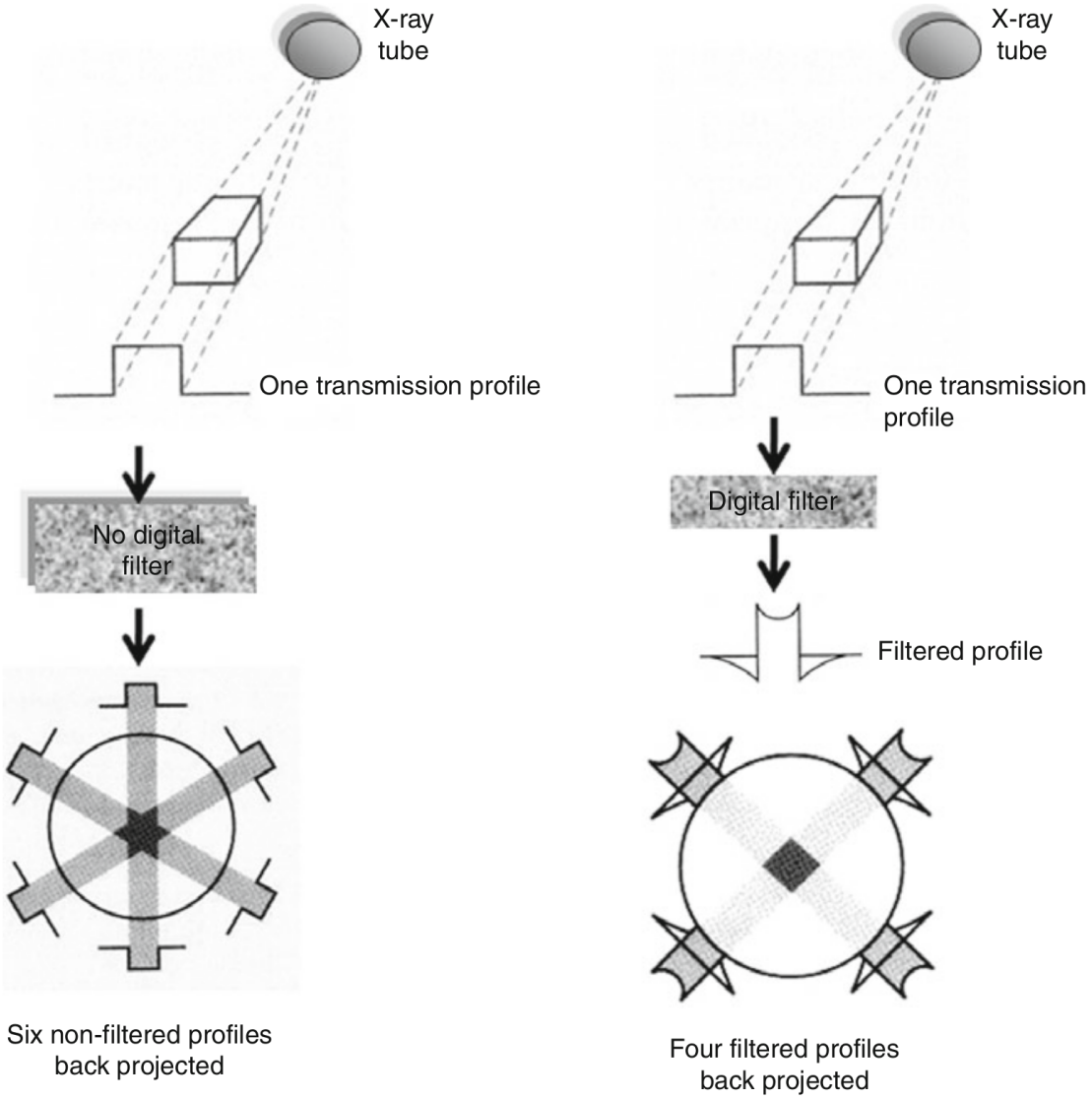

FIGURE 2.6: A comparison of simple back projection (left) and filtered back projection (right). In the simple case, a star-shaped image artefact is visible after the projections of the object are back-projected. When filtered back projection is used the artefact is removed. This figure is taken from [31].

The GE Infinia Hawkeye 4 scanner uses an X-ray tube voltage of 140 kV and a current of 2.5 mA [34].

2.3.2 SPECT

Gamma cameras are used to detect the position and energy of gamma rays. A SPECT scanner consists of one or more detectors rotated around a patient to obtain a series of planar images from different angles. Gamma cameras typically consist of a lead collimator, a sodium iodide scintillator crystal and an array of PMTs. The rear of the camera is surrounded by lead shielding to prevent photons which do not originate from the patient

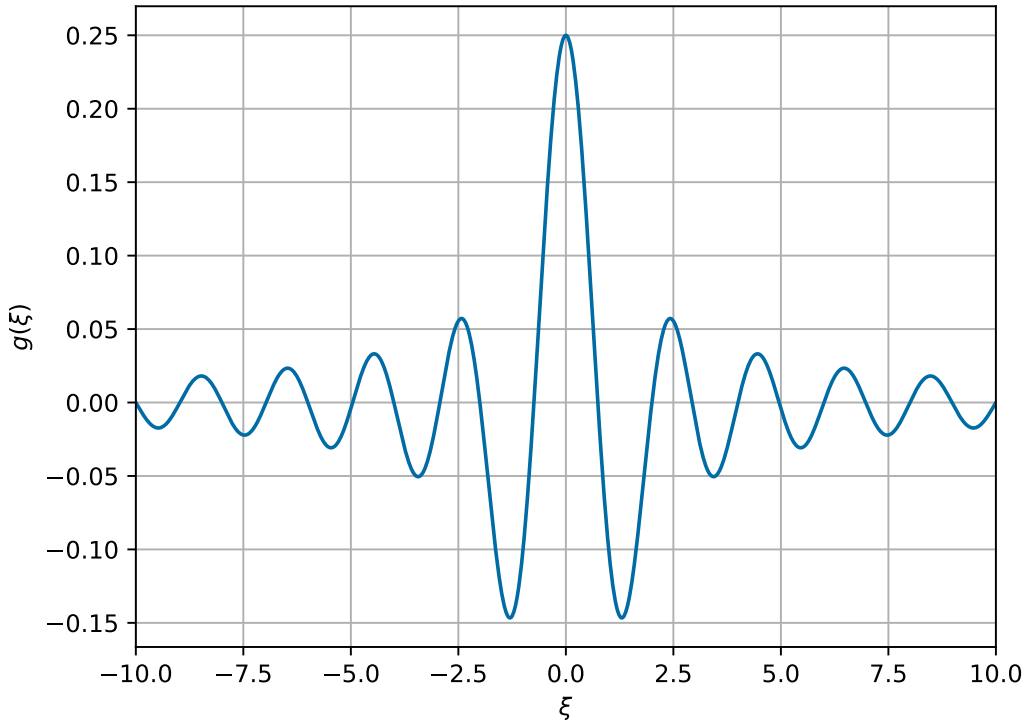

FIGURE 2.7: The continuous form of the Ramachandran-Lakshminarayanan filter function in the spatial domain. This is shown as an example of a convolution kernel which may be used as a filter in filtered back projection.

being detected. A schematic diagram of a gamma camera is shown in Figure 2.8. A parallel hole collimator consists of a lead sheet containing an array of hexagonal holes. The collimator is required to restrict the detection of gamma rays to those which are travelling perpendicularly to the holes of the collimator. Different thicknesses of collimator are used depending on the energy of the photopeak(s) being imaged. Low Energy High Resolution (LEHR) collimators are used in this work for imaging ^{99m}Tc and Medium Energy General Purpose (MEGP) collimators are used for imaging ^{177}Lu. The mechanical properties of the collimators are described in Table 2.1. For higher energy photons thicker collimators with thicker walls between the holes (septa) are used to reduce septal penetration. Septal penetration reduces the image quality as there is no way to distinguish photons which pass straight through a hole and those which pass through a septa. The collimator gives the detector a poor efficiency but is required to form a usable image. The resolution of the system (Full Width at Half Maximum (FWHM) at 100 mm) is 7.4 mm with the LEHR collimator and 9.4 mm with the MEGP collimator. The sensitivity is 72 cps MBq^{-1} with the LEHR collimator and 65 cps MBq^{-1} with the MEGP collimator [34]. When a gamma ray interacts in the scintillator crystal typically several thousand optical photons are emitted. A light guide is used to hermetically seal the crystal while allowing light to

reach the PMTs. The scintillation photons are detected by the array of PMTs. From the detected signal the energy and position of the gamma ray is calculated [4, 35].

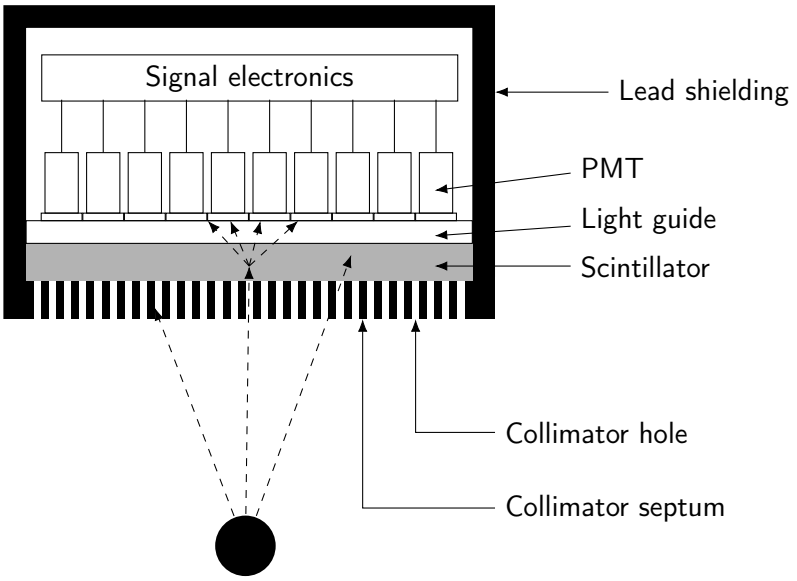

FIGURE 2.8: A schematic diagram of a gamma camera detector. The circle represents a radioactive source. The dotted lines to the scintillator crystal represent gamma rays emitted by the source. The left-hand gamma ray is stopped in the collimator septum. The central gamma ray passes through a collimator hole and causes the emission of optical photons in the scintillator. The right-hand gamma ray penetrates a collimator septum before interacting in the scintillator and will degrade the image quality.

TABLE 2.1: Description of the LEHR and MEGP collimators for a GE Infinia Hawkeye 4 SPECT/CT scanner with a 3/8" crystal. The information in this table is taken from reference [34].

Collimator	Septal penetration at 140 keV (%)	Hole diameter (mm)	Septal thickness (mm)	Hole length (mm)
LEHR	0.3	1.5	0.2	35
MEGP	2.0	3.0	1.05	58

In SPECT, one or more gamma cameras are rotated around a patient. Two cameras mounted 180° apart are used in the GE Infinia Hawkeye 4. The 2D projections acquired by the gamma camera are reconstructed to give a 3D image of the distribution of activity. This distribution is a grid of 3D pixels, or voxels, with the value being the number of counts detected from the voxel. In this thesis the Ordered Subset Expectation Maximisation (OSEM) algorithm, with 4 iterations and 10 subsets, is used unless otherwise stated. This is the number of iterations and subsets used clinically at the Christie Hospital. OSEM is an iterative algorithm which extends the method of Expectation Maximisation to process subsets of the data separately in order to speed up the computation time needed for reconstruction [36]. Expectation Maximisation is a two step iterative process. First the current estimate of the activity distribution is forward projected to calculate the expected

projections based on that distribution. The difference between the expected and measured projections is then used to adjust the estimated activity distribution. Figure 2.9 illustrates the process. Iterative reconstruction allows the physical processes in the emission and detection of radiation to be modelled [37].

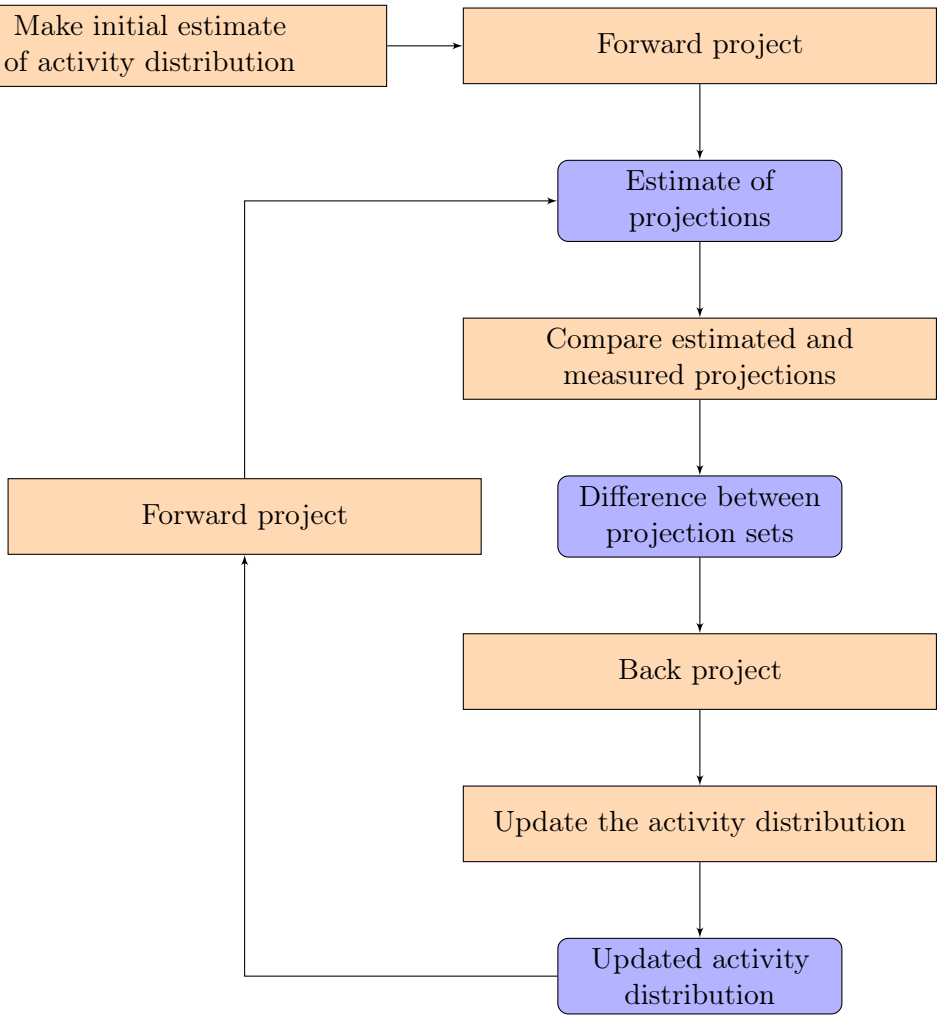

FIGURE 2.9: A flow chart showing the process of Expectation Maximisation iterative reconstruction. The process is repeated until the specified number of iterations have been carried out.

There are multiple effects which degrade quality of any reconstructed image. Photons emitted from the centre of the patient are more likely to be attenuated than photons emitted from the edge. If not corrected for this will result in an underestimation of the counts in the centre of the patient. Attenuation information from the CT data is used to correct for this during the image reconstruction. Attenuation coefficients are energy dependent so the measured values must be converted to those for photons of the emitted energy before use for attenuation correction.

Scattered photons may pass through a collimator hole and be detected. This results in a photon being detected from a position it did not originate at. Examples of some possible paths a photon may take are shown in Figure 2.10. Path (c) in Figure 2.10 will result in the detected photon appearing to come from the wrong position. To reduce the impact of scattered photons, only photons with energies in a window around the emission photopeak energy are used in the reconstruction. Due to the poor energy resolution of the detector, about 9 % for the 140 keV emission from ^{99m}Tc, this window is often around 10 % above and below the photopeak energy. However photons can Compton scatter by large angles and still be within the window set around the photopeak. Scatter correction is used to correct for this. There are multiple methods of scatter correction. In dual-energy window scatter correction a second energy window is used below the photopeak of interest. All the events in this window are assumed to have scattered. A simulated ^{99m}Tc energy spectrum is shown in Figure 2.11 with the energy windows indicated. A fraction of the scattered image is subtracted from the photopeak image in the reconstruction process. The fraction required to be subtracted is determined either by Monte Carlo simulations or analysis of phantom data. In triple-energy window (TEW) scatter correction a window is also defined above the photopeak. The two scatter images are used to inform the subtraction from the photopeak image. The number of scattered photons in the photopeak window, C_{scat}, is estimated to be

$$C_{\text{scat}} \approxeq \left(\frac{C_l}{W_l} + \frac{C_u}{W_u}\right) \cdot \frac{W_p}{2}, \tag{2.8}$$

where W_u and W_l are the widths of the upper and lower scatter windows, C_u and C_l are the number of counts in the upper and lower scatter windows and W_p is the width of the photopeak window [35, 38–40]. TEW scatter correction is used when there scattered photons from higher energy emissions may be detected in the photopeaks of interest. A simulated energy spectrum of ^{177}Lu is shown in Figure 2.12, showing the scattered and unscattered components and the energy windows used. It can be seen that there is a greater scatter component in the EM1 window.

The finite spatial resolution of the scanner results in partial-volume effects in imaged objects. Partial volume effects occur when the edge of an object is not at the edge of a voxel, causing the counts inside and outside the object to be averaged. Figure 2.13 illustrates the effect. The effect is most significant in small structures, with dimensions less then three times the FWHM of the spatial resolution of the scanner. The FWHM may be measured using a line source phantom. Resolution recovery methods may be applied during the reconstruction process to correct for this [1, 11].

SPECT scanners can also be used in Pulse Height Analysis (PHA) mode. In this mode the scanner is used to measure an energy spectrum with the heads stationary. Data are collected until a set number of counts have been detected.

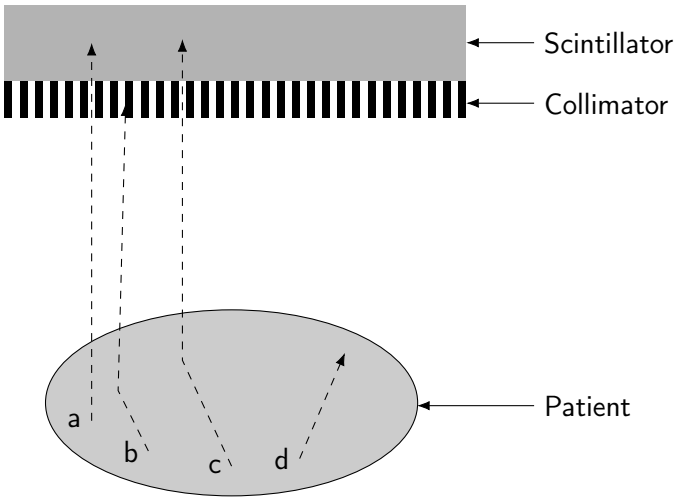

FIGURE 2.10: A schematic diagram of possible photon paths. Photon (a) is emitted and travels directly to the crystal without interacting in the patient. Photon (b) scatters in the patient and is absorbed in the collimator. Photon (c) scatters in the patient and then reaches the crystal. Photon (d) is absorbed in the patient.

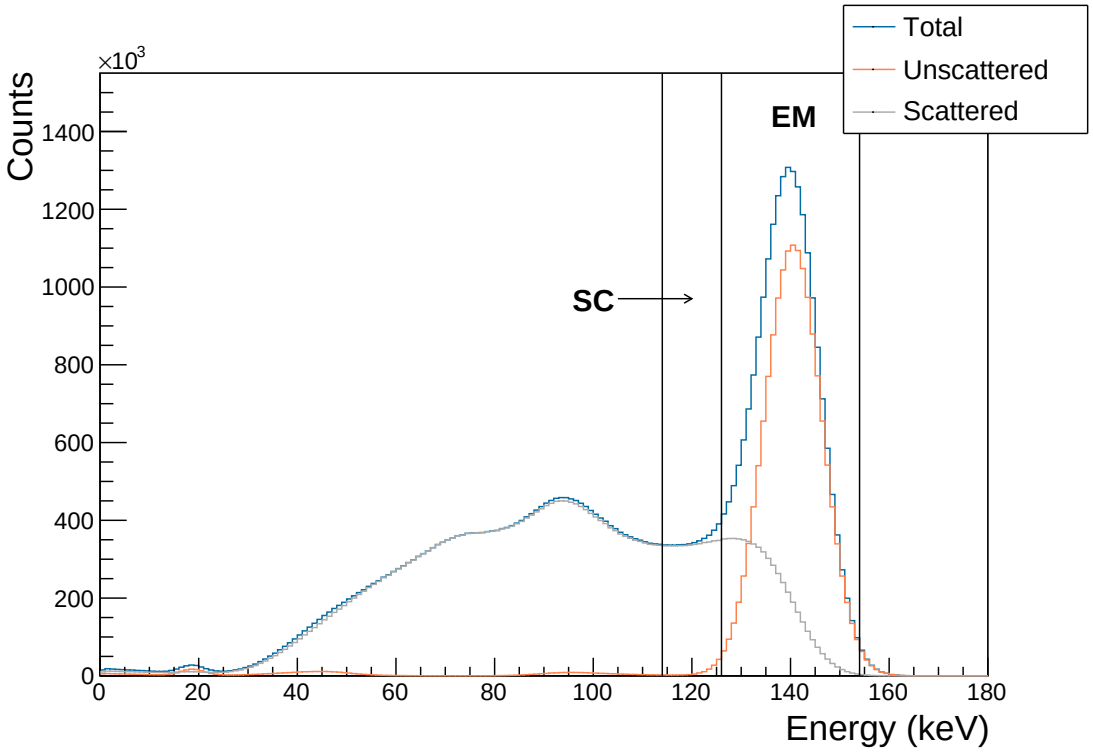

FIGURE 2.11: An example simulated energy spectrum for ^{99m}Tc, showing the energy windows used. The detected energy spectrum (total) and the unscattered and scattered components are shown. The 'EM' window is the energy window for the gamma emission peak. The 'SC' window is used to provide an estimate of the number scattered photons in the emission window in dual energy window scatter correction.

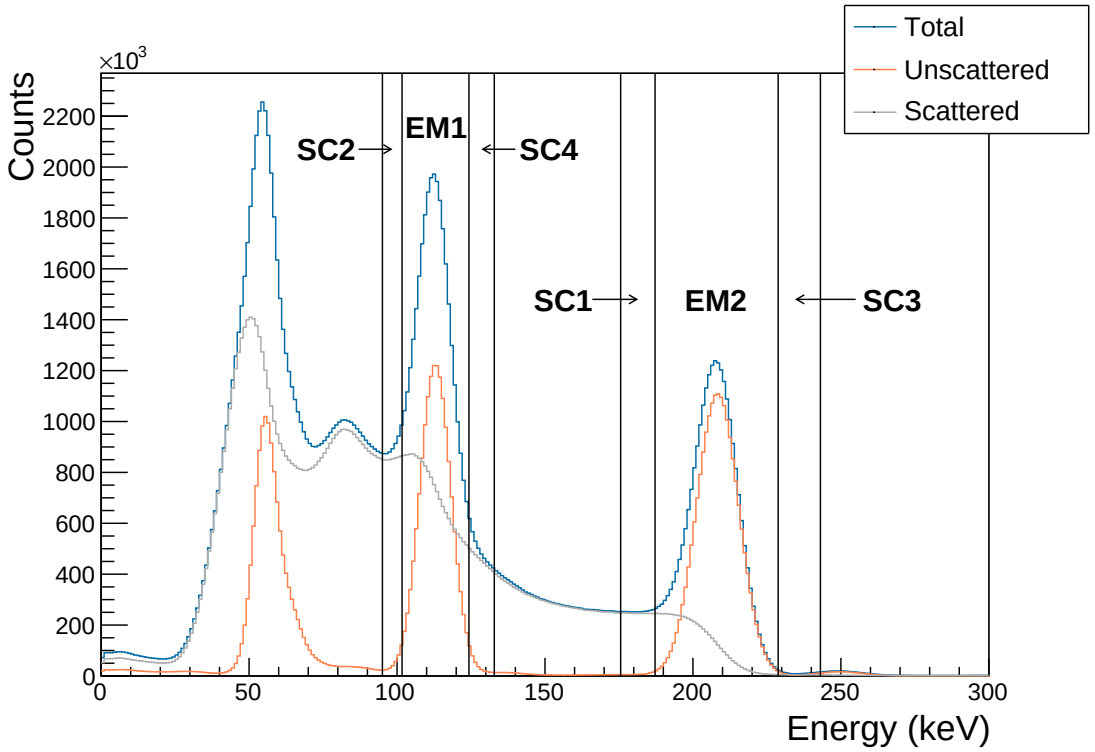

FIGURE 2.12: An example simulated energy spectrum for ^{177}Lu, showing the energy windows used. The detected energy spectrum (total) and the unscattered and scattered components are shown. The 'EM1' and 'EM2' windows are the emission windows for the primary decays of ^{177}Lu. The 'SC1', 'SC2', 'SC3' and 'SC4' windows are used to provide an estimate of the number of scattered photons detected in the emission windows in triple energy window scatter correction

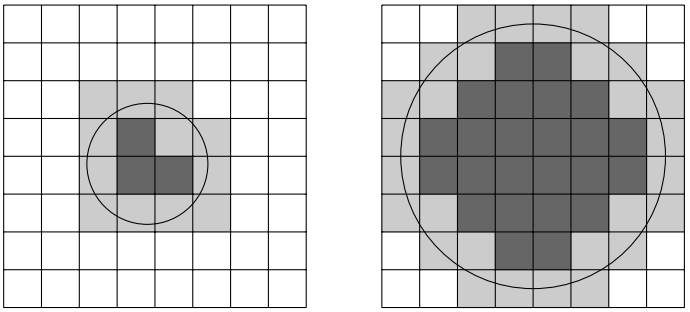

FIGURE 2.13: A diagram demonstrating partial volume effects. The grid represents the pixels in an image and the circles represent objects being imaged. Pixels completely inside the circles are shaded dark grey and pixels on the edge are shaded light grey. The ratio of interior pixels to edge pixels is larger for the larger circle.

2.4 Quantitative SPECT

For imaging being viewed for diagnostic purposes it may be sufficient for the image to be presented qualitatively in terms of counts. This will show areas of less activity and more activity. For dosimetry to be done, the counts must be converted to units of becquerels (Bq). This is done using a calibration factor, cf, defined as

$$\mathrm{cf} = \frac{\text{counts}}{\text{activity in insert} \cdot \text{scan duration}} \tag{2.9}$$

in units of counts per second per MBq. A calibration factor may be defined for any arbitrary volume. The calibration factor is specific to a camera and set of reconstruction parameters. The calibration factor will also depend on the size and shape of the volume it is defined for due to the limited spatial resolution of the SPECT detector and the partial volume effects inherent to the voxelisation of the activity distribution. The calibration factor can then be used to quantify the activity in a region. In phantom scans the activity in the inserts is known from measurements taken when the phantoms were filled. In such cases the quality of calibration factors may be assessed by comparing the quantified activity in a region with the known activity. This can be done numerically using the recovery factor, rf, defined as

$$\mathrm{rf} = \frac{A_{\text{quantified}}}{A_{\text{administered}}}. \tag{2.10}$$

A recovery factor greater than one indicates an overestimation of the activity in the region and a recovery factor less than one indicates an underestimation.

As described in reference [22] theoretical values of the ratio of the calibration factor for a volume to the true camera sensitivity, $\mathrm{cf}_{\mathrm{true}}$, can be calculated. $\mathrm{cf}_{\mathrm{true}}$ can be measured by calculating the calibration factor for an object large enough that any partial volume effects are minimised. The ratio for a particular volume of interest (VOI) is given by

$$\frac{\mathrm{cf}_{\mathrm{voi}}}{\mathrm{cf}_{\mathrm{true}}} = 1 - \frac{\sum_{i=i}^{\mathrm{nVoxels}} \alpha_i}{\mathrm{nVoxels}}, \tag{2.11}$$

where nVoxels is the total number of voxels in the VOI and for an individual voxel centred at x_i, y_i, z_i with x_a, x_b, y_a, y_b, z_a, z_b being the perpendicular distances to the closest VOI boundary,

$$\alpha_i = 1 - \int_{z_a - z_i}^{z_b - z_i} \int_{y_a - y_i}^{y_b - y_i} \int_{x_a - x_i}^{x_b - x_i} g(x_i, y_i, z_i, \sigma) dx\ dy\ dz. \tag{2.12}$$

$g(x, y, z, \sigma)$ is defined as

$$g(x, y, z, \sigma) = \frac{1}{\sigma^3 (2\pi)^{\frac{2}{3}}} \exp\left(-\left(\frac{x^2 + y^2 + z^2}{2\sigma^2}\right)\right) \tag{2.13}$$

and

$$\sigma(\text{FWHM}) = \frac{\text{FWHM}}{2\sqrt{2\ln 2}}, \tag{2.14}$$

where FWHM is the full width at half maximum of the spatial resolution of the SPECT camera.

2.5 Dosimetry

Many of the interactions of radiation in tissue result in the deposition of energy in a tissue. This deposition of energy results in a radiation dose. The absorbed dose is measured in joules of energy deposited per kilogram of target material. The SI unit of dose is the gray. If a radiation weighting factor is applied the dose is referred to as the equivalent dose in units of sieverts [41].

2.5.1 Biological effects of dose

The biological effects of radiation are primarily due to damage done to DNA in cell nuclei. This damage may be direct or indirect. Direct damage is caused by the radiation interacting with the DNA molecule itself. Indirect damage is caused by the radiation ionising some other molecule in the cell. This interaction results in the creation of free radicals. Free radicals contain an unpaired electron and are therefore very reactive. The free radicals may then interact with DNA molecules, resulting in damage. The majority of radiation damage is due to the indirect effect [3, 41].

DNA molecules are made of two strands, connected by base pairs. Damage is done by one of the bases being changed, or by one or both of the strands being broken. If one of the bases is changed a mutation may result or there may be no effect. If one of the strands is broken, known as a single strand break, it is possible for the cell to repair itself given sufficient time. However the repair may be incorrect or incomplete in which case a mutation may still occur. If both strands are broken in close proximity, known as a double strand break, then the cell is less likely to survive [3, 41].

2.5.2 Dose calculation

The absorbed dose in gray, D, to a region of mass m is defined as

$$D = \frac{\epsilon}{m}, \tag{2.15}$$

where ϵ is the energy deposited in the region. The MIRD schema is a general method for calculating the dose from a source region to a target region [42]. The general MIRD equation for the mean absorbed dose $D(r_T, T_D)$ to a region r_T in time T_D is:

$$D(r_T, T_D) = \sum_{r_s} \int_0^{T_D} A(r_S, t) S(r_T \leftarrow r_S, t) dt, \tag{2.16}$$

where $A(r_S, t)$ is the time dependent activity in the source region r_S and $S(r_T \leftarrow r_S, t)$ represents the mean absorbed dose rate to target region r_T at time t per unit activity in source region r_S. S depends on both the radionuclide present and the spatial arrangement of the source and target regions. S is given by:

$$S(r_T \leftarrow r_S, t) = \frac{1}{m(r_T, t)} \sum_i E_i Y_i \phi(r_T \leftarrow r_S, E_i, t), \tag{2.17}$$

where $m(r_T, t)$ is the mass of the r_T at time t. The summation is over all decay channels for a particular radionuclide. E_i is the energy of the i^{th} nuclear transition, Y_i is the number of i^{th} nuclear transitions per nuclear transformation and $\phi(r_T \leftarrow r_S, E_i, t)$ is the fraction of energy E_i emitted from r_S at time t which is absorbed in r_T, called the absorbed fraction. ϕ may divided by the mass of the target m to calculate the specific absorbed fraction. In cases where ϕ and therefore S are constant with time Equation (2.16) can be written as:

$$D(r_T, T_D) = \sum_{r_S} \widetilde{A}(r_S, T_D) S(r_T \leftarrow r_S), \tag{2.18}$$

where $\widetilde{A}(r_S, T_D)$ is the total number of radioactive decays in region r_S during time T_D. In nuclear medicine T_D is set to infinity as the radionuclides used generally have short physical half-lives [42]. S values for different radionuclides and anatomical models are tabulated in the literature [43–45]. These are calculated by Monte Carlo simulation. It is also possible to use direct Monte Carlo simulation for an individual patient to perform patient-specific dosimetry. S-factors are approximately symmetric if they are calculated for a uniform source in a finite homogeneous medium [3].

Clinically there are multiple software packages available which can perform dosimetry in either of these ways [3]. Of these, OLINDA/EXM 1.0 and OLINDA/EXM 2.0 are used in this thesis [46, 47]. OLINDA/EXM 1.0 uses the Cristy and Eckerman phantom set to perform whole body dosimetry, along with models of some specific organs. The Cristy and Eckerman phantoms are mathematical models based on population averages of organ size. Figure 2.14 shows a diagram of the adult male phantom. These models may not be representative of any particular individual. S-factors for these were pre-calculated for more than 800 radionuclides and are stored in a database [46]. These S-factors are based on calculations of specific absorbed fractions performed in the 1980s [45]. OLINDA/EXM 2.0

uses newer models based on the ICRP 89 phantoms [47]. The open dose project aims to produce an open database of S-factors for a variety of patient models calculated using a range of Monte Carlo simulation packages [48]. The S-factors are then used to calculate the dose to every source – target pair. The masses of the phantom organs can be adjusted to that of the patient to account for differences in size. This does not increase the size of the organ but rather the density. The dose output gives the contributions to the dose from alpha particles, electrons and photons. Patient-specific S-factors may be calculated using direct Monte Carlo simulation of the patient geometry. This is currently prohibitively time consuming for clinical use but is possible for research. Whichever method is used the activity distribution in the patient over time must be quantified in order to calculate $\widetilde{A}(r_S, T_D)$ for each source organ. This is done by serial quantitative imaging to measure the activity in each organ over time. The total number of decays is then the area under the curve described by the measured points. This can be calculated by numeric integration or analytically integrating a function fitted to the data points [1].

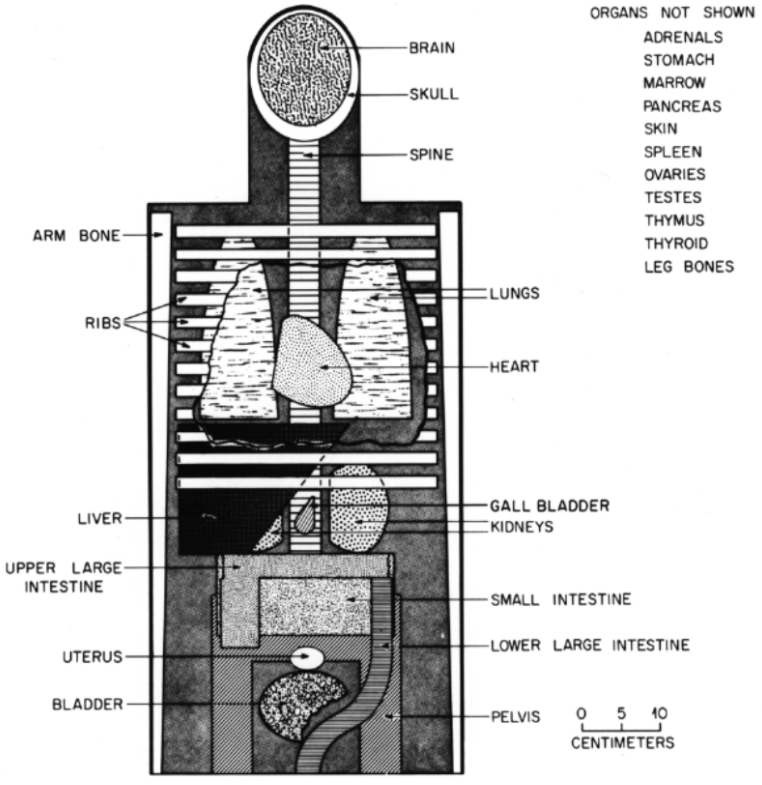

FIGURE 2.14: The geometry of the Cristy and Eckerman adult male phantom. The phantom is based on simple geometrical objects and is not representative of any particular individual. This figure is taken from reference [49].

2.6 Monte Carlo methods

The processes involved in radiation transport can be described using cross-sections, which give the probability of a process happening. These cross-sections may be used to define probability density functions (PDFs). Monte Carlo methods sample the PDFs to calculate a possible outcome of an interaction. By sampling the PDFs many times, an approximation to the true distribution of results can be obtained. Monte Carlo methods are not limited to radiation transport. A simple example of a Monte Carlo method is estimating the value of π. A circle of radius r is drawn inside a square of side length $2r$. The ratio of the area of the circle to the area of the square is $\pi/4$. If points within the square are randomly sampled, for instance by throwing a dart, the fraction of points within the circle approaches $\pi/4$. Figure 2.15 illustrates this process [3, 50]. There are many Monte Carlo codes available for the simulation of radiation transport [50]. These include MCNP, EGSnrc, Penelope and Geant4 [51–54]. In this work GATE (Geant4 Application for Tomographic Emission) is used [55]. GATE is based on Geant4 and provides extensions for tomographic imaging, such as the ability to read medical image formats and simplify time-dependent detector positions. The output of imaging simulations used in this thesis is in the ROOT file format [56]. A benefit of Monte Carlo simulation for nuclear medicine imaging is that the complete history of each particle is known. This provides information which is not available experimentally. Before a Monte Carlo simulation can be trusted it must be validated by comparison to experiment.

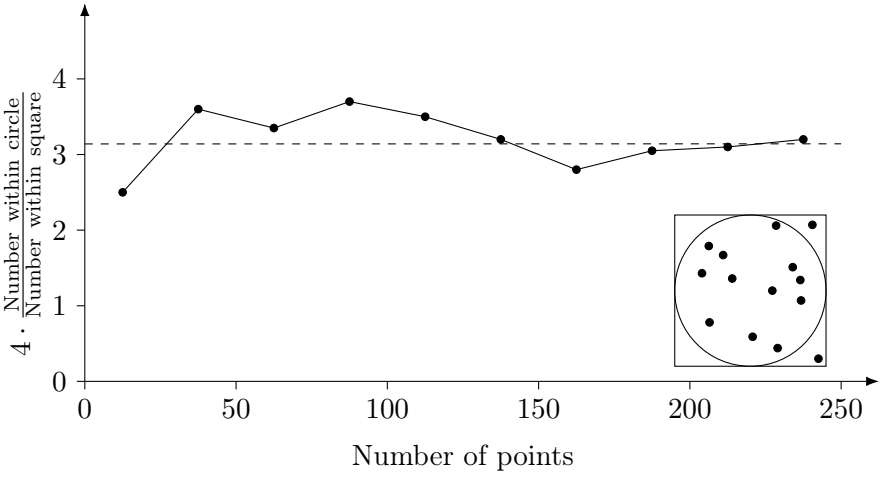

FIGURE 2.15: An example of a Monte Carlo method to calculate the value of π. As more points are sampled within the square, the fraction within the circle will approach $\pi/4$. This figure is adapted from [3].

2.7 Calculation of uncertainty in phantom imaging

When calculating calibration factors and recovery factors care must be taken to ensure that correlated components of uncertainty are considered. These correlations will often be due to the activities in inserts being measured using the same radionuclide calibrator. The radionuclide calibrator is a well-type ionisation chamber used to measure the amount of activity in a vial or syringe. The National Physical Laboratory (NPL) has published a Good Practice Guide describing the calibration and quality control for such calibrators [57]. A photograph of a radionuclide calibrator at the Christie Hospital is shown in Figure 2.16. The stability of the radionuclide calibrator response over time is monitored using a long-

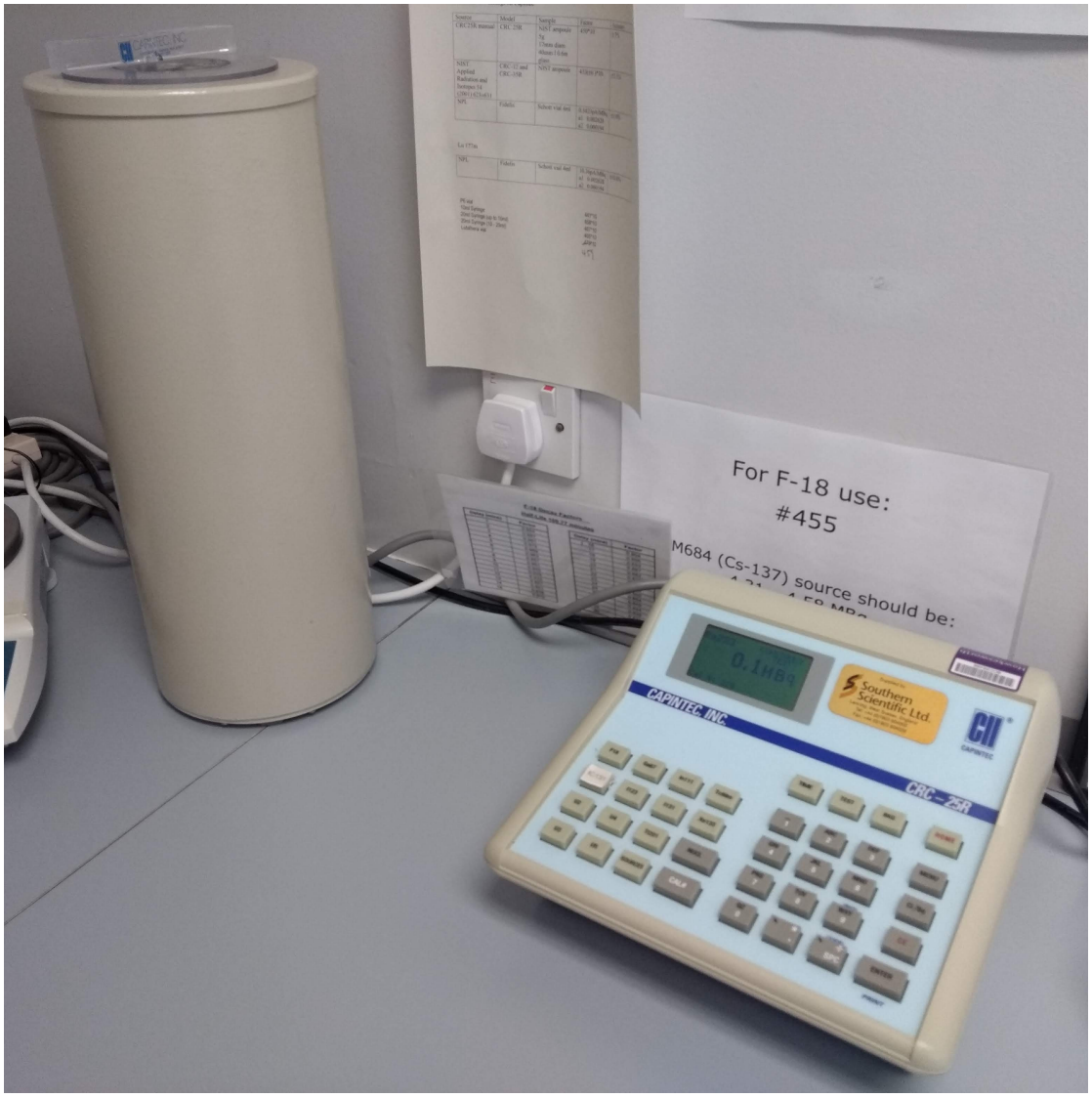

FIGURE 2.16: A photograph of a radionuclide calibrator at the Christie Hospital. On the left is the ionisation chamber detector into which samples are placed. On the right is the digital readout display. This figure is taken from reference [14].

lived check source such as ^{137}Cs. This ensures the reproducibility of the measurements

using the calibrator. The accuracy of the calibrator is maintained by calibration to reference sources traceably calibrated to national standards. Multiple measurements of a source are used to check the repeatability of measurements. To use the calibrator, calibration factors must be calculated to relate the measured current to the activity for a particular radionuclide and source geometry [57]. When filling inserts, multiple measurements will be performed. These may be measurements of the activity in a vial and syringe before and after filling an insert, or measurements of activity while making a stock solution and subsequent measurements of mass to determine the volume of solution in an insert. The Guide to the Expression of Uncertainty in Measurement (GUM) provides detailed guidance on how to calculate the uncertainty on measurements and derived quantities [58]. In this case the uncertainties are assumed to be distributed normally and are combined in quadrature.

The calibration to a primary standard is correlated for all measurements in a particular calibrator and should therefore be excluded from any comparisons between them. This includes the comparison of SPECT calibration factors and recovery factors as a change in the calibration of the ionisation chamber will result in a change in the absolute values of the calibration factors and recovery factors but not their relative values. The drift in the calibration of the ionisation chamber relative to a long-lived ^{137}Cs source is also correlated. The correlation will be stronger for measurements close together and weaker for measurements far apart. The effect of this correlation is neglected in this thesis as the contribution of the uncertainty due to the drift of the ionisation chamber is negligible in comparison to the other sources of uncertainty. Correlations will also arise when multiple measurements are done in the same filling session as the activity will be based on the same set of ionisation chamber measurements.

The uncertainty on the counts in a VOI is determined by the uncertainty on the definition of the VOI and the statistical uncertainty on the number of counts in each voxel in the VOI. The number of counts follows a Poisson distribution so the uncertainty on the number of counts is $\sigma = \sqrt{N}$, where N is the number of counts. The uncertainty on the number of counts in the VOI due to definition was calculated using the 'random' method described in [59]. The points defining the boundary of each VOI were shifted randomly and the variation in counts observed for 20 different perturbations.

The European Association of Nuclear Medicine (EANM) has recently published guidance on the propagation of uncertainty in MRT [9]. A paper by D'Arienzo and Cox presented analysis of the uncertainty in the calibration of imaging systems in MRT [60]. Phantom studies allow the assessment of systematic effects from using inappropriate calibration factors. Similarly Monte Carlo simulation of dosimetry allows the assessment of S-factors. These effects are not random but are a constant offset from the true value.

Chapter 3

Investigation of anthropomorphic calibration factors

This chapter describes the production and initial use of the Christie Anthropomorphic Tomographic Imaging Ellipse (CATIE) phantom. The majority of the work in this chapter has been published in reference [23]. CATIE is a large elliptical cylinder to represent the patient body. The phantom is used with 3D printed inserts based on a patient CT. The phantom was used to investigate the impact of calibration factor on activity quantification in a patient-specific geometry. Doses to the modelled organs were calculated using clinical dosimetry software and compared to patient-specific Monte Carlo simulations.

3.1 Production

CATIE is a large perspex elliptical cylinder designed to represent the human abdomen [23]. It is designed to allow 3D printed inserts representing patient organs to be placed in anatomically representative positions. The dimensions of the ellipse were chosen such that a range of patient organ sizes would fit inside it. Inserts were produced for the liver, spleen and both kidneys. These were chosen as they are the organs most at risk in the MRT therapies considered. The organs were outlined on a diagnostic CT scan of the patient by a clinician to produce binary VOIs. These VOIs were then smoothed and converted into STL format. These surfaces were used to define shells for the insert walls in a CAD program. Features were added to allow the inserts to be filled and mounted in the phantom. The liver insert also had mount points added to allow tumours to be positioned inside it. The inserts were printed in an acrylic photopolymer by Shapeways, Inc (`www.shapeways.com`), a commercial 3D printing service. This material was chosen as it has similar attenuation properties to water in the range of energies

relevant to SPECT imaging. Figure 3.1 shows stages of production of the phantom. The

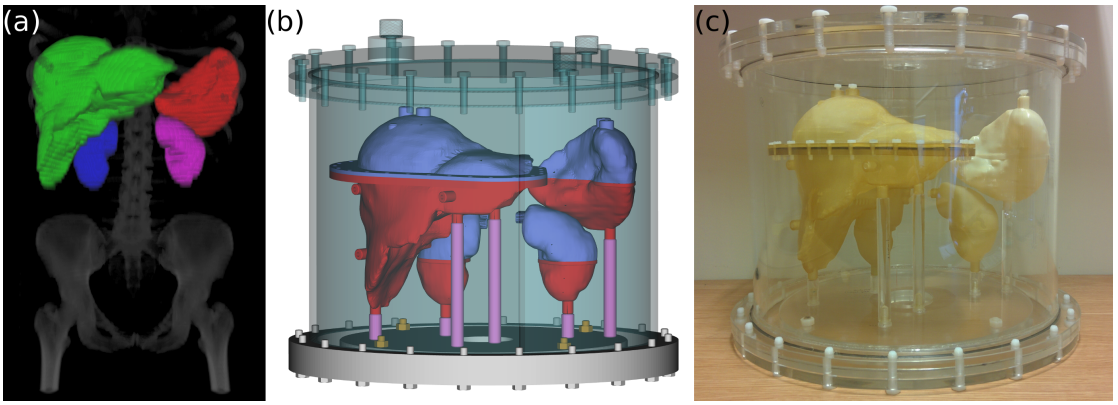

FIGURE 3.1: The stages of producing the phantom showing (a) an anterior view of the segmented CT scan; (b) the CAD model of the phantom and (c) a photograph of the assembled phantom. This figure is taken from reference [23].

phantom was designed with a removable base plate to allow multiple organ configurations to be mounted. The phantom body external to the organ inserts can be filled with activity to represent background activity in the patient blood pool and surrounding tissues.

3.2 Experimental phantom imaging

For all the scans described the inserts were filled with a solution of ^{177}Lu. The inserts were imaged both alone and assembled in the anatomically-representative configuration. The assembled organs were imaged with and without background activity to allow the impact of spill-in of counts to be assessed. Spill-in is an effect where counts originating outside a region are detected as coming from within it. In the scans of the assembled phantom the inserts and background were filled with anatomically representative activities, shown in Table 3.1. All scans were performed once. All the images were acquired using standard clinical parameters for a clinical ^{177}Lu-DOTATATE post-therapy scan on a GE Infinia Hawkeye 4 SPECT/CT scanner. The scan parameters are shown in Table 3.2. Projections were acquired of the 208 keV and 113 keV photopeaks, along with adjacent scatter windows, using MEGP collimators. Hybrid CT scans were acquired immediately after the SPECT scan. All images were reconstructed on a GE Xeleris system using an OSEM algorithm with 4 iterations and 10 subsets. These settings correspond to the standard clinical protocol for ^{177}Lu imaging. Images were reconstructed with only AC applied and with both AC and SC applied. No resolution recovery was used as it was not available when the work was started.

The scans of the inserts alone were used to calculate patient-specific calibration factors. The kidney and spleen inserts were imaged mounted centrally in an elliptical Jaszczak

TABLE 3.1: The administered activities in the inserts at the beginning of each scan when the inserts were imaged alone, assembled without background activity and assembled with background activity (BG).

Insert	Activity (MBq)			Activity concentration (MBq/ml)		
	Calibration scan	Phantom scan	Phantom scan with BG	Calibration scan	Phantom scan	Phantom scan with BG
Liver	389 ± 8	352 ± 7	348 ± 7	0.203 ± 0.004	0.184 ± 0.004	0.182 ± 0.004
Spleen	842 ± 17	121 ± 3	121 ± 3	0.750 ± 0.016	0.312 ± 0.007	0.309 ± 0.007
Left kidney	414 ± 9	129 ± 3	128 ± 3	2.47 ± 0.05	0.769 ± 0.019	0.761 ± 0.018
Right kidney	388 ± 8	121 ± 3	120 ± 3	2.50 ± 0.05	0.781 ± 0.020	0.773 ± 0.020
Background	NA	NA	813 ± 16	NA	NA	0.0358 ± 0.0007

TABLE 3.2: SPECT tomographic acquisition parameters corresponding to a clinical ^{177}Lu-DOTATATE post-therapy scan.

Pixels	128×128
Number of views per head	30 (60 in total)
Time per view	40 s
Rotation radius	25 cm
Photopeak windows	113 keV $\pm$ 10%, 208 keV $\pm$ 10%
Scatter windows	181 keV $\pm$ 3%, 236 keV $\pm$ 3%
OSEM settings	4 iterations, 10 subsets

phantom for the calibration scans. The spleen was additionally imaged in the anatomical position. The liver insert was too large to mount in the Jaszczak phantom so was imaged in its anatomical position. The phantom body was filled with water for the calibration scans to provide attenuation and scattering similar to human tissue.

To calculate the patient-specific calibration factors each insert was outlined on the CT scan and the resulting VOI transferred to the accompanying SPECT image. The total number of counts in the VOI was then recorded. Theoretical values of calibration factor were calculated using the VOI for each insert and for spheres of the same volume as each insert. Comparison of these values shows the impact of the change of shape from a sphere. The value of cf_{true} (11.74 ± 0.02 cps/MBq) was determined in reference [22].

The patient specific calibration factors were used to quantify the activity in the inserts in the scans of the assembled phantom with and without background. The activities were also quantified using calibration factors for a 113 ml sphere and inserts based on the Cristy and Eckerman phantom set (referred to as the C&E phantoms) [22]. The quantified activities were used to calculate recovery factors for each insert. The activities were also used to calculate the dose to each organ using clinical dosimetry software, OLINDA/EXM 1.0. The masses of the organs in OLINDA/EXM 1.0 were scaled based on the volumes of the VOIs used to define the inserts. As the same S-factors are used for all the dose calculations the changes in dose are proportional to the changes in recovered activity.

3.3 Monte Carlo simulation of dosimetry

A voxelised simulation of dosimetry was developed in GATE v8.0. The simulation takes voxelised CT-format images as input and records the dose to each voxel using the `DoseActor` feature of GATE. The recommended physics model in GATE for this energy range, 'EM option 3', was used for all simulations. To validate the simulation a voxelised version of the Cristy and Eckerman phantom was created, with voxels the same size as

those in the CT scan used to define the CATIE organs. The volumes of the voxelised C&E organs are all within 1 % of the volumes given in reference [49]. For both the validation and patient-specific simulations only the torso, liver, spleen and kidneys were considered. Each organ was simulated containing 150 MBq of activity for one second of simulated time. The output of these simulations was used to calculate the dose to each of the liver, spleen and kidneys. These doses were compared to doses calculated using OLINDA/EXM 1.0. A comparison of the calculated doses is shown in Table 3.3. The uncertainties on the output of OLINDA/EXM 1.0 are approximately 5 % [10]. The statistical uncertainty on the gamma doses and beta self-doses calculated using the patient-specific simulation is small, ∼0.02 % and ∼0.008 % respectively. Proportionally fewer beta particles travel far enough to reach other organs, so the uncertainty is larger for beta cross-doses, ∼1 % to ∼7 %. The doses calculated for validation are consistent with OLINDA/EXM to within 5 %. This agreement is consistent with other comparisons between different Monte Carlo codes [61–63].

To set up a patient-specific simulation of dose the binary VOIs used to define the patient inserts were used to define the source and geometry. A VOI defining the torso region of the patient was also added. All the material of the torso was set to be 'soft tissue' as defined in [49]. The activity distribution in each organ was assumed to be homogeneous.

3.4 Results

Table 3.4 shows calibration factors for the patient-specific inserts. Significant differences can be seen between the calibration factors of the liver and spleen and those of the kidneys. There is also a significant difference in the calibration factors of the spleen in the central and anatomical positions. This difference in calibration factor impacts the activity quantification and subsequent dosimetry. The origin of the positional dependence is examined further in Chapter 4. Figure 3.2 shows a comparison of experimental and theoretical calibration factors for each insert, along with theoretical factors for spheres of equivalent volume calculated using Equation (2.11). The differences between the theoretical calibration factors demonstrate the impact of shape for objects of the same volume.

Figure 3.3 shows recovery factors for the patient inserts for scans of the assembled phantom with and without background activity. Recovery factors are shown for activities quantified using three different calibration factors for each organ: a 113 ml sphere; the corresponding C&E insert and the patient-specific insert. It can be seen that the inclusion of background gives a slight increase in recovery factor. All the calibration factors used were suitable for the kidneys. This is to be expected as they are a similar volume and

TABLE 3.3: Comparison of ^{177}Lu absorbed dose calculations for C&E organ models from MC simulation and OLINDA/EXM. The calculations use 150 MBq of activity in each individual organ. The MC simulation uses a voxelised geometry with $0.7812 \times 0.7812 \times 3$ mm^3 voxels. The uncertainties on the output of the simulation are purely statistical. This table is taken from [23].

Source organ	Target organ	Dose			
		OLINDA/EXM (mGy/MBq)		MC simulation (% of OLINDA/EXM[a])	
		Gamma	Beta[b]	Gamma	Beta
Kidneys	Kidneys	$(1.16 \pm 0.06) \times 10^{0}$	$(6.54 \pm 0.33) \times 10^{1}$	95	100.8
Liver	Liver	$(4.31 \pm 0.22) \times 10^{-1}$	$(1.02 \pm 0.05) \times 10^{1}$	100	103.5
Spleen	Spleen	$(2.10 \pm 0.10) \times 10^{0}$	$(1.07 \pm 0.05) \times 10^{2}$	97.5	101.2
Kidneys	Spleen	$(1.54 \pm 0.08) \times 10^{-1}$	N/A	98.4	$(5.65 \pm 0.09) \times 10^{-4}$
Spleen	Kidneys	$(1.54 \pm 0.08) \times 10^{-1}$	N/A	98.2	$(5.63 \pm 0.07) \times 10^{-4}$
Kidneys	Liver	$(6.74 \pm 0.34) \times 10^{-2}$	N/A	100.7	$(1.888 \pm 0.017) \times 10^{-4}$
Liver	Kidneys	$(6.74 \pm 0.34) \times 10^{-2}$	N/A	100.2	$(1.89 \pm 0.04) \times 10^{-4}$
Liver	Spleen	$(1.63 \pm 0.08) \times 10^{-2}$	N/A	103.8	$(3.04 \pm 0.22) \times 10^{-5}$
Spleen	Liver	$(1.63 \pm 0.08) \times 10^{-2}$	N/A	103.8	$(3.08 \pm 0.07) \times 10^{-5}$

[a] Given in units of mGy/MBq where component is not reported by OLINDA/EXM.
[b] No beta component of cross-dose reported by OLINDA/EXM.

TABLE 3.4: Calibration factors for the patient organ models filled with ^{177}Lu solution for images reconstructed with attenuation and scatter correction applied. The EM2 data in this table are taken from [23].

Insert	Calibration factor (cps / MBq)	
	EM1	EM2
Liver	7.91 ± 0.17	7.54 ± 0.17
Spleen (central position)	7.06 ± 0.14	7.00 ± 0.14
Spleen (anatomical position)	7.98 ± 0.23	7.98 ± 0.18
Left kidney	6.49 ± 0.20	6.43 ± 0.18
Right kidney	6.15 ± 0.16	6.19 ± 0.15

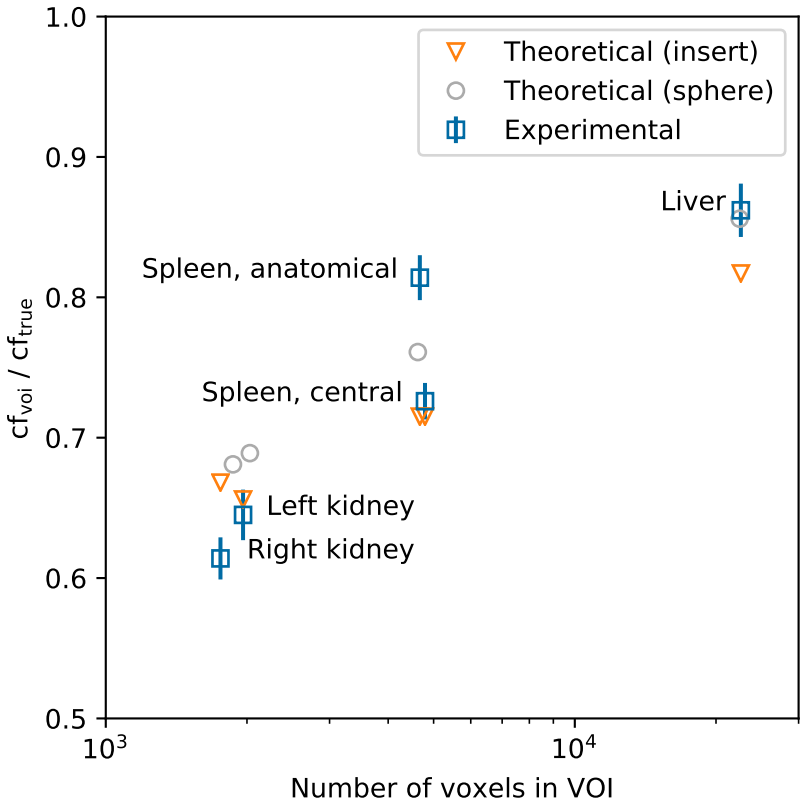

FIGURE 3.2: Theoretical and experimental calibration factors for the CATIE inserts, and theoretical calibration factors for spheres of equivalent volume. The calibration factors for EM2 were used.

shape as the sphere and C&E kidneys. The similarity of calibration factors for spheres and the C&E kidney models has previously been reported in [21]. For the liver and spleen the sphere calibration factor is unsuitable. The liver and spleen are much larger than the sphere so there will be significant differences in the impact of partial volume effects. For the liver both the C&E and patient-specific calibration factors are suitable. It can be seen that the only suitable calibration factor for the spleen is the one in the anatomical position. It should be noted that the calibration factor used for the C&E spleen was calculated with the spleen insert in a central position.

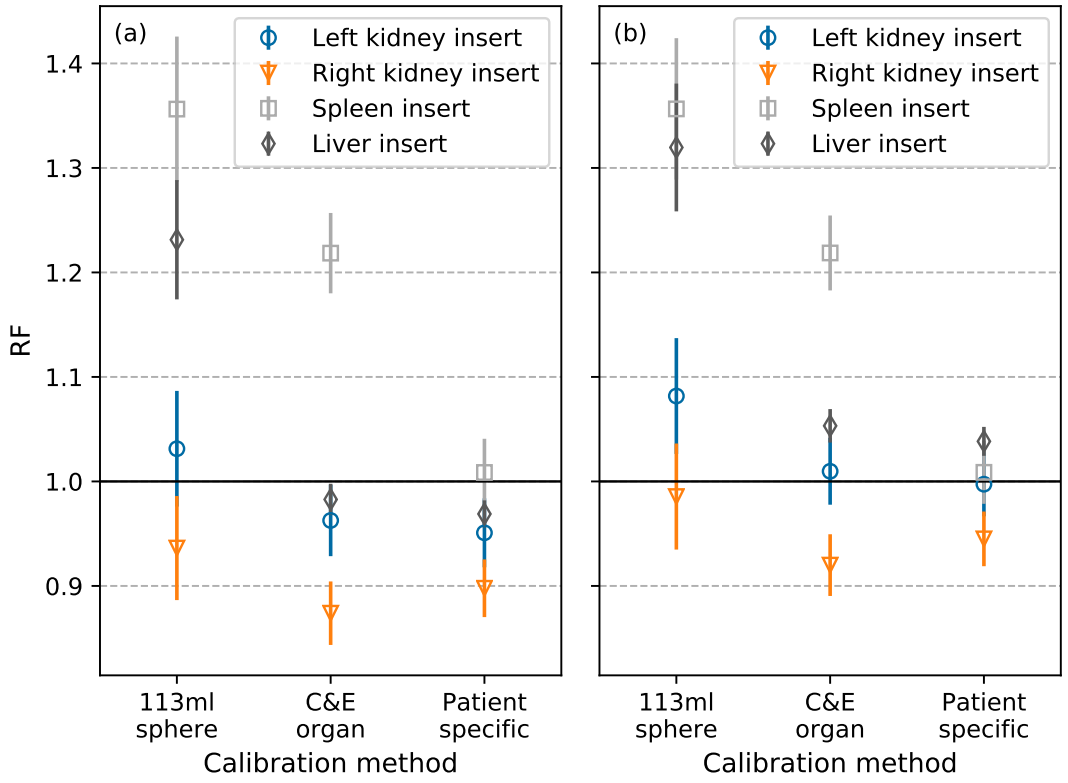

FIGURE 3.3: The recovery factors for each insert for scans performed (a) without and (b) with background activity in the phantom. The recovery factors were calculated using images of the EM2 photopeak. There is a clear improvement for the liver and spleen when the organ- and patient-specific calibration factors are used.

Figures 3.4 and 3.5 show the self- and cross-doses to all the organs in the phantom. For the kidneys the doses to each kidney are shown for the Monte Carlo calculations. The doses are calculated using OLINDA/EXM 1.0 and the quantified activities (points) and the patient-specific Monte Carlo simulation. The doses were also calculated in OLINDA/EXM 1.0 using the administered activity. The vertical range surrounding the line represents the uncertainty on the Monte Carlo dose calculation. This is dominated by the uncertainty on the activity in each insert. The doses shown include both the beta and gamma components. The dominant contribution to the dose for each organ is the

self-dose which is approximately 1000 times greater than the cross-dose. The dominant component of the total dose is from beta particles, with gamma rays contributing between 2 and 5 %. The beta component of cross dose is negligible for ^{177}Lu, and is not reported by OLINDA/EXM 1.0 for these calculations. Beta particles contribute 96 to 98 % of the self-dose to each organ. All the recovered activities are those from the scan with background as that is the physiologically representative case. Table 3.5 shows the total dose to each organ. While the best-case calculations with OLINDA/EXM 1.0 agree with the patient-specific Monte Carlo simulation, this is only the case if appropriate calibration factors are used.

TABLE 3.5: Total absorbed dose from ^{177}Lu, calculated using the patient specific MC simulation and OLINDA/EXM with different activity calibration factors. This table is taken from reference [23].

Organ	Dose (mGy/MBq)				
	Sphere cf	C&E cf	Patient cf	Administered activity	MC simulation
Liver	6.9 ± 0.5	5.51 ± 0.31	5.43 ± 0.32	5.23 ± 0.28	5.11 ± 0.04
Spleen	11.6 ± 0.8	10.4 ± 0.7	8.6 ± 0.6	8.5 ± 0.5	8.25 ± 0.12
Kidneys	22.0 ± 1.5	20.6 ± 1.3	20.7 ± 1.3	21.3 ± 1.3	20.64 ± 0.24
Left kidney	NR	NR	NR	NR	20.54 ± 0.31
Right kidney	NR	NR	NR	NR	20.8 ± 0.4

3.5 Discussion

It can be seen in Table 3.4 that the calibration factor is dependent on the shape and size of the insert. This has been previously reported in references [1, 21, 22]. Figure 3.2 also demonstrates the impact of shape on calibration factor. Table 3.4 also shows that there is a dependence on radial position in the calibration factor. The origin of this dependence is investigated further in Chapter 4. It should be noted that the subsequent calculations of recovery factor and activity were done using the patient spleen in the anatomical position.

Figure 3.3 shows the recovery factors for scans (a) without and (b) with activity in the background of the phantom. The presence of background activity results in an increase in the recovery factor, corresponding to an increase in counts in the VOI. This is due to counts from the background 'spilling in' to the VOI. In clinical scenarios there will always be background surrounding the patient organs of interest so the data with background were used to perform the dosimetry calculations. All three calibration factors tested were suitable for the kidneys. This is in agreement with previous work demonstrating the similarity of the C&E kidneys to spheres [21]. For the spleen only the patient-specific calibration factor gives an acceptable recovery factor. However the C&E spleen calibration

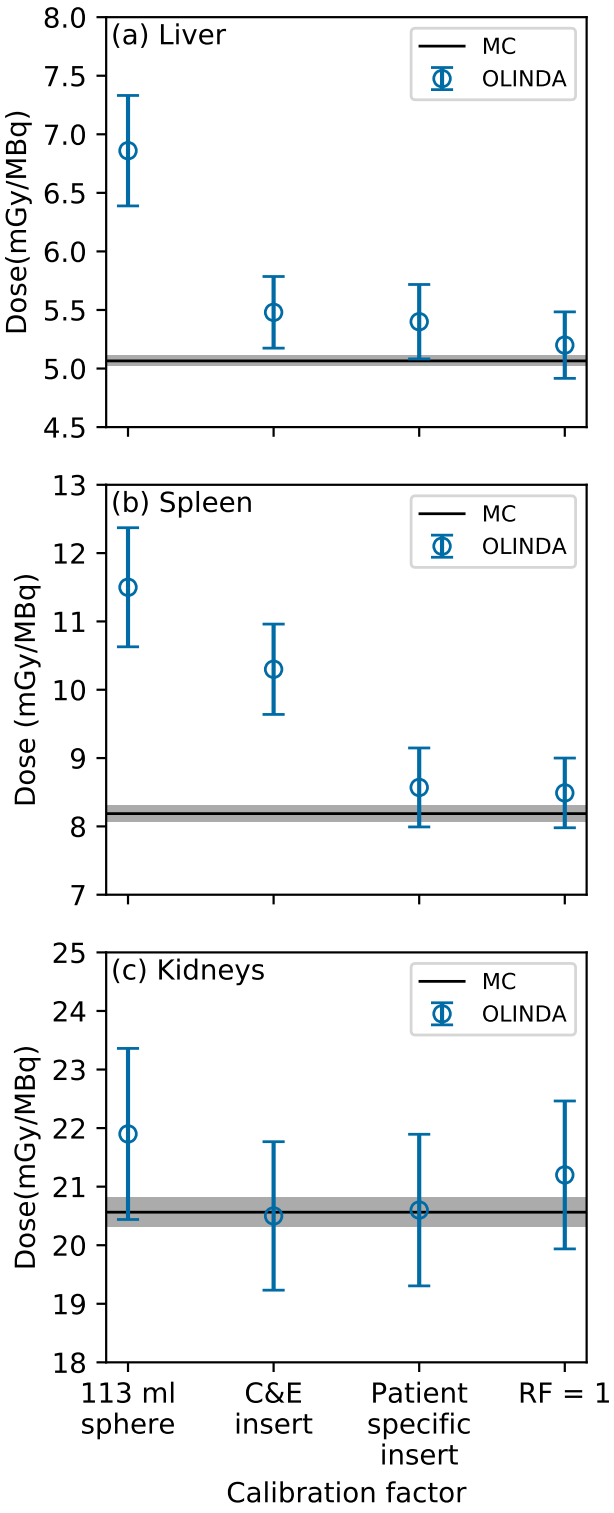

FIGURE 3.4: The self-doses to each organ in CATIE, calculated using OLINDA/EXM (points) and a patient-specific Monte Carlo simulation (line). The shaded regions indicate the uncertainty on the doses calculated using the patient-specific Monte Carlo simulation. It can be seen that for all the organs considered the self-doses calculated using OLINDA/EXM are consistent with the patient-specific Monte Carlo simulation if suitable calibration factors are used. The changes in the doses reported by OLINDA/EXM are solely due to the differences in the quantified activity used to calculate the dose. This figure is taken from reference [23].

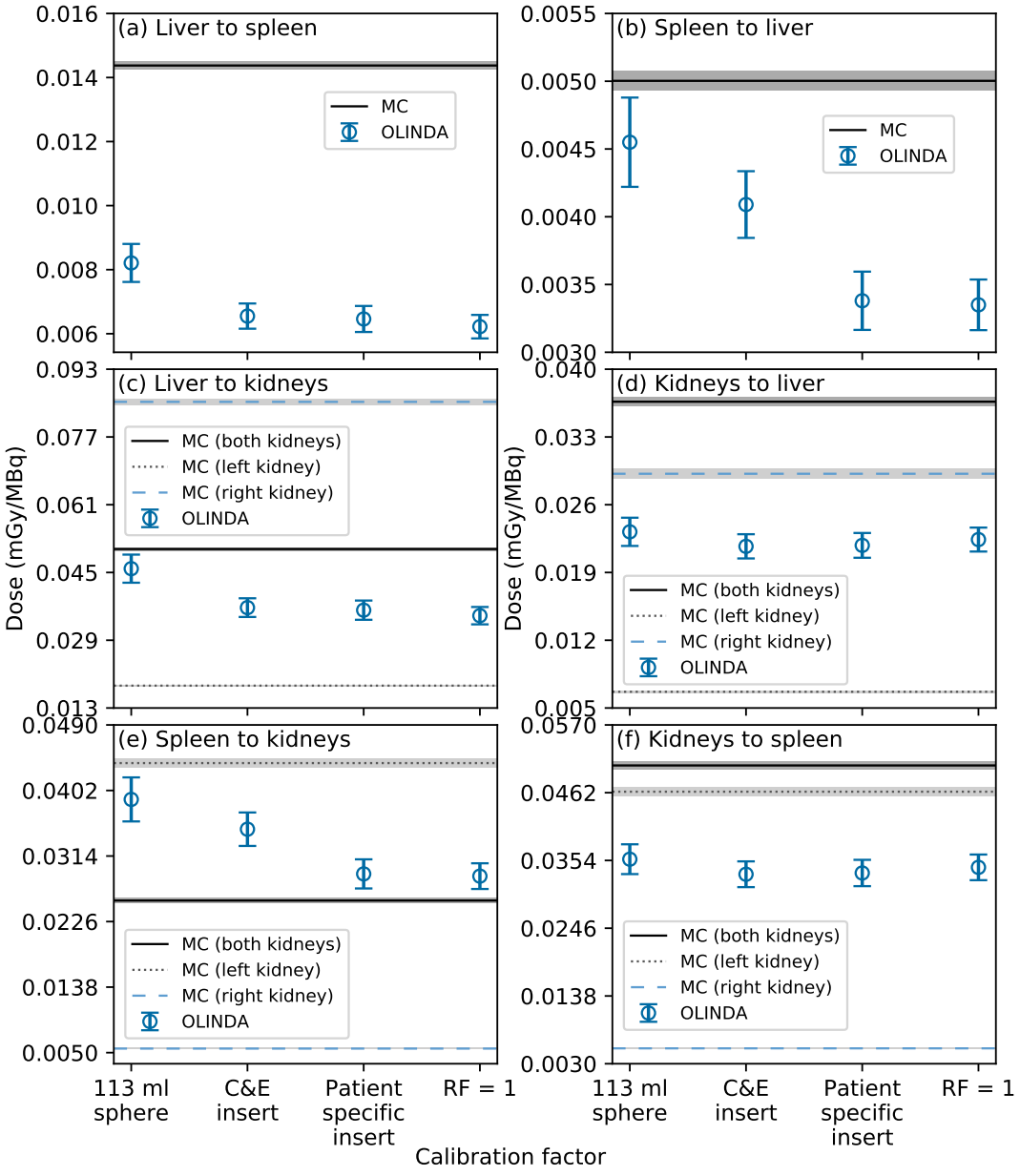

FIGURE 3.5: The cross-doses to each organ in CATIE, calculated using OLINDA/EXM (points) and a patient-specific Monte Carlo simulation (line). The shaded regions indicate the uncertainty on the doses calculated using the patient-specific Monte Carlo simulation. For some source-target pairs the doses calculated using OLINDA/EXM are not consistent with those calculated using the patient-specific Monte Carlo simulation. The changes in the doses reported by OLINDA/EXM are solely due to the differences in the quantified activity used to calculate the dose. This figure is taken from reference [23].

factor was calculated with the insert mounted centrally in an elliptical Jaszczak phantom. It would be expected that a radial displacement of the C&E spleen insert would improve agreement with the patient insert. This is seen when the insert is translated, however when the insert is positioned in the correct orientation the improvement is removed. This is discussed further in Chapter 4. The data from the scan with the insert mounted centrally are used for the rest of this chapter. It is important to note that reducing the random uncertainty in a calibration factor will not improve it's suitability. The offset is due to the shape and size of the calibration insert, not the uncertainty in the calibration factor.

In Figures 3.4 and 3.5 the doses calculated using OLINDA/EXM 1.0 all use the same S-factors so any differences are solely due to differences in the cumulated activity used in the dose calculations. This in turn is solely dependent on the suitability of the calibration factor used. The comparison shows the impact of the use of unsuitable calibration factors on dose calculations. The doses calculated from the patient-specific Monte Carlo simulation use the activity calculated to be in the inserts based on measurements taken while filling the inserts. Comparing these to the calculations using OLINDA/EXM 1.0 and the same activity allow the pre-computed S-factors in OLINDA/EXM 1.0 to be compared to patient-specific S-factors. In Figure 3.4 the self-doses calculated with OLINDA/EXM 1.0 agree with the patient-specific Monte Carlo calculations for all three organs. This is expected as the self-dose is dominated by the dose from beta particles which have a short range in tissue, approximately 2 mm, and therefore deposit almost all of their energy in the source region. In nuclear medicine it is often assumed that all of the energy from beta particles is deposited in the source region [3]. The shape of the organs is largely unimportant so long as the mass of the organ is scaled in OLINDA/EXM 1.0. In contrast the cross-dose, shown in Figure 3.5, is dominated by gamma rays. As a result differences due to the organ shape and position are apparent. For all source-target pairs apart from the spleen to kidneys there are significant differences between the doses calculated using OLINDA/EXM 1.0 and the patient-specific Monte Carlo simulation. In OLINDA/EXM 1.0 the kidneys are treated as a single organ, with the activity in both kidneys divided equally between them. The dose is only considered to the combined kidney organ. In cases where the kidneys are the target organ (Figure 3.5 parts (c) and (e)) the difference in doses to the left and right kidneys is concealed. This is true even when there is agreement between OLINDA/EXM 1.0 and the patient-specific Monte Carlo calculation as in Figure 3.5 part (e). When the kidneys are the source organ, problems will arise if one kidney has higher uptake than another, and the assumption that the activity is distributed equally does not hold. Table 3.5 shows the total dose to each organ calculated using OLINDA/EXM 1.0 and the patient-specific Monte Carlo simulation. The good agreement when a patient-specific calibration factor is used is to be expected as

the dose is dominated by the beta-component which is not strongly influenced by shape. The impact of an isotope like ^{131}I, which emits more gamma rays of higher energy on S-factors is examined in Chapter 5. As for the activity recovery, a lower uncertainty on the dose calculation will not improve the agreement between the S-factors.

For all the organs the doses are incorrect if accurate activity quantification is not done. Provided mass correction is applied while calculating the doses the S-factors used in OLINDA/EXM 1.0 are suitable for this patient. Over-estimations of the quantified activity of up to 35 % are observed if inappropriate calibration factors are used. Calibration factors appropriate to the patient must be used if accurate dosimetry is to be done.

The remainder of this page was intentionally left blank.

Chapter 4

Investigation of the positional dependence of calibration factor

4.1 Introduction

A dependence of calibration factor on spatial position was observed in Chapter 3. A similar effect has been observed for spheres filled with ^{131}I and ^{177}Lu in reference [64]. In reference [64] spheres were displaced up to 12.8 cm from the centre of an elliptical Jaszczak phantom and imaged on GE Infinia Hawkeye, GE Discovery 670 and Siemens Symbia T cameras. These images were then reconstructed using native and vendor neutral software. The positional dependence was suggested in reference [64] to be due to the depth-dependent spatial resolution (DDSR) of the SPECT scanners. However, data were presented in table 1 of reference [64] for a scanner and reconstruction combination in which no positional dependence was apparent, and for which no resolution recovery was used. The lack of dependence for one scanner and reconstruction combination suggests that the dependence is not due to the DDSR of SPECT scanners. This chapter investigates the origin of this effect. There are multiple possible causes of the effect, relating to the geometry of the scanner and the reconstruction performed. The possible effects examined are: the depth-dependent spatial resolution of the collimator; PMT signal processing; the choice of reconstruction algorithm implementation and attenuation correction method and the scatter correction method used.

In this chapter a combination of experimental imaging and Monte Carlo simulation of ^{177}Lu imaging was used to isolate the impact of these effects. Monte Carlo methods allow the simulation of un-physical images, such as with attenuation or scatter removed. Calibration factors for images of inserts filled with ^{99m}Tc solution were also calculated to investigate the behaviour of the scanner for the isotope for which it may be considered to

have been optimised. The inserts were imaged in the centre of phantoms and radially displaced similarly to those in reference [64]. It is important to note that if a phantom is positioned centrally then a radial displacement of an insert has two effects: the distance from the insert to the detector changes and the insert is closer to the edge of any attenuating material in the phantom. Our paper investigating the positional dependence has been published in Nuclear Medicine Communications [65].

4.2 Monte Carlo simulation of imaging

A model of the GE Infinia Hawkeye 4 camera, previously described and validated in reference [66], was used for the simulations of SPECT imaging. Figure 4.1 shows a visualisation of the model of the SPECT scanner used in the Monte Carlo simulation. For this work the model was used in GATE v8.0. The model was validated in the updated version of GATE by comparing the simulation output to experimental data. For the simulation of imaging a pre-built physics list was not used. This was due to a bug which caused photon scatter to be incorrectly recorded if the atomic de-excitation process was activated. A user-defined physics list allows individual physical process to be selected. The exclusion of atomic de-excitation results in the absence of X-rays in the simulation but as the energies of the X-rays which are produced are below the energy ranges of interest for imaging this does not impact the simulation of imaging. The complete history of each detected photon is known, allowing projection sets to be created with all scattered events removed. Removing all scattered events allows the investigation of the impact of attenuation correction only in the reconstruction step. Images can also be calculated for activity distributions with no attenuating material present. The simulated model does not include signal processing of the PMT output, so the comparison used for validation can assess the impact of this. The simulation in vacuum, with no attenuating material, then only shows the impact of the collimator geometry on the imaging. Simulated images reconstructed with attenuation correction and triple energy window scatter correction are referred to as Sim. AC TEW. Simulated images with all scattered events removes are referred to as Sim. AC MCSC.

The simulation can use either a geometric model or experimental CT data to define the geometry of the phantom and inserts. Similarly the source can either be defined mathematically as a geometric model or voxelised, based on a suitably-modified CT images. To simulate a voxelised geometry based on a CT image, GATE requires calibration information to convert the CT voxel values to material definitions. Two sets of calibration data are required: the relationship between CT number and mass density in $\mathrm{g\,cm^{-3}}$ and the mapping from CT number to material. The materials and their chemical composition

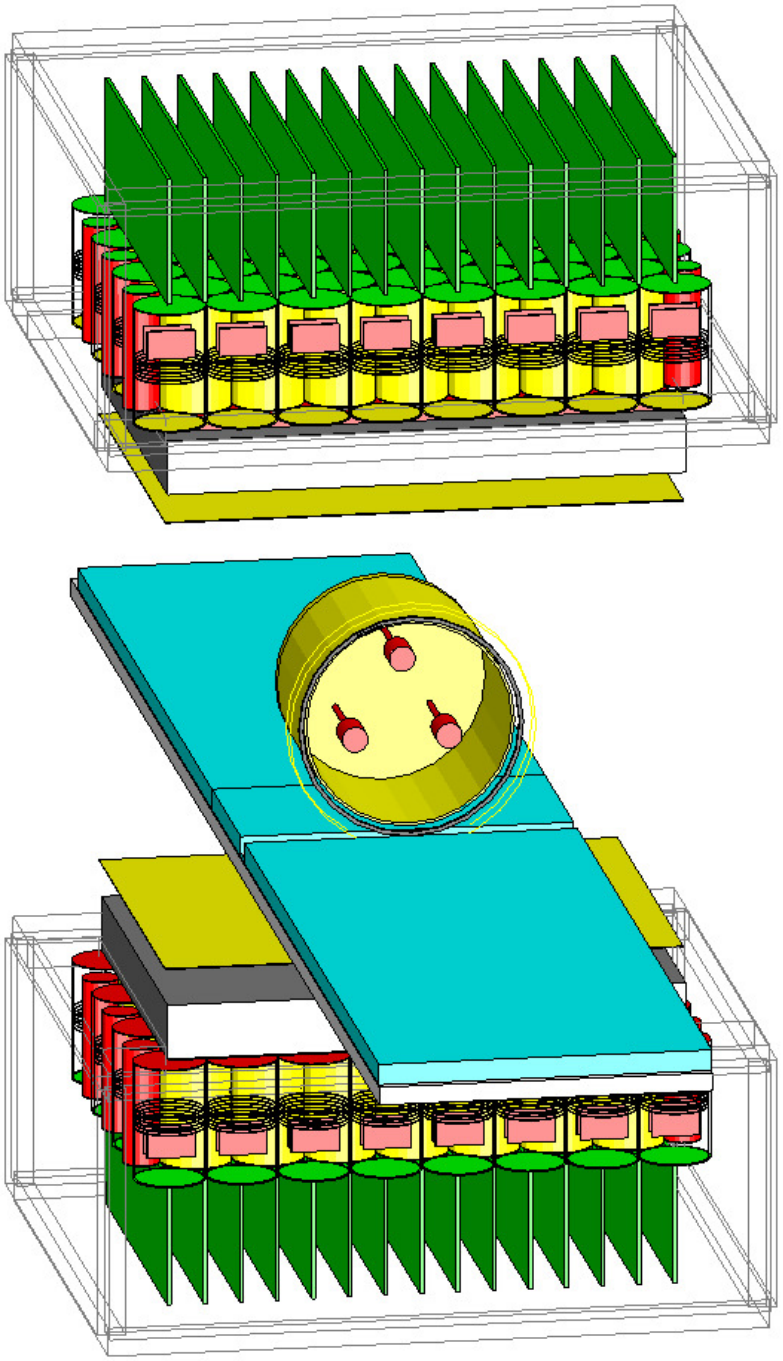

FIGURE 4.1: A visualisation of the camera geometry in the simulation. Also shown is a Jaszczak phantom with cylindrical inserts and a geometrical model of the patient bed. These may be removed and replaced with voxelised geometry based on CT scans.

are defined separately. GATE uses this information to produce ranges of CT numbers with the same mass density and material composition. A density tolerance can be set to control how many different materials are created. Voxelised sources were defined in GATE by setting the activity per voxel for a range of voxel values. To define a uniform source region a VOI of the required region is created. The voxels in the VOI are then set to a value outside the range of CT numbers in the unaltered CT image. The required activity per voxel is then calculated using the number of voxels in the VOI.

4.2.1 Validation of simulation

The simulation was validated by comparing simulated and experimental projection sets and energy spectra. Figure 4.2 shows a comparison of experimental and simulated energy spectra for a 113 ml sphere filled with ^{99m}Tc solution in a water-filled Jaszczak phantom. The lack of an emission peak between 70 and 80 keV is due to the absence of lead X-rays in the simulation. The disagreement below 70 keV is likely due to the efficiency and calibration of the physical camera. The camera is calibrated to the 140 keV gamma ray from ^{99m}Tc in the morning, and the calibration may drift over the course of the day. This region is not used for any calculations. Above 80 keV the agreement between the simulation and experiment is reasonable. Figure 4.3 show simulated energy spectra for ^{99m}Tc using the 'EM Option 3' and 'Penelope' physics models respectively. For both, most of the events are recorded as unscattered. Further, there is a clear over-production of X-rays in the 70 to 80 keV region. Figure 4.5 shows a comparison of real and simulated energy spectra for three 10 ml cylinders filled with ^{177}Lu solution in a cylindrical Jaszczak phantom. This is the same geometry as shown in Figure 4.1, but a voxelised geometry and source were used. There is reasonable agreement above the 80 keV region, as lead X-rays are not simulated. Figures 4.6 and 4.7 show the total number of counts in each projection of experimental and simulated images of the C&E spleen containing ^{177}Lu solution in the edge position. The changes in the number of counts in each projection is due to the detector heads rotating around the phantom and passing both beneath the bed and to the side of the phantom away from the insert. The close agreement indicates that the modelling of materials and photon transport through the phantom and detector is accurate.

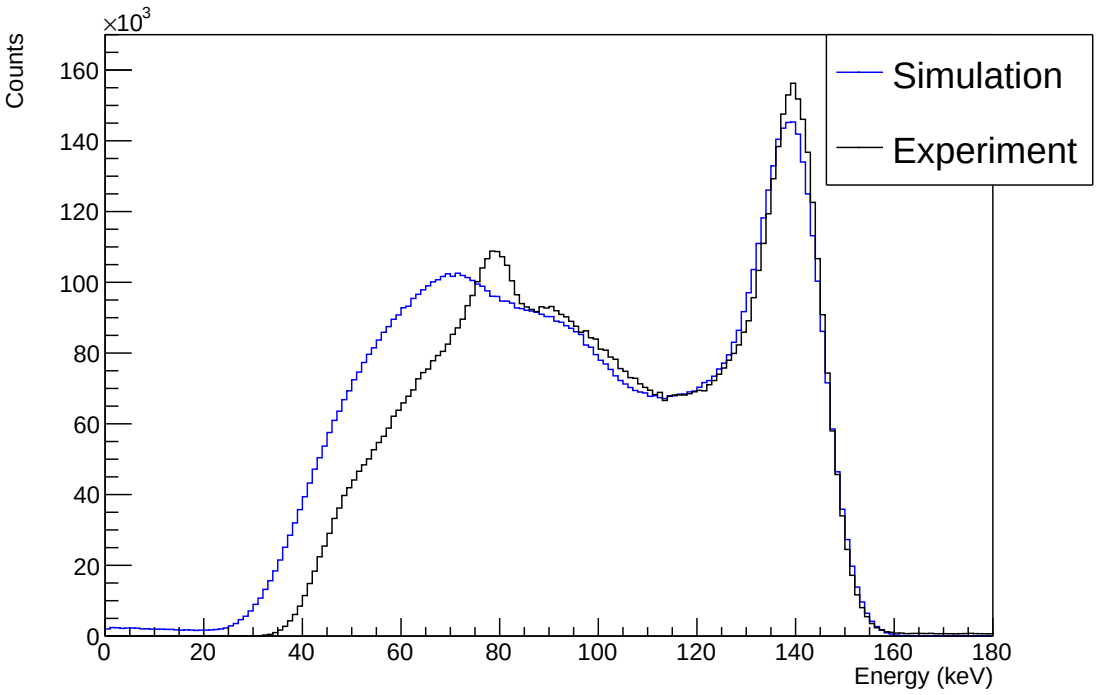

FIGURE 4.2: The simulated and experimental energy spectra for a 113 ml sphere filled with ^{99m}Tc solution in a water-filled Jaszczak phantom. The energy spectra are normalised to have the same number of counts in the region from 120 to 160 keV.

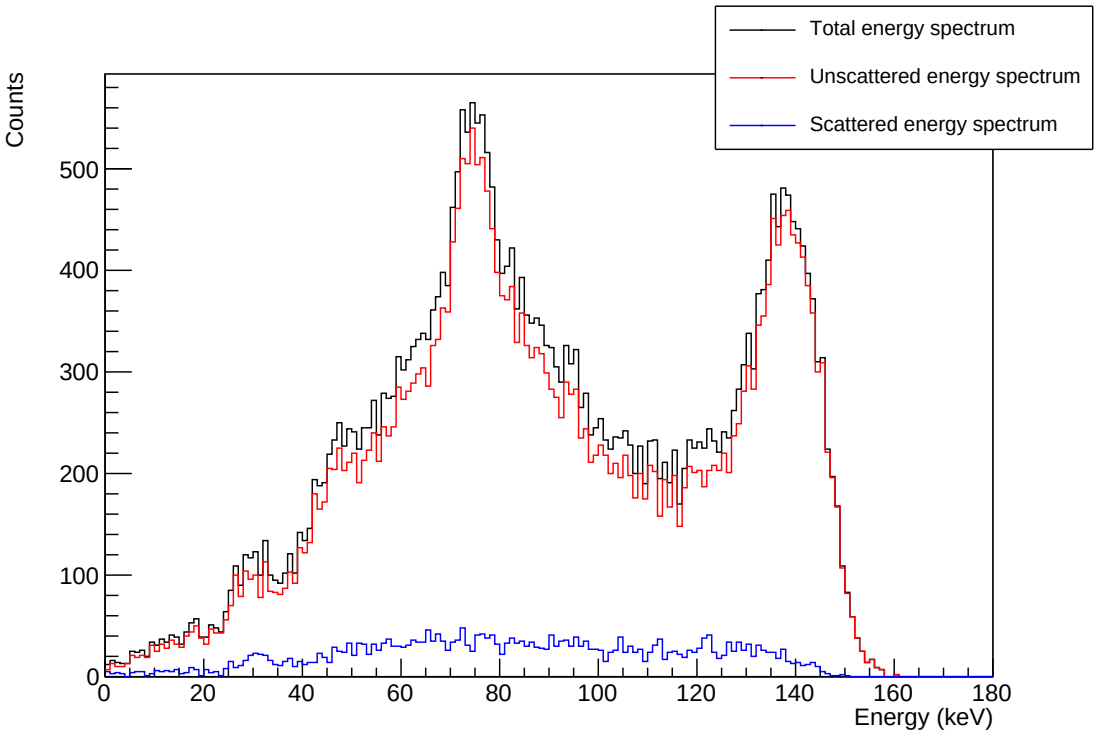

FIGURE 4.3: A simulated energy spectrum of ^{99m}Tc using the 'EM option 3' physics model, showing the scattered and unscattered components. It can be seen that the recording of scatter is not correct.

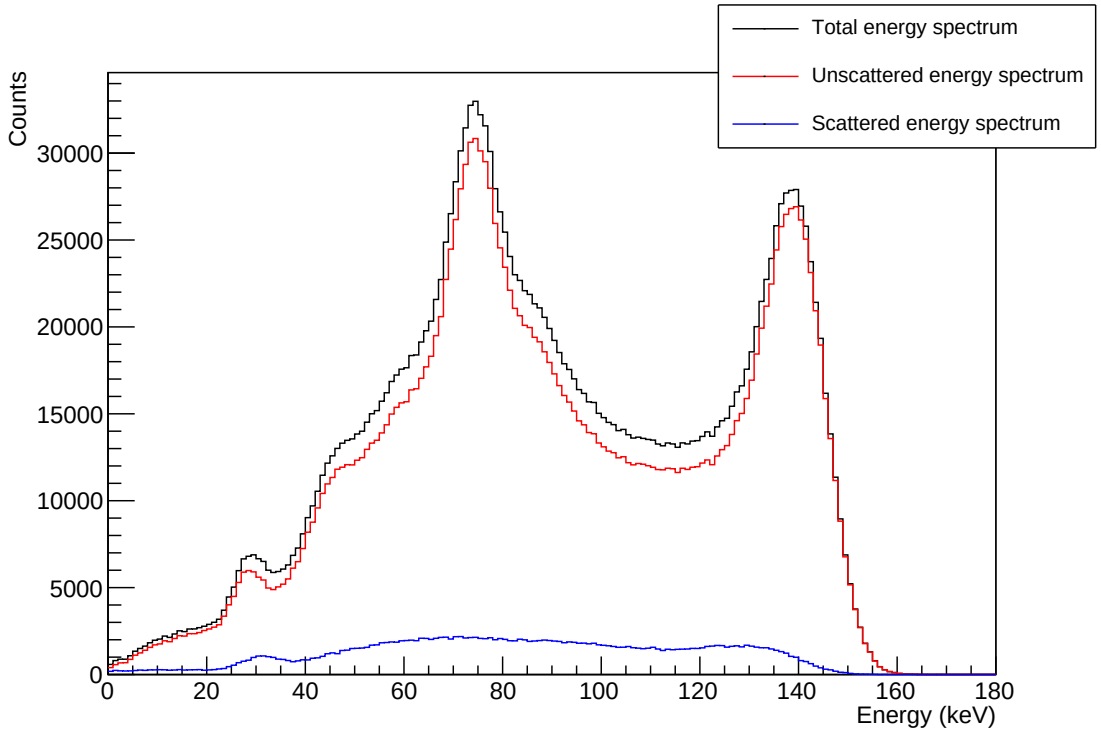

FIGURE 4.4: A simulated energy spectrum of ^{99m}Tc using the 'Penelope' physics model, showing the scattered and unscattered components. It can be seen that the recording of scatter is not correct.

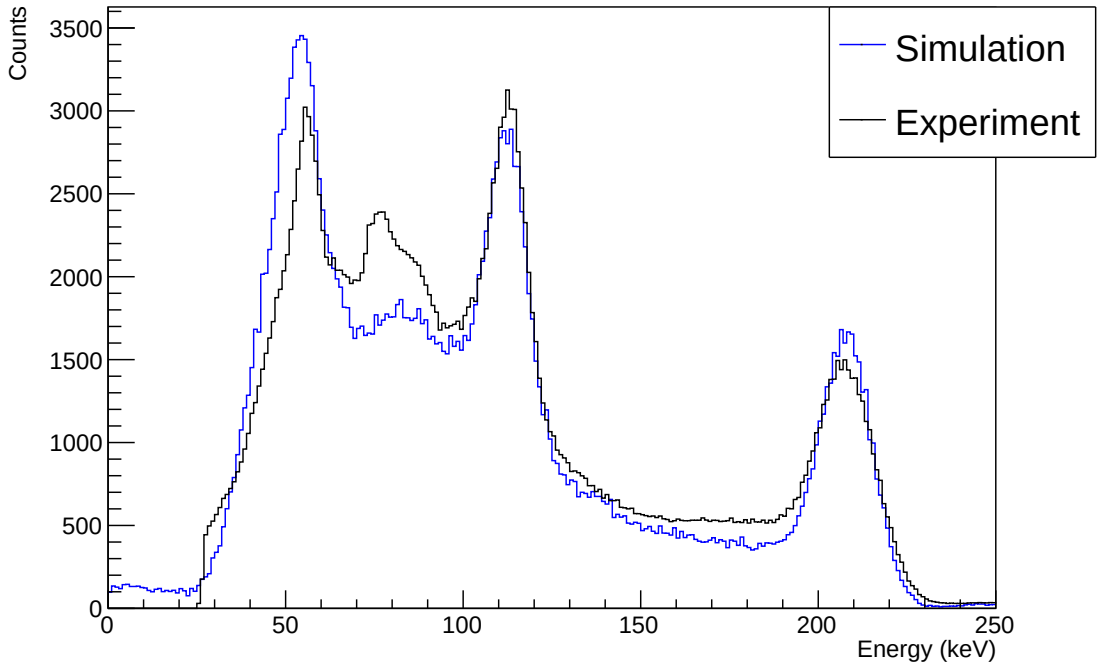

FIGURE 4.5: The simulated and experimental energy spectra for a three 10 ml cylinders filled with ^{177}Lu solution in a water-filled Jaszczak phantom. The energy spectra are normalised to have the same number of counts in the region from 190 to 220 keV.

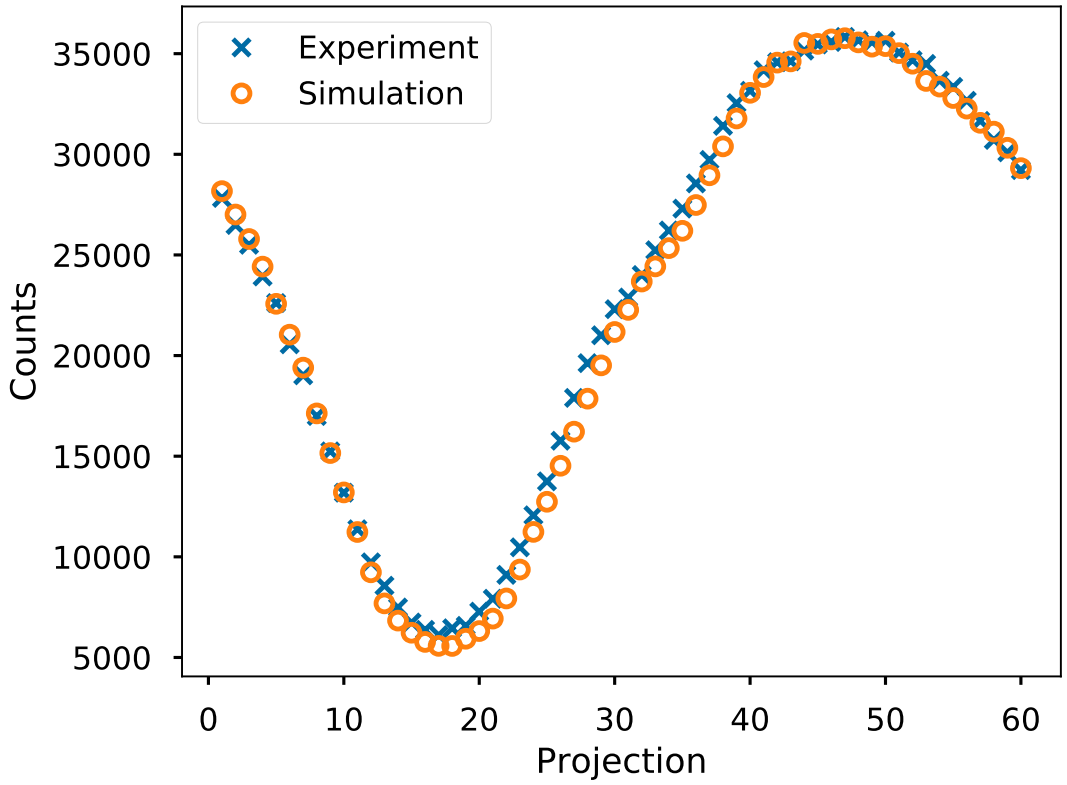

FIGURE 4.6: The total counts in each projection of experimental and simulated images of the C&E spleen in the edge position for the EM2 window. The close agreement indicates that the photon transport model is accurate.

4.3 Experimental imaging

4.3.1 ^{177}Lu imaging

Experimental data were collected for a selection of phantom inserts in different positions and orientations using a GE Infinia Hawkeye 4 SPECT/CT scanner. The imaging settings used are shown in Table 3.2. These data were reconstructed with different settings applied on two different clinical systems. Calibration factors were calculated for the whole reconstructed images and VOIs outlining the inserts. The calculation of calibration factors for the whole image removes the impact of defining the VOI on the calibration factor. Images were reconstructed on a GE Xeleris system using Volumetrix (`www.gehealthcare.com`) and a Hermes Medical Solutions system using HybridRecon (`www.hermesmedical.com`) with the settings described in Table 4.1. The two reconstruction systems are from different vendors, so will implement the OSEM algorithm and attenuation correction in different ways. The details of the implementation of these is not published. The two systems also use different methods of scatter correction. GE Volumetrix uses TEW scatter correction, performed on the projection set prior to

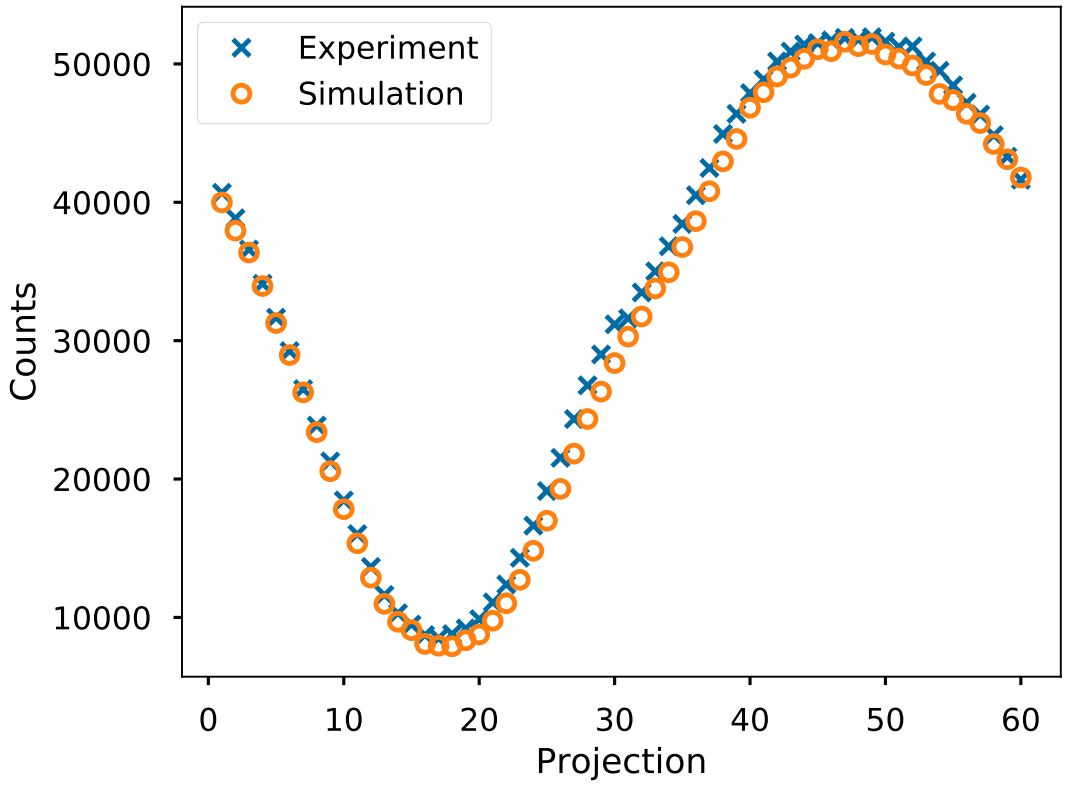

FIGURE 4.7: The total counts in each projection of experimental and simulated images of the C&E spleen in the edge position for the EM1 window. The close agreement indicates that the photon transport model is accurate.

TABLE 4.1: The reconstruction settings used for images reconstructed using GE Volumetrix and HybridRecon.

Platform	Settings used
Xeleris	Attenuation correction only (Exp. AC). Attenuation and TEW scatter correction (Exp. AC TEW) with 4 iterations and 10 subsets. Attenuation and TEW scatter correction with 5 iterations and 20 subsets.
Hermes	Attenuation correction only. Attenuation and TEW scatter correction with 4 iterations and 10 subsets. Attenuation and Monte Carlo-based scatter correction (Exp. AC MCSC) with 4 iterations and 10 subsets.

reconstruction and Hermes HybridRecon uses Monte Carlo based scatter correction. It is possible to export the TEW-corrected projection set from Xeleris and reconstruct it with the Hermes system. Neither system allows interrogation of how the attenuation correction is performed in the reconstruction. GE Xeleris outputs the attenuation map used, and Hermes HybridRecon allows the user to input a calibration of CT number to attenuation coefficient. Table 4.2 describes the inserts which were imaged, and their positions. A cylindrical Jaszczak phantom containing a uniform activity distribution was also imaged. Figure 4.8 shows transaxial slices through CT images of the inserts mounted

TABLE 4.2: The positions the inserts were imaged in and the phantoms in which they were mounted.

Insert	Position
C&E spleen	At the centre of an elliptical Jaszczak phantom. At the edge of an elliptical Jaszczak phantom. At the edge of an elliptical Jaszczak phantom in the anatomical orientation.
CATIE spleen insert	At the centre of an elliptical Jaszczak phantom. Midway between the centre and edge of an elliptical Jaszczak phantom. In the anatomical position in the CATIE phantom.
113 ml sphere	At the centre of an elliptical Jaszczak phantom. At the edge of an elliptical Jaszczak phantom.
16 ml sphere	At the centre of an elliptical Jaszczak phantom. At the edge of an elliptical Jaszczak phantom.

in the phantoms to show the positions.

4.3.2 ^{99m}Tc Imaging

The 113 ml sphere was imaged in the same positions as in Section 4.3.1, filled with a saline solution of ^{99m}Tc. Images were acquired for the 140 keV photopeak and a lower scatter window. The acquisition settings are described in Table 4.3. The images were reconstructed on a GE Xeleris system and using Hermes HybridRecon. Calibration factors were calculated for the insert in both positions using AC only and AC with the scatter correction provided in the reconstruction process. Volumetrix uses dual energy window scatter correction and Hermes HybridRecon uses a Monte Carlo based scatter correction.

4.4 Simulated data

The Monte Carlo simulation was used to address questions which could not be answered solely using experimental methods. All the scans of the inserts described in 4.3.1 were

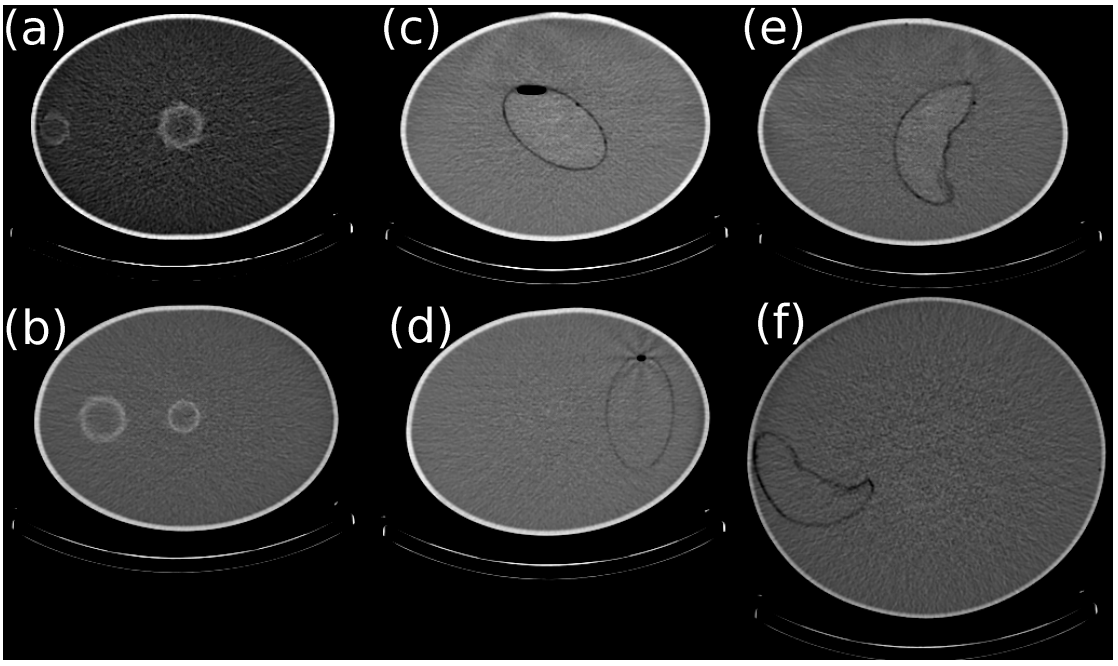

FIGURE 4.8: CT scans showing the positions of the inserts. These are the scans taken immediately after the SPECT image acquisition. (a) 113 ml sphere central, 16 ml sphere outer; (b) 16 ml sphere central, 113 ml sphere outer; (c) C&E spleen central; (d) C&E spleen outer; (e) CATIE spleen central; (f) CATIE spleen, anatomical position.

TABLE 4.3: SPECT tomographic acquisition parameters used for the scans of the 113 ml sphere filled with ^{99m}Tc.

Pixels	128×128
Number of views per head	30 (60 in total)
Time per view	20 s
Rotation radius	25 cm
Photopeak window	140 keV±10%
Scatter window	120 keV±5%
OSEM settings	4 iterations, 10 subsets

simulated using the experimental CT scan as input. The uniform Jaszczak phantom was simulated based on a geometric definition as a simulation using the CT would have taken a prohibitive amount of time. Scans of the insert sources in vacuum with no attenuating material between them and the scanner heads were also simulated. Each insert was simulated containing the true activity in the insert, or 300 MBq if the true activity was greater than 300 MBq. The 300 MBq limit was imposed to constrain the running time of the simulations whilst providing adequate statistics. The statistical uncertainty on the number of counts in a VOI was approximately 0.04 % when using 300 MBq, far less than the total uncertainty of around 1.5 %.

4.5 Results

Figure 4.9 shows calibration factors for the various inserts calculated using images reconstructed using the GE Xeleris system. It can be seen that in the simulations of the inserts in vacuum the calibration factors for each insert are consistent when the organs are translated. This is not the case when they are rotated. The impact of orientation of volumes is an interesting topic for further work but is not examined further in this thesis. A similar effect is visible in Figure 4.10 which compares the total counts per MBq in the whole SPECT field of view. In this case the calibration factors in vacuum are consistent for all inserts, positions and orientations. When attenuation correction is introduced the calibration factors for each insert differ significantly, with inserts positioned towards the edge of a phantom having higher calibration factors. Note that the calibration factors for the C&E spleen positioned centrally and anatomically become consistent. This is the case for both energy windows and for VOI and image calibration factors. The introduction of TEW scatter correction in addition to attenuation correction reduces the calibration factors but does not bring them into closer agreement. The simulated AC TEW calibration factors are consistent with experiment for EM2, while those for EM1 are lower by between 8 and 14 percent. The simulated AC TEW calibration factors for EM1 are not significantly more different than the experimental values. When Sim. AC MCSC is used the calibration factors are reduced, but not brought into consistency. Figure 4.11, showing a comparison of the total counts in each projection of experimental scans and simulated scans in vacuum, demonstrates that the sensitivity of the simulated detector is roughly constant as the insert moves across the field of view. In the experimental projections the number of counts per projection varies as the amount of attenuating material between the insert and the detector changes.

Figure 4.12a shows an example of the attenuation maps generated by Xeleris from the CT scans. The CT scans are down-sampled to the same resolution as the reconstructed SPECT images and have voxel values representing the attenuation coefficient of the voxel at the energy of the primary photopeak. The ends of the down-sampled CT image are padded with zeroes to provide 128 slices. The voxel values are in arbitrary units. GE do not provide details of how these images are used in the reconstruction process. A plot of voxel values along a line section is also shown in Figure 4.12b. The water in the phantom has a largely constant voxel value, with only a 2.4 % difference between the centre and the edge. The air bubble at the top of the insert is also visible. The voxel value for water is approximately 162 for the EM1 attenuation map and 132 for EM2. The percentage difference between these values, approximately 20 %, is the same as the percentage difference between the cross sections for photon interactions in water at

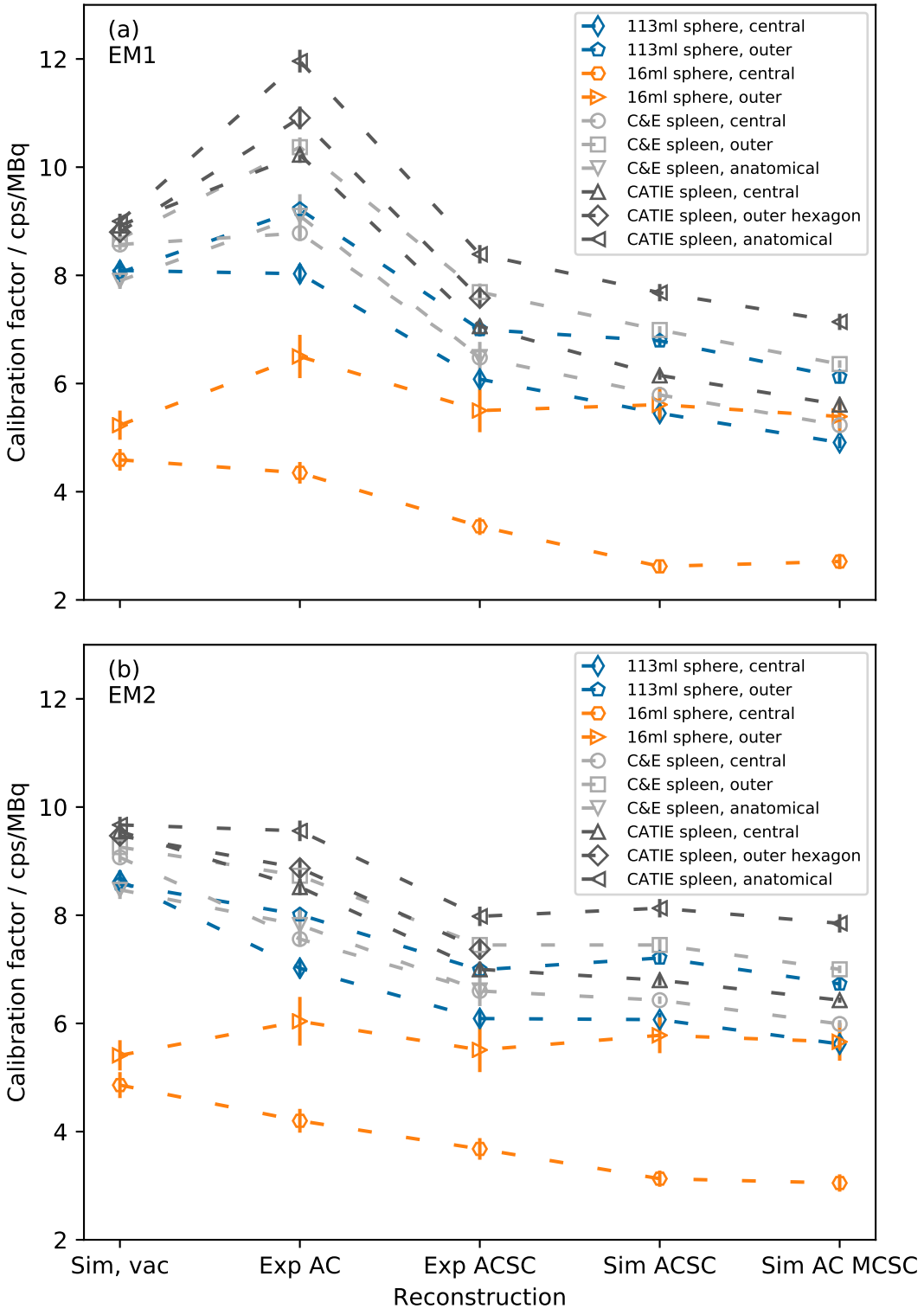

FIGURE 4.9: Calibration factors for the inserts in different positions with different reconstructions methods for (a) the 113 keV photopeak and (b) the 208 keV photopeak. Note the difference of calibration factor when AC is applied which remains when scatter correction is used. The images were reconstructed using GE Volumetrix. The dashed lines are added solely to guide the eye.

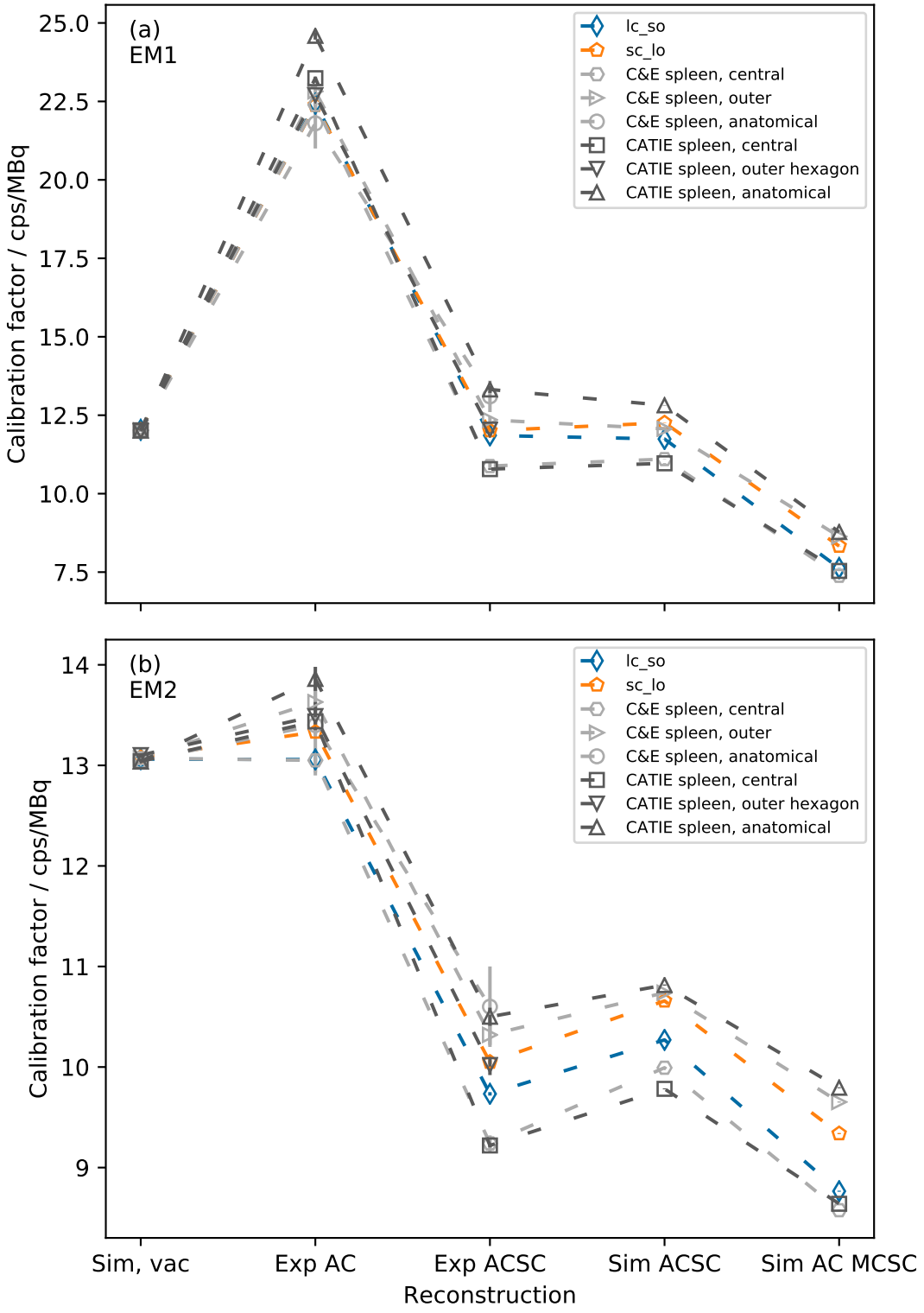

FIGURE 4.10: Calibration factors for the whole reconstructed images for the insert scans. Calibration factors are shown for (a) the 113 keV photopeak and (b) the 208 keV photopeak. Note the difference of calibration factor when AC is applied. The images were reconstructed using GE Volumetrix. The dashed lines are added solely to guide the eye.

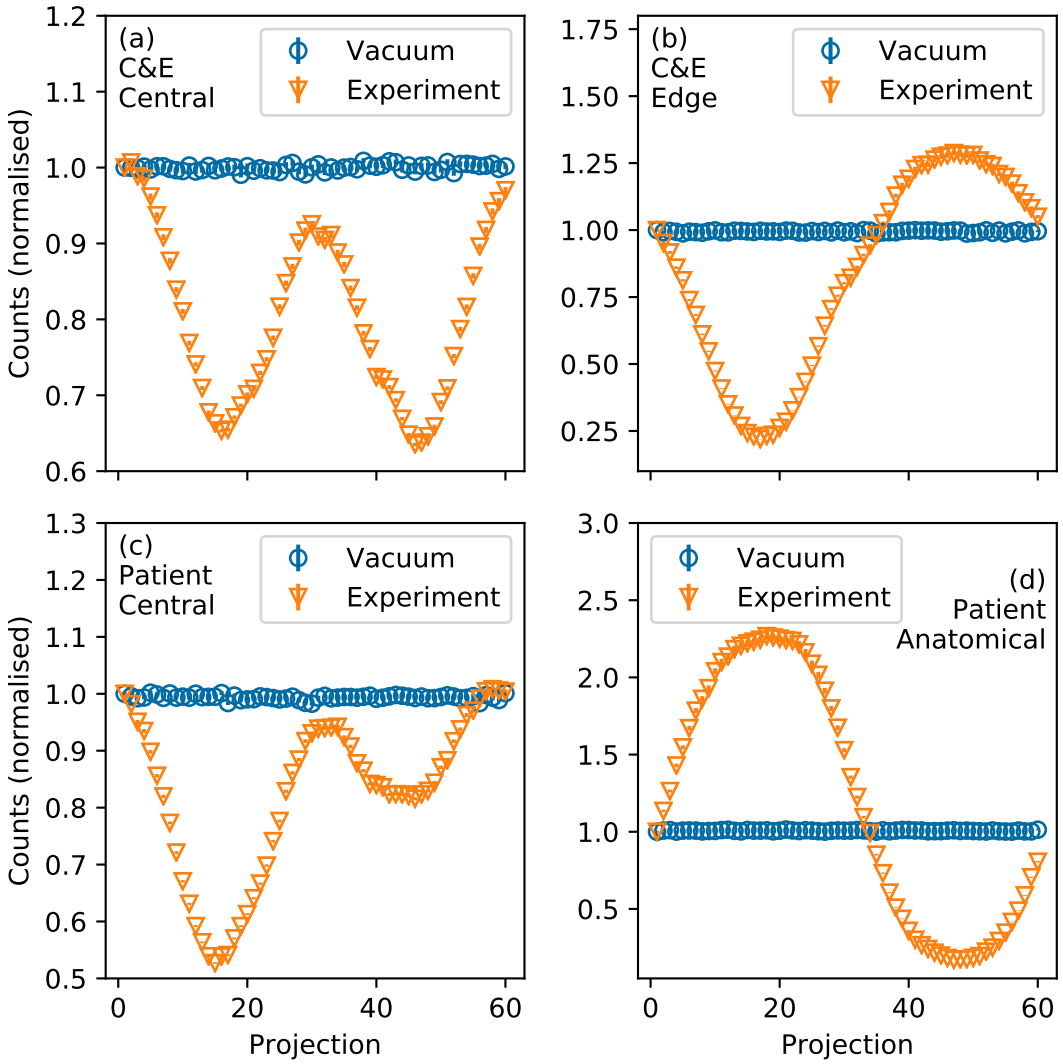

FIGURE 4.11: A comparison of the total number of counts in each projection of the scans of the C&E spleen insert positioned (a) centrally and (b) at the edge of the phantom and CATIE spleen insert positioned (c) centrally and (d) at the edge of the phantom. Counts per projection are shown for simulations in vacuum and the experimental image. The counts are normalised to the number of counts in the first projection. As expected the number of counts per projection is roughly constant for the image in vacuum. This demonstrates that the sensitivity of the detector does not vary with position.

113 keV and 208 keV. This suggests that the conversion from CT number to attenuation coefficient is being done correctly.

Histograms of the counts per voxel and radial distance from the centre of a uniform cylinder for the EM1 and EM2 windows respectively are shown in Figures 4.13 and 4.14. An increase in counts per voxel towards the edge of the cylinder is visible for both experiment and simulation with AC, AC TEW and Sim. AC MCSC.

The SPECT projections of the CATIE spleen in the central and anatomical positions were reconstructed with 5 iterations and 20 subsets with Volumetrix in order to confirm

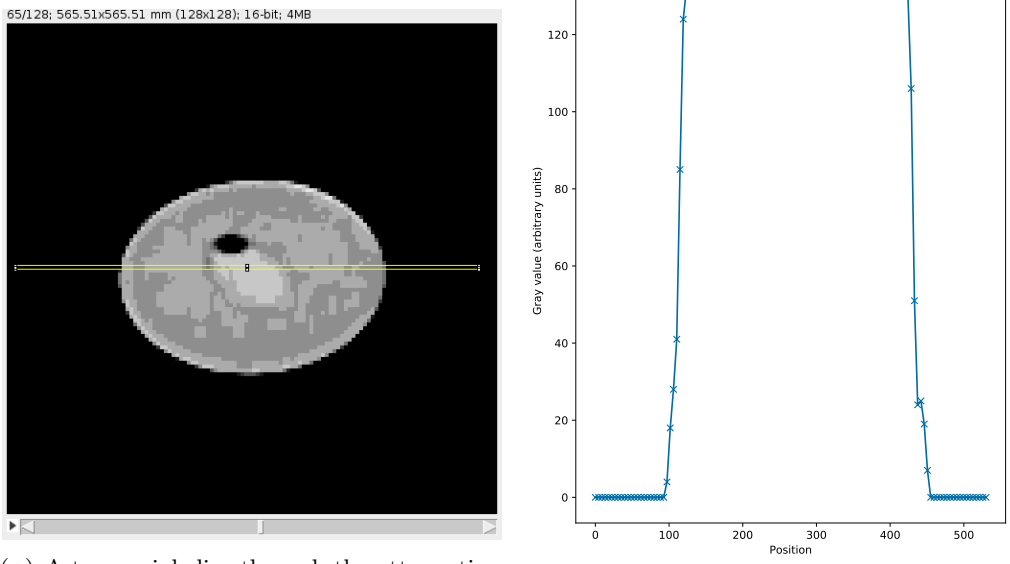

(A) A transaxial slice through the attenuation map.

(B) Profile through the slice.

FIGURE 4.12: Figure showing (a) a transaxial slice through the attenuation map for the EM2 window for the C&E spleen mounted centrally and (b) a line profile through the slice. The pixel values in the attenuation map are in arbitrary units. The pixel values in the water of the phantom are all within 3 units of one another. The pixel values are higher towards the centre but this is only a difference of 2 in 128. The attenuation map for the EM1 window follows the same structure.

that more OSEM updates do not remove the effect. The number of updates is the number of iterations multiplied by the number of subsets. A reconstruction using 5 iterations and 20 subsets may be described as 5x20 updates. Figure 4.15 shows a comparison of the VOI calibration factors for the reconstructed images with 5x20 and 4x10 updates. Increasing the number of updates results in a slight increase in the VOI calibration factors. The amount of noise in the image is increased as shown in Figures 4.16 and 4.17 which compare histograms of the number of counts per voxel in the VOIs. VOI calibration factors for the C&E spleen, CATIE spleen and the spheres in different positions, reconstructed using Hermes HybridRecon, are shown in Figure 4.18. For both energy windows the calibration factors for each insert are consistent when AC is applied. When AC TEW and AC MCSC are applied the calibration factors for each insert remain consistent. Image calibration factors for the SPECT images reconstructed using Hermes HybridRecon are shown in Figure 4.19.

Figure 4.20 shows a comparison of calibration factors for a 113 ml sphere filled with ^{99m}Tc solution positioned centrally and offset in a Jaszczak phantom, reconstructed using GE Volumetrix and Hermes HybridRecon. The calibration factors are inconsistent for the images reconstructed using Volumetrix when both AC and ACSC are used. The calibration factors for Hermes HybridRecon are consistent for both AC and ACSC.

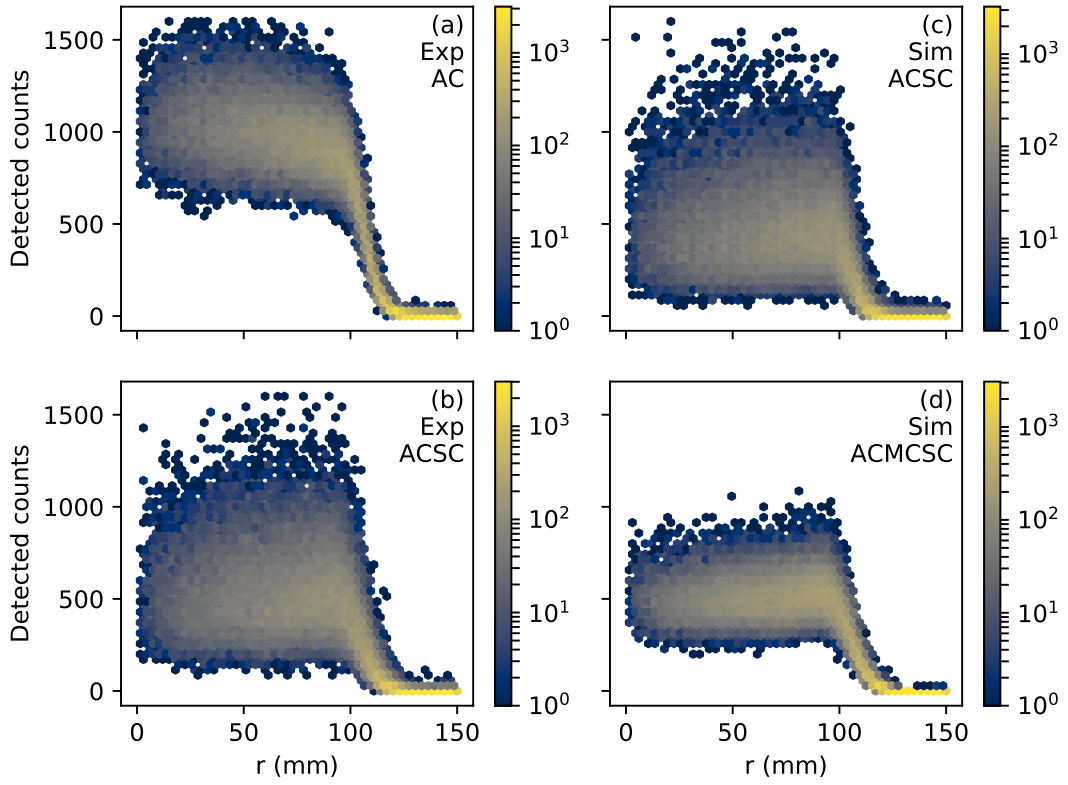

FIGURE 4.13: Figure showing histograms of the number of detected counts in each voxel of a reconstructed SPECT image of a cylindrical Jaszczak phantom against the radial distance from the centre. The colour scale indicates the number of voxels containing a certain number of counts a certain radial distance from the centre of the phantom. The boundary of the phantom is at $r = 108$. Data are shown for the EM1 energy window with (a) AC only, (b) ACSC, (c) simulated with ACSC and (d) simulated with ACMCSC.

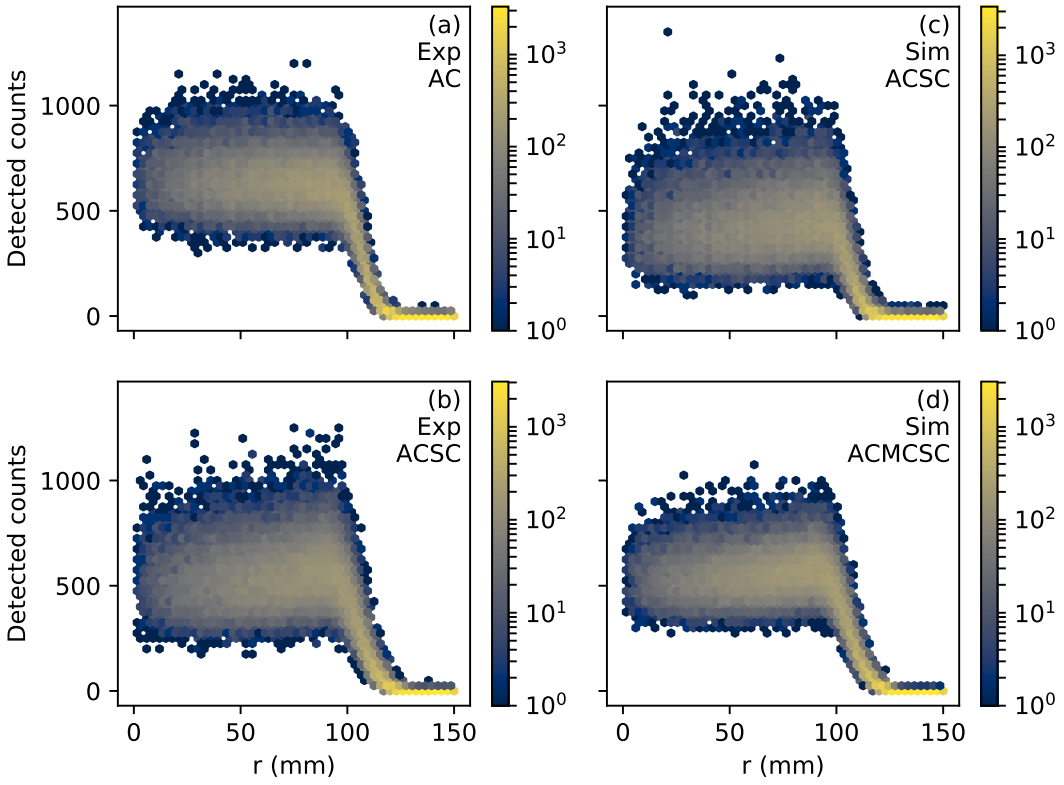

FIGURE 4.14: Figure showing histograms of the number of detected counts in each voxel of a reconstructed SPECT image of a cylindrical Jaszczak phantom against the radial distance from the centre. The colour scale indicates the number of voxels containing a certain number of counts a certain radial distance from the centre of the phantom. The boundary of the phantom is at $r = 108$. Data are shown for the EM2 energy window with (a) AC only, (b) ACSC, (c) simulated with ACSC and (d) simulated with ACMCSC.

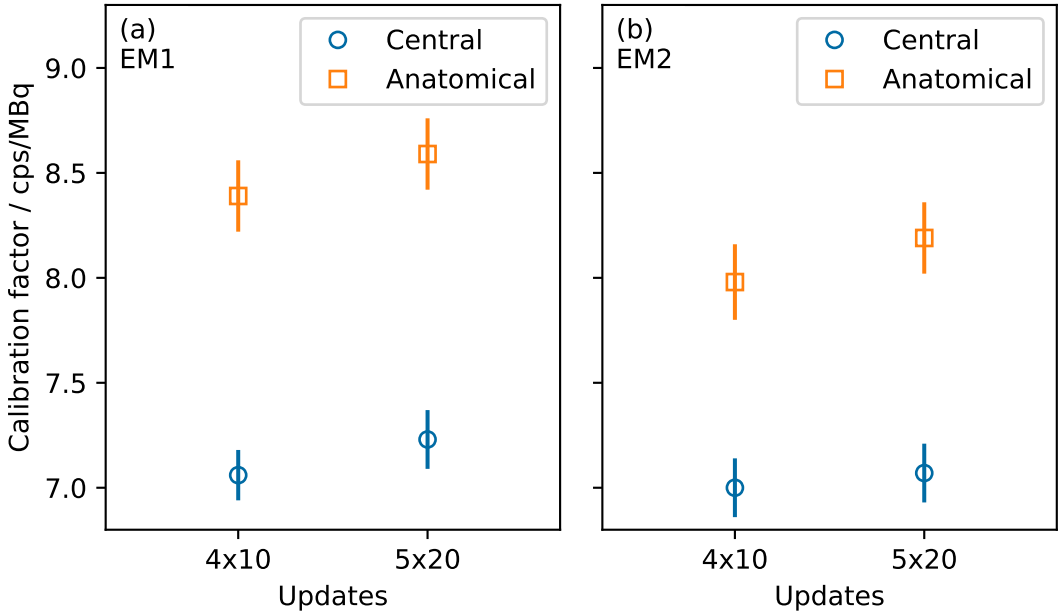

FIGURE 4.15: The calibration factors for the CATIE spleen mounted centrally and anatomically with 4x10 and 5x20 updates. Increasing the number of updates from 4x10 to 5x20 does not result in a significant difference in VOI calibration factor. The calibration factors for the insert in the two positions are not brought into agreement if more updates are used.

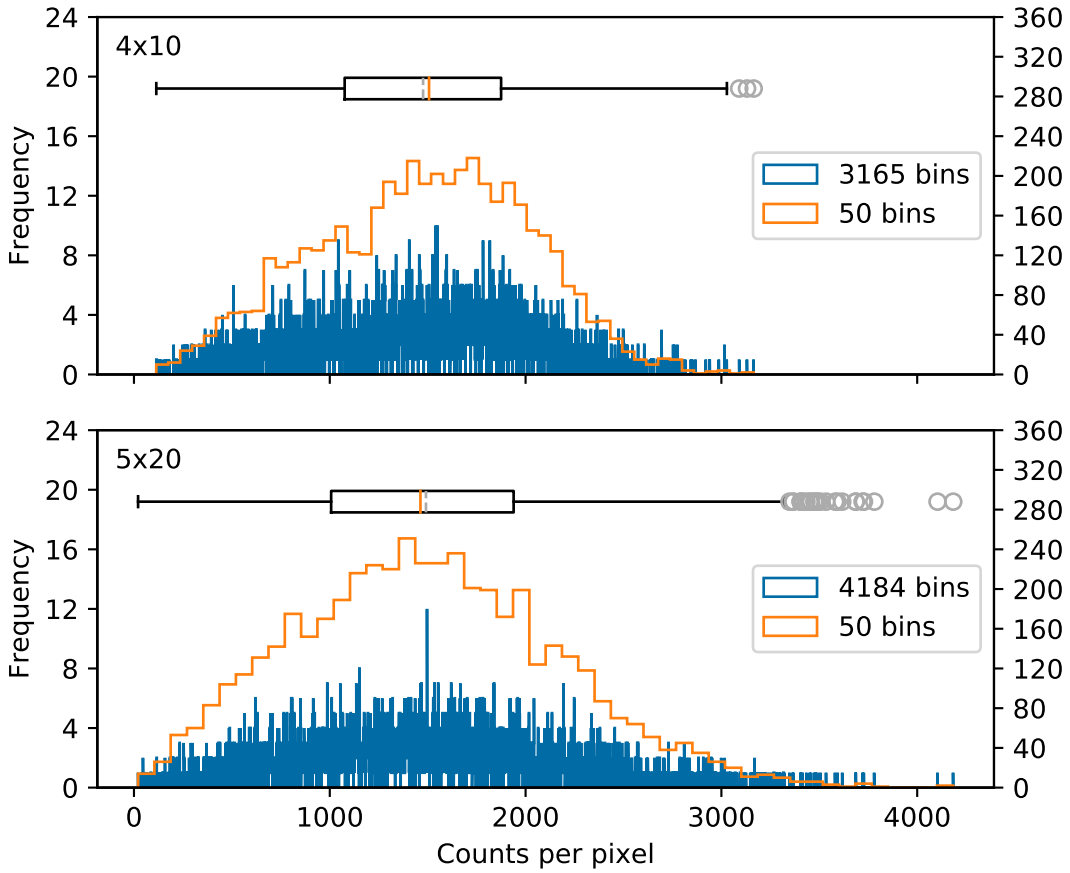

FIGURE 4.16: Figure showing histograms of the counts in each pixel in the VOI for the CATIE spleen mounted centrally, reconstructed with 4x10 and 5x20 OSEM. Also shown are box plots of the same data. The histograms shown in blue have bin widths of one count per pixel, and therefore the number of bins indicates the largest number of counts in any pixel. It can be seen that using 5x20 updates results in a noisier image. This is expected behaviour of the OSEM algorithm.

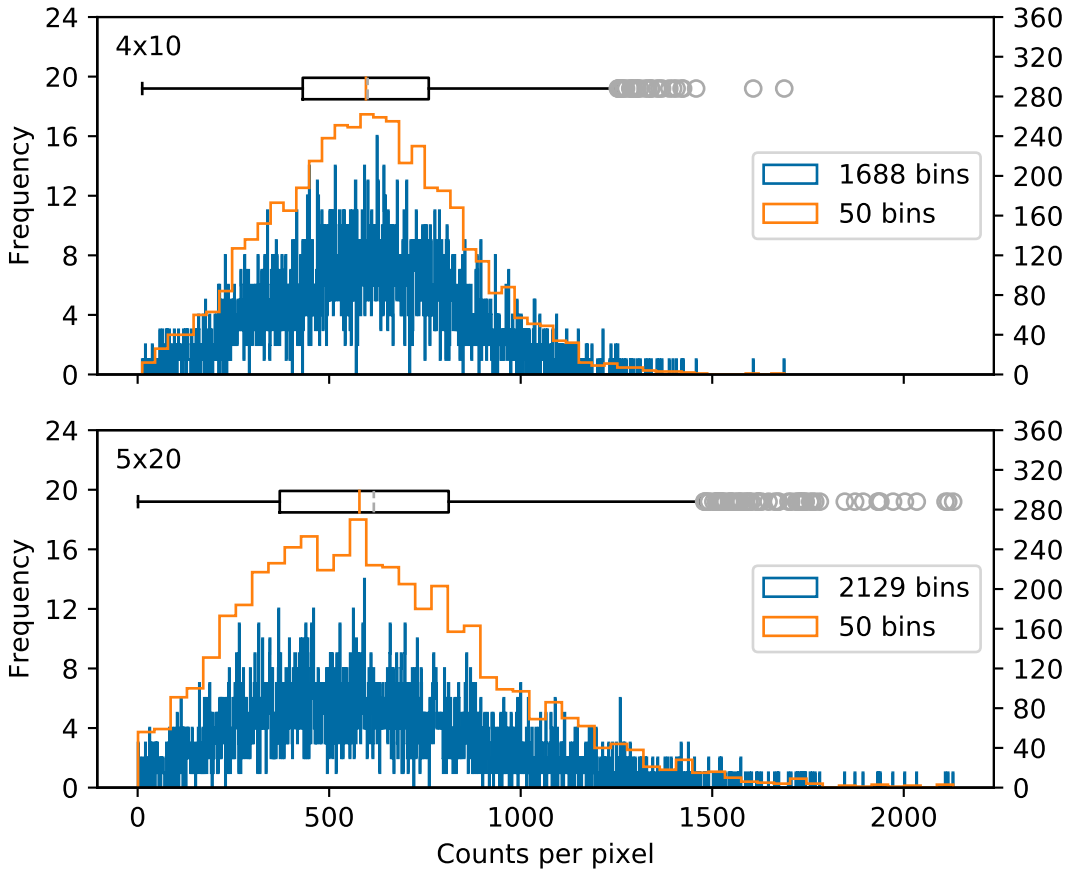

FIGURE 4.17: Figure showing histograms of the counts in each pixel in the VOI for the CATIE spleen mounted in the anatomical position, reconstructed with 4x10 and 5x20 OSEM. Also shown are box plots of the same data. The histograms shown in blue have bin widths of one count per pixel, and therefore the number of bins indicates the largest number of counts in any pixel. It can be seen that using 5x20 updates results in a noisier image. This is expected behaviour of the OSEM algorithm.

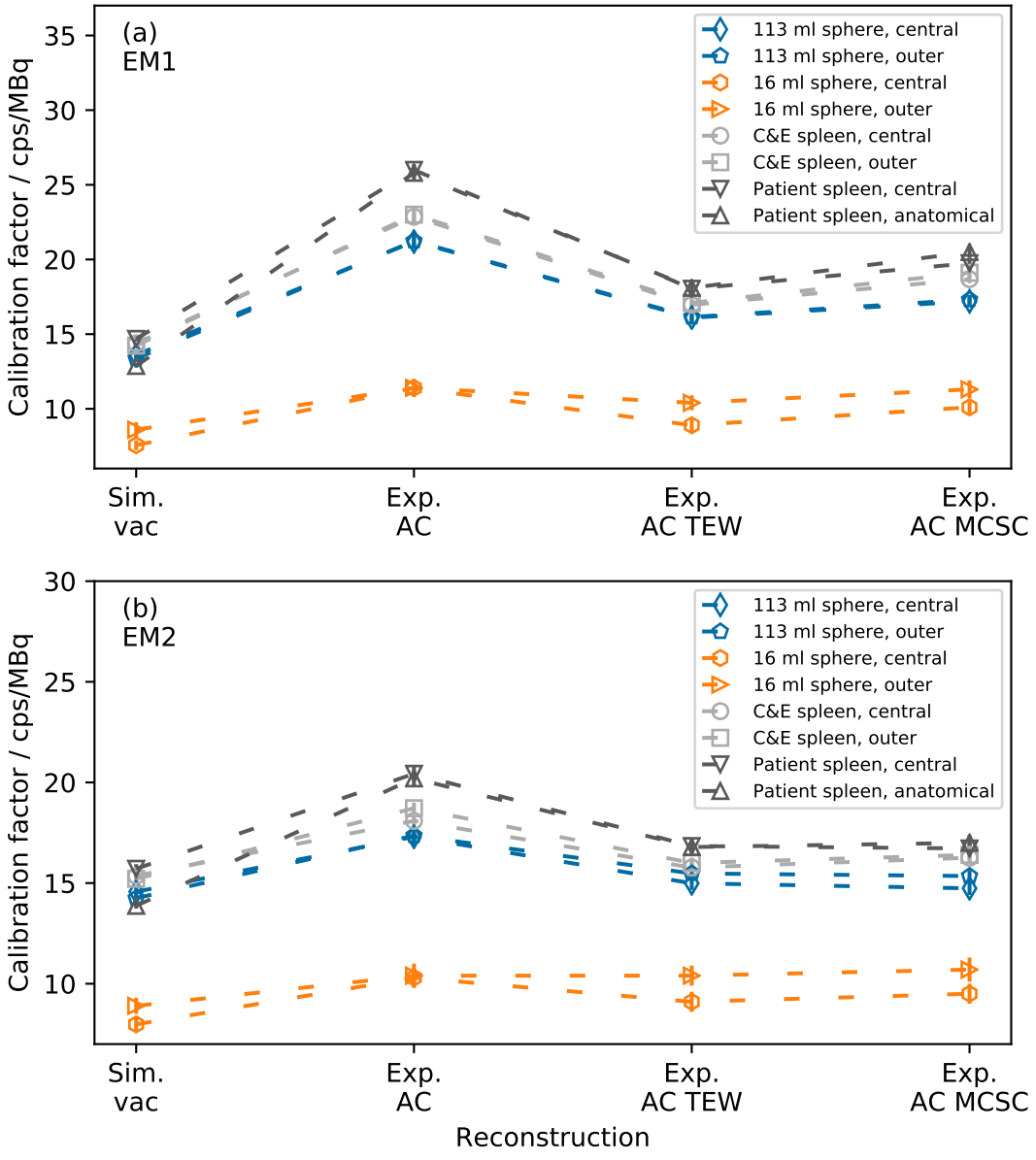

FIGURE 4.18: Comparison of VOI calibration factors for inserts in different positions, reconstructed using Hermes HybridRecon. The calibration factors for the same insert in different positions can be seen to be consistent.

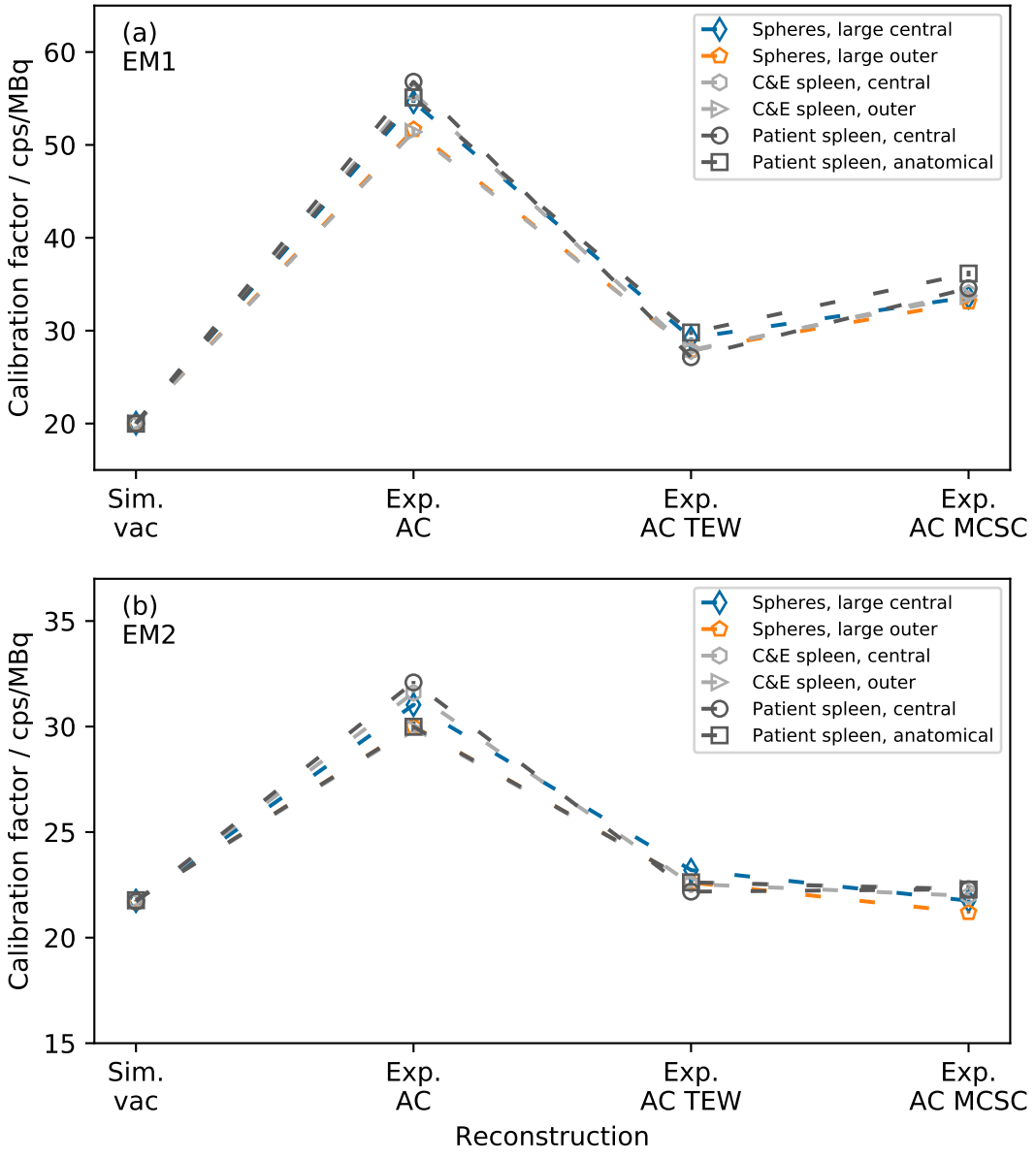

FIGURE 4.19: Comparison of image calibration factors for inserts in different positions, reconstructed using Hermes HybridRecon. The calibration factors for the same insert in different positions can be seen to be consistent.

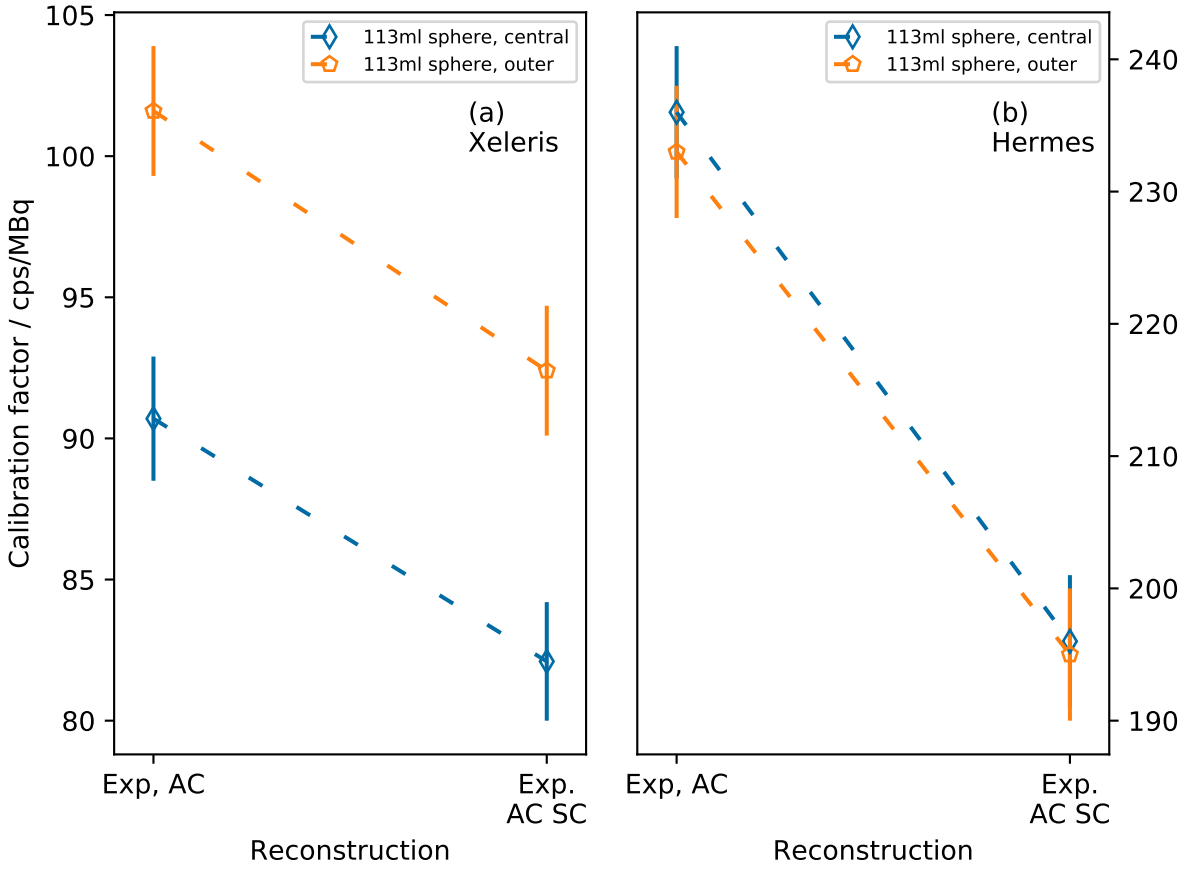

FIGURE 4.20: VOI calibration factors for the 113 ml sphere filled with ^{99m}Tc solution, reconstructed using Volumetrix and HybridRecon. It can be seen that the calibration factors for the image reconstructed using HybridRecon are consistent whilst those from Xeleris are not.

4.6 Discussion

The calibration factors for the simulated data reconstructed with TEW scatter correction are consistent with experiment for the EM2 window. The simulated calibration factors for EM1 are lower by between 8 and 14 percent but those for each insert are not significantly more different than the experimental values. This indicates that there is no positional dependence in the PMT signal processing of the real camera as any such effects are not modelled in the simulation. The image calibration factors for all the inserts in vacuum are consistent with each other, as shown in Figure 4.10. This demonstrates that the inserts are not displaced sufficiently in the field of view for the positional dependence to be due to geometrical effects from the collimator. It is to be expected that all the image calibration factors in vacuum are consistent with each other as the influence of partial volume effects is removed. The comparison of the counts in each projection of the image simulated in vacuum, shown in Figure 4.11, provides further evidence that a geometric effect from the collimator is not responsible for the positional dependence. The number of counts per projection is roughly constant as the SPECT heads rotate around the phantom, and the position of the insert in the field of view changes. The number of counts per projection for the experimental scans are shown to demonstrate the effect of the presence of attenuating and scattering material. In Figure 4.9 the impact of partial volume effects can be seen in the vacuum calibration factors. The calibration factors for each insert are consistent when the insert is translated. When the C&E spleen is rotated however, the calibration factor is different. This is likely due to a difference in partial volume effects when transferring a VOI defined on a CT to the SPECT image. The voxels in the CT image are not cubes as the slice separation is much greater than the voxel height and width (the voxels are 1.1045 by 1.1045 by 4.41806 mm^3). In the scans of the C&E spleen at the centre and edge the long axis is in the plane of the CT image. In the 'anatomical' scan, the long axis is parallel to the long axis of the voxels.

In Figures 4.9 and 4.10 the calibration factors for each insert can be seen to differ significantly when attenuation correction is applied to the experimental data, for both energy windows. It should be noted that the 113 ml and 16 ml spheres were mounted in the same phantom so there are not image calibration factors for these inserts alone. The similarity of the effect whether or not VOIs are used suggests that the origin of the problem is not related to VOI definition. When scatter correction is applied there is a clear change in calibration factor. However the calibration factors for the same insert in different positions are not brought into closer agreement. The same is true when Monte Carlo scatter correction is used. This suggests that the attenuation correction is the cause of the positional dependence. Figure 4.12 shows an attenuation map output from Xeleris after the reconstruction process and a plot of a line section across the attenuation

map image. The attenuation map shows the CT image down-sampled to be the same resolution as the SPECT image while maintaining image registration. The attenuation coefficients measured by the CT scanner are corrected to the energy of the photopeak used for imaging and are given in arbitrary units. As such the attenuation maps can only be discussed qualitatively. The shape of the phantom is maintained in the images and inserts and air bubbles can be seen. The line section indicates that there is a slight increase in the pixel value towards the centre of the phantom. However the pixel values are only approximately 2 % different, much less than the difference observed in calibration factor. The reconstruction system is a 'black box', so it is not possible to assess how the attenuation map is interpreted in the reconstruction process. An increase in counts towards the edge of a uniform cylinder can be seen in Figures 4.13 and 4.14, which show two-dimensional histograms of the counts in each voxel of a uniform cylinder against the radial distance of the voxel from the centre. Again, the effect is visible in images reconstructed with or without scatter correction.

Images of the CATIE spleen and the spheres were additionally reconstructed with 5 iterations and 20 subsets to assess whether the number of OSEM updates had an impact on the positional dependence of calibration factor. While a slight increase in counts is visible when more updates are used the calibration factors for the inserts in the same position are all consistent. The calibration factors for the same insert in different positions are still inconsistent. Figures 4.16 and 4.17 show comparisons of histograms of the number of counts in VOIs of the CATIE spleen in central and anatomical positions with 4x10 and 5x20 updates. Also shown are box plots to indicate the distribution of counts in the histograms. Applying 5x20 updates results in an increase in the distribution of counts and an increase in image noise. This is indicated by the increase of outlier points above the upper quartile and is expected behaviour of the OSEM algorithm.

Images of the C&E spleen, CATIE spleen and the spheres were reconstructed using Hermes HybridRecon. This system uses a different implementation of attenuation correction and the OSEM algorithm which allows an assessment of whether the positional dependence is a fundamental result of the algorithm or due to particular implementations. Figure 4.18 shows the VOI calibration factors for the images reconstructed using the Hermes platform. It can be seen that the calibration factors are consistent for each insert in the experimental images. Moving the same insert inside a phantom has no significant impact on the calibration factor. The VOI calibration factors for the CATIE spleen simulated in vacuum are not consistent. However, the image calibration factors for the CATIE spleen simulated in vacuum, shown in Figure 4.19, are within 0.02 %. The difference between the VOI calibration factors will therefore be due to the image segmentation process. The image calibration factors for the experimental images reconstructed using the Hermes system,

with scatter correction applied, are very close. Moving the inserts inside a phantom has a limited impact on the sensitivity of the reconstructed image.

It was expected that AC would perform better for images of inserts containing ^{99m}Tc as this is the isotope for which the scanners may be considered to be optimised. However, as shown in Figure 4.20 the positional dependence is still present in images reconstructed using GE Volumetrix. The dependence is absent from the images reconstructed using Hermes HybridRecon. This suggests that the problem lies with the conversion of the attenuation coefficients measured during the CT scan to the attenuation coefficients for photons of the required photopeak energy.

The evidence discussed indicates that the cause of the positional dependence is due to differing implementations of attenuation correction in the reconstruction process. As for the differences in calibration factor due to size and shape the difference due to position is not due to random error. Any over- or underestimation of the calibration factor will have a proportional impact on the quantified activity and hence calculated dose. If accurate dosimetry is to be done, the calibration behaviour of the imaging system must be understood and an appropriate calibration factor used.

Chapter 5

Validation of the clinical dosimetry chain

5.1 Overview

For dosimetry to be performed clinically data describing the activity distribution in a patient must be acquired and then used to calculate the dose distribution. In an ideal case multiple SPECT scans would be performed but in practice combinations of SPECT imaging, planar gamma camera imaging and dose rate measurements are also used. Once the activity distribution has been quantified the total number of radioactive decays must be calculated. To determine this a 'time activity curve' (TAC) is fitted to the data and integrated to calculate the area under the curve. This area is also known as the time-integrated activity. The total number of decays is then multiplied by an S-factor as described in Equation (2.18) to calculate the dose.

In Chapter 3 a single time point was imaged and then a mono-exponential with a known half life used to calculate the time-integrated activity. In patients the time-activity curve will be more complex due to the biokinetics of the radiopharmaceutical in the patient. This requires imaging at multiple time points in order to fit a curve. Sums of exponentials are usually used as the fitting function [3]. The fitting of summed exponentials is a challenging problem and is discussed later in this chapter. The images taken at each time point will not necessarily be registered due inconsistent patient position and the distortion of soft tissues in the patient. Registration and segmentation of the images is required to calculate the activity in volumes of interest. Further, some of the time points may only be planar or dose-rate measurements. For reliable fitting more data points than the number of fit parameters must be collected. Commonly fewer than five time points are used in clinical practice. Once the time-activity curve for each organ or VOI has been

fitted the time-integrated activity may be calculated. The dose to organs may then be calculated. Changes in calibration will result in changes to the activities and therefore the doses calculated. This chapter investigates the impact of experimental uncertainties and changing calibration on calculated doses and their uncertainties.

By taking advantage of the knowledge of the TAC for the four organs considered, it is possible to separate the contributions of curve fitting, calibration and S-factors on the calculated dose. If six SPECT scans are performed, six measurements of counts c_i are obtained at times t_i for each VOI. Typically these would be converted to activities $A_i = kc_i$ where $k = (\text{scan duration} \cdot \text{cf})^{-1}$. This equation is a rearrangement on Equation (2.9). A function $A(t)$ is then fitted to these activity values and integrated for use in Equation (2.18). As k is a constant, $A(t) = kc(t)$ and $\widetilde{A}$ from Equation (2.18) can be written as

$$\widetilde{A} = k \int_0^{T_D} c(t)dt = k \cdot \widetilde{c}. \tag{5.1}$$

Substituting Equation (5.1) into Equation (2.18), and considering only one source region, gives

$$D(r_T, T_D) = S(r_T \leftarrow r_S)k\widetilde{c}(r_S, T_D). \tag{5.2}$$

The calibration factor is a constant scaling factor and does not change the shape of curve fitted to the c_i. It can also be seen that a percentage change in any of S, k or $\widetilde{c}$ will have an equal percentage change on the calculated dose. The percentage uncertainty on the dose will be at least as large as the largest percentage uncertainty on S, k and $\widetilde{c}$. The impact of changing calibration factor on activity recovery has been shown in Chapter 3. This chapter will discuss the impact of patient-specific S-factors for different isotopes and examine the impact of curve fitting on the calculated value of the integrated counts, $\widetilde{c}$. Patient-specific Monte Carlo simulation is used to calculate patient-specific S-factors. In order to examine the impact of curve fitting many sets of activities were generated based on known TACs. The generation of the data sets and the fitting process are discussed in Section 5.2.2.

5.2 Impact of TAC fitting

The fitting of sums of exponential functions is a classically hard problem in the field of curve fitting using non-linear least squares methods [67–69]. This section examines the impact of this difficulty on the calculation of radiation dose in MRT. This is done as a mathematical exercise to assess the problems which occur if non-linear least squares methods are used despite the difficulties involved. Large synthetic data sets were generated, representing experimental measurements, distributed according to known biexponential

functions. The area under the curves was calculated using two methods. The first method was refitting the biexponential function defining the distribution of the data points to the data points. The second method was to fit multiple functions to the data points, and take the weighted mean of the area under those fits which passed quality control criteria. The methods are discussed in detail in Section 5.2.2. Calculating the area for large numbers of sets of data points allows the estimation of the PDF of the area under the curve given the distribution of data points. These results allow the validity of the assumption that the calculated areas under the curve follow a Gaussian distribution to be assessed. Similarly, PDFs of the fit parameters were estimated for refitted biexponential functions. The distributions of the fit parameters for a refitted biexponential function show that the parameters estimated by the fitting process are not reliable estimates of the true function parameters. This is to be expected given the problems inherent in fitting sums of exponential functions.

5.2.1 Difficulties with TAC fitting

The central problem with the fitting of summed exponential functions is that there is not guaranteed to be a unique set of fit parameters which give a 'best fit' [70, 71]. An example of this so-called 'ill conditioning' is shown in Figure 5.1. This potential lack of uniqueness arises from the structure of the optimisation function and cannot generally be rectified by acquiring more data points. As a result, the parameters of the best fit line may be far from those of the true function despite producing very similar curves. Further, the values of the fit parameters are sensitive to the values of the measured data points and if the decay rates differ by less than a factor of five then it is likely that one of the parameters is redundant [72]. The calculation of uncertainties and covariances of the fit parameters is complicated by the fact that the confidence intervals of the fit parameters are likely to be asymmetric and confidence regions for pairs of parameters may be curved rather than elliptical [68]. This asymmetry means that the covariance matrix estimated by a least-squares fitting algorithm is not a good estimate of the standard error on the parameters. Similarly, the lack of symmetry means that the PDFs of the fit parameters are not Gaussian and writing the parameters like $p = x \pm \sigma$ is not appropriate and standard error propagation cannot be used. Confidence intervals may be evaluated by using other methods to explore possible values of the parameters but if the PDF has multiple peaks a single confidence interval is not a reliable way of describing the distribution. Monte Carlo techniques allow the estimation of the PDF of the fitted parameters and the area under the curve by performing fits repeatedly using different sets of simulated measurements distributed around a true curve.

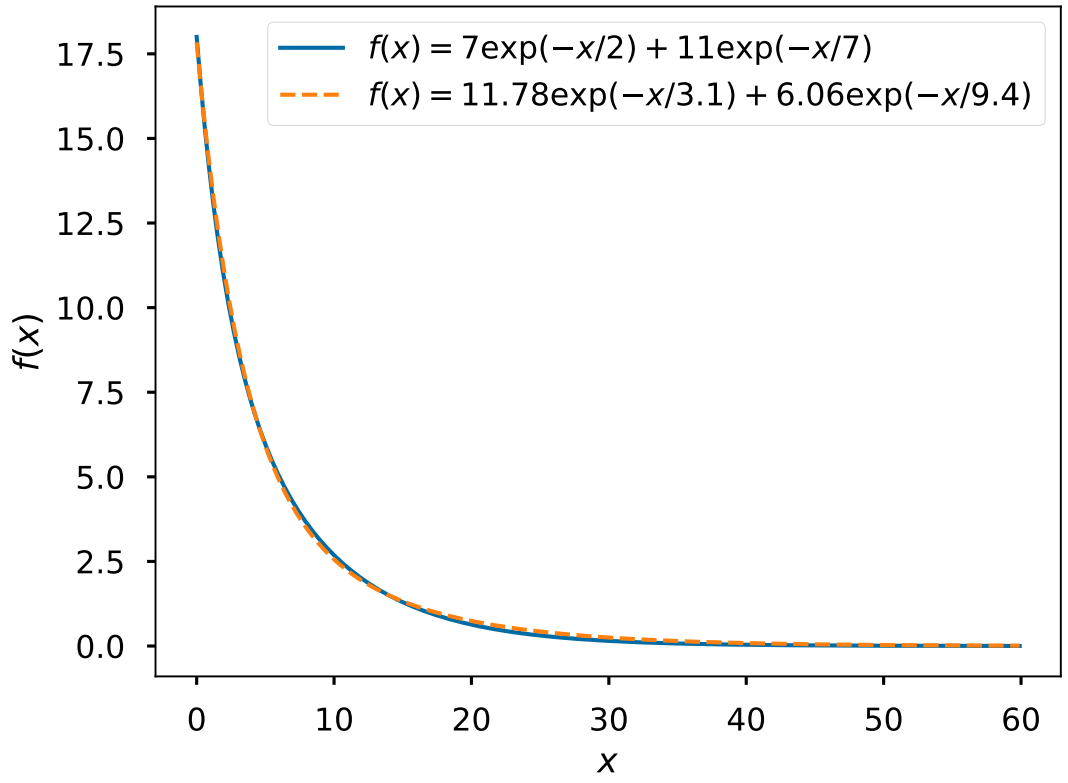

FIGURE 5.1: An example of the lack of identifiability of summed exponentials. The two curves have different parameters but are nearly indistinguishable. The area under the solid blue curve is 90 and the area under the dashed orange curve is 100.5268, both in arbitrary units. This figure is adapted from reference [68].

In clinical practice the correct functional form, and the parameters of the function, are not known. The choice of function may be informed by pharmacokinetic modelling and examination of the available data. The NUKFIT software aims to estimate the area under a real curve by fitting multiple functions and selecting those which are suitable based on quality control criteria [73]. The criteria are shown in Table 5.1. The corrected Akaike Information Criterion (AICc) is used to indicate which of several functions is the best match to the data [74]. The Akaike Information Criterion (AIC) estimates the Kullback-Liebler Information, which is a measure of the information lost when one model is used to approximate another [75]. If the ratio of number of data points, n, to the number of model parameters, k, is small then the corrected AIC (AICc) is recommended [75]. A small ratio is suggested in reference [75] to be 40, so in nuclear medicine the AICc is more appropriate. The absolute value of the AIC is not meaningful on its own; it should only be used in comparison to other values. The function with the lowest AIC is the one most supported by the data. It should be noted that the function may not be a good

match; it is the best out of those compared. The Akaike weights,

$$w_{\mathrm{AIC}_i} = \frac{\exp\left(\frac{-\Delta_i}{2}\right)}{\sum_{i=1}^{F} \exp\left(\frac{-\Delta_i}{2}\right)} \tag{5.3}$$

where $\Delta_i = \mathrm{AICc}_i - \mathrm{AICc}_{\min}$, $\mathrm{AICc}_{\min}$ is the minimum AICc and F is the number of functions used, are then calculated for functions which meet the quality control criteria. The area under each curve is calculated and the standard error estimated using Gaussian error propagation. The final area under the curve is calculated as

$$\mathrm{AUC} = \sum_{i=1}^{F} w_{\mathrm{AIC}_i} \cdot \mathrm{AUC}_i, \tag{5.4}$$

where AUC_i is the area under the ith curve. The standard error on the area under the curve is given by

$$\mathrm{SE(AUC)} = \sum_{i=1}^{F} w_{\mathrm{AIC}_i} \cdot \sqrt{\mathrm{SE}(\mathrm{AUC}_i)^2 + (\mathrm{AUC}_i - \mathrm{AUC})^2}. \tag{5.5}$$

The closeness of the area under the curve calculated using this technique to the true area can also be assessed using Monte Carlo techniques.

TABLE 5.1: The quality control criteria used in NUKFIT. J is the number of adjustable parameters and N is the number of data points. This table is reproduced from reference [73].

Results	Condition	Quality control
Plot	...	Visible inspection
R^2	...	Close to 1
AIC	...	Compare with values of other functions
AICc	$J + 2 \leq N$	Compare with values of other functions
w_{AICc}	All functions $J + 2 \leq N$	If $w_{\mathrm{AICc}} > 0.01$ function is used for inference
Parameter	$J \leq N$	Plausible values
Parameter SE	$J + 1 \leq N$	CV $< 25\%$ precise, CV $< 50\%$ acceptable
Correlation matrix	$J + 1 \leq N$	$-0.8 <$ each element < 0.8
Weighted residuals	...	Random distribution

5.2.2 Monte Carlo TAC fitting

Time activity curves for each insert were calculated based on the clinical TACs for the patient from which the CATIE phantom was derived. All the curves used were biexponentials, with two excretion phases for the liver and kidneys and an uptake and

clearance phase for the spleen. The liver and kidney curves are of the form

$$A(t) = A_i f \exp(\frac{-t\ln(2)}{t_1}) + A_i(1-f)\exp(\frac{-t\ln(2)}{t_2}). \tag{5.6}$$

The functional form used for the spleen,

$$A(t) = A_1 \exp(\frac{-t\ln(2)}{t_1}) + A_2 \exp(\frac{-t\ln(2)}{t_2}), \tag{5.7}$$

is more convenient when uptake is modelled. The TACs are shown in Figure 5.2 with the parameters of each given in Tables 5.2 and 5.3. Re-fitting Equation (5.7) to generated data is examined in Section 5.2.5 and is not reliable. This problem arises in part due to only the first time point being on the uptake portion of the curve, so fitting the uptake is unreliable. This can be easily seen by plotting the time points on the TAC, as shown in Figure 5.3. For any single set of data points there is not enough information to determine that the fitted function should pass through the origin. The fit can be constrained further by writing the function in the form

$$A(t) = A_i \left(\exp(\frac{-t\ln(2)}{t_1}) + \exp(\frac{-t\ln(2)}{t_2}) \right). \tag{5.8}$$

Writing the equation in this way forces the fit to pass through zero.

TABLE 5.2: Parameters of the TACs for the inserts apart from the spleen.

Insert	A_i	f	t_1	t_2
Liver	496.8	0.21	15.7	70.8
Kidneys	190.4	0.65	73.8	2.49

TABLE 5.3: Parameters of the TAC for the spleen, defined as Equation (5.7).

A_1	A_2	t_1	t_2
411.8	−411.8	70.4	0.34

TABLE 5.4: Parameters of the TAC for the spleen, defined as Equation (5.8).

A_1	t_1	t_2
411.8	70.4	0.34

Data sets were generated based on these curves. Each data set contained six time points, at $t = 1, 4, 24, 40, 72, 144$ hours after injection. The time points are derived from a combination of the time points used at the Christie Hospital and ASMN [14]. The sets of data points were calculated by randomly sampling a Gaussian distribution centred on

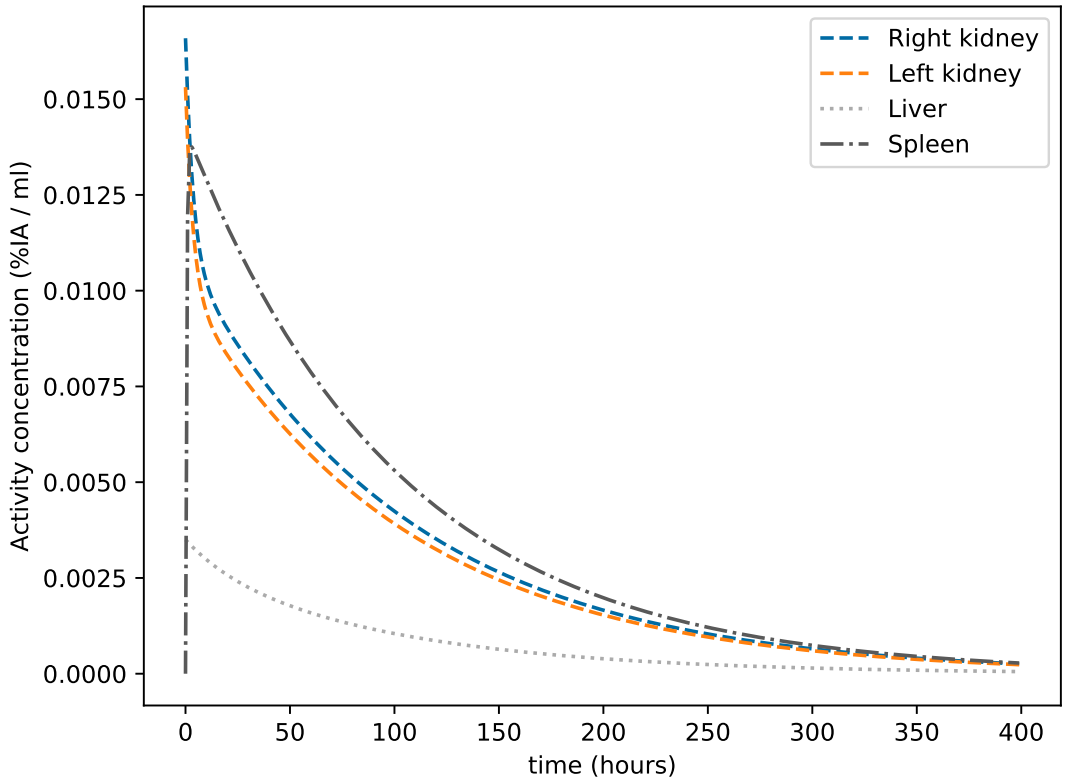

FIGURE 5.2: The time activity curves used to examine the impact of curve fitting on dose. The curves are given in units of activity concentration, scaled to the total injected activity.

the true curve at each time point with a width representing the expected distribution of a measurement around the true value. Two sets of widths were used, 5 % of the activity for all times, referred to as 'constant width' and a linear percentage uncertainty from 5 % at $t = 1$ hour to 15 % at $t = 144$ hour, referred to as 'linearly scaled width'. The width of 5 % was chosen to represent a best case, which is unlikely to be attainable in practice. The choice of the scaling with time is arbitrary and informed by experimental imaging to represent the distribution which may be more likely in practice. Sets of points generated in this manner were used to assess the accuracy under fitted curves using the same function as was used to generate the fit and using the NUKFIT strategy. The fitting using a single function was done using the `curve_fit` function from the `scipy` python library [76]. The starting parameters for the fits and constraints on the fit parameters are shown in Table 5.5. The constraints for the half-lives were chosen such that the half-lives are positive and less than the physical half-life of ^{177}Lu. The initial values of the half-lives were chosen to be close to the true values. For convenience of labelling, the initial values were opposite ways around for the liver and kidney curves. The initial value of f was set to assume equal weights of each exponential function, and as a fraction was constrained to be between 0 and 1. The value of A_i was set to be the true value

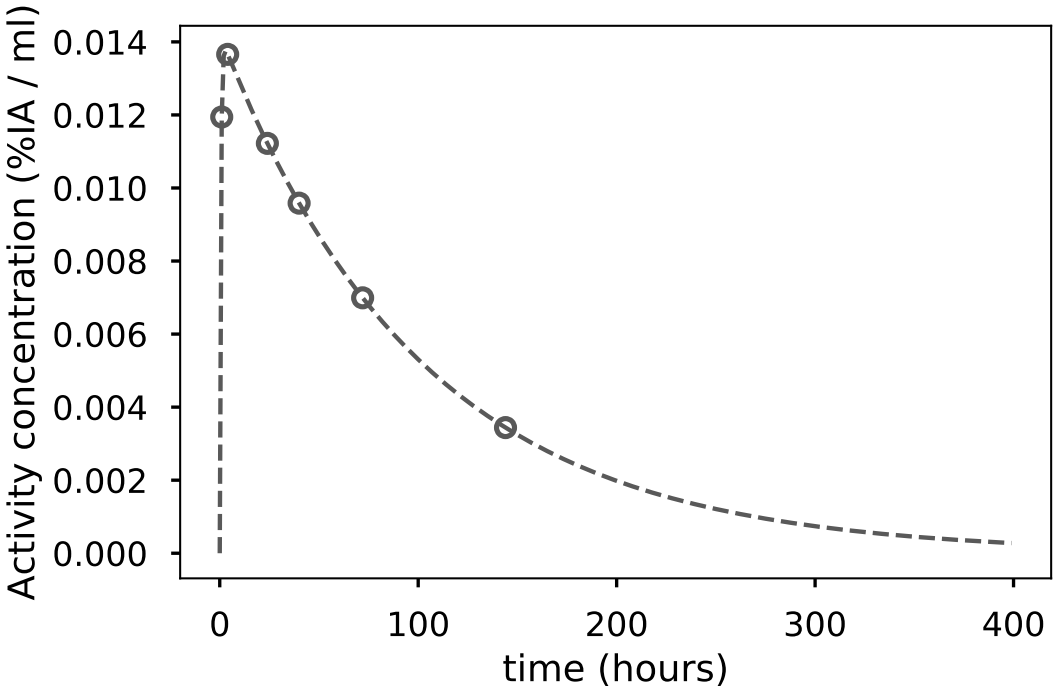

FIGURE 5.3: The spleen time activity curve, with points showing the activities at the imaging times. The curve are given in units of activity concentration, scaled to the total injected activity.

rounded to one significant figure. This is similar to the value which may be set by visual inspection of the data points before fitting. A_i was constrained to be positive and less than an unrealistically large value. The value of A_i is well controlled by the values of the points. The fitting using the NUKFIT-style method was done using the `lmfit` python package [77]. Ten million sets of points were used to assess the refitting of the true function. Due to the increased computation time of fitting six functions per data set only one million sets of points were used for NUKFIT strategy.

TABLE 5.5: The starting values and constraints on the fit parameters for the fits done using a single function.

Function	Starting parameters	Constraints
Equation (5.6)	A_i, true value to 1 s.f.	$0 \leq A_i \leq 10\,\text{GBq}$
	$f = 0.5$	$0 \leq f \leq 1$
	$t_1 = 10,100\,\text{hours}$	$0 \leq t_1 \leq 159.54\,\text{h}$
	$t_2 = 100,10\,\text{hours}$	$0 \leq t_2 \leq 159.54\,\text{h}$
Equation (5.7)	$A_{1,2}$, true value to 1 s.f.	$-1 \leq A_{1,2} \leq 1\,\text{GBq}$
	$t_1 = 10\,\text{hours}$	$0 \leq t_1 \leq 159.54\,\text{h}$
	$t_2 = 100\,\text{hours}$	$0 \leq t_2 \leq 159.54\,\text{h}$
Equation (5.8)	A_i, true value to 1 s.f.	$0 \leq A_i \leq 10\,\text{GBq}$
	$t_1 = 10\,\text{hours}$	$0 \leq t_1 \leq 159.54\,\text{h}$
	$t_2 = 100\,\text{hours}$	$0 \leq t_2 \leq 159.54\,\text{h}$

`lmfit` allows the confidence intervals for fit parameters to be estimated directly. This is done as follows: the F-test is used to compare the best fit model to an alternate model. The alternate model is the same as the best fit, but with one of the parameters fixed. This parameter is varied until the difference in the chi-squared values for the two models cannot be explained by the loss of a degree of freedom within a certain confidence. The starting values of and the constraints on the fit parameters for the `nukfit`-style fits are shown in Table 5.6. The half lives for all the functions were constrained to be positive and less than the physical half life of ^{177}Lu. The value of f in function f_{4b} is constrained to be between 0 and 1 as before. The activity values were, as before, constrained to be between 0 and 10 GBq apart from for function f_{4a} which was not constrained. The initial values of all activities were 500 MBq and the initial values of effective half lives were 50 hours.

TABLE 5.6: The starting values and constraints on the fit parameters for the fits done using `lmfit` emulating the `nukfit` strategy.

Function	Starting values	Constraints
f_1	$A_1 = 500\,\text{MBq}$	$0 \leq A_1 \leq 10\,\text{GBq}$
f_2	$A_1 = 500\,\text{MBq}$	$0 \leq A_1 \leq 10\,\text{GBq}$
	$t_{\text{eff}} = 50\,\text{hours}$	$0 \leq t_{\text{eff}} \leq 159.54\,\text{h}$
f_3	$A_1 = 500\,\text{MBq}$	$0 \leq A_1 \leq 10\,\text{GBq}$
	$A_2 = 500\,\text{MBq}$	$0 \leq A_2 \leq 10\,\text{GBq}$
	$t_{\text{eff}} = 50\,\text{hours}$	$0 \leq t_{\text{eff}} \leq 159.54\,\text{h}$
f_4	$A_1 = 500\,\text{MBq}$	$0 \leq A_1 \leq 10\,\text{GBq}$
	$A_2 = 500\,\text{MBq}$	$0 \leq A_2 \leq 10\,\text{GBq}$
	$t_{\text{eff},1} = 50\,\text{hours}$	$0 \leq t_{\text{eff},1} \leq 159.54\,\text{h}$
	$t_{\text{eff},2} = 50\,\text{hours}$	$0 \leq t_{\text{eff},2} \leq 159.54\,\text{h}$
f_{4a}	$A_1 = 500\,\text{MBq}$	
	$t_{\text{eff},1} = 50\,\text{hours}$	$0 \leq t_{\text{eff},1} \leq 159.54\,\text{h}$
	$t_{\text{eff},2} = 50\,\text{hours}$	$0 \leq t_{\text{eff},2} \leq 159.54\,\text{h}$
f_{4b}	$A_1 = 500\,\text{MBq}$	$0 \leq A_1 \leq 10\,\text{GBq}$
	$f = 0.5$	$0 \leq f \leq 1$
	$t_{\text{eff},1} = 50\,\text{hours}$	$0 \leq t_{\text{eff},1} \leq 159.54\,\text{h}$
	$t_{\text{eff},2} = 50\,\text{hours}$	$0 \leq t_{\text{eff},2} \leq 159.54\,\text{h}$

For the refitting of the true functions histograms of the fit parameters and the ratio of the fitted area to the true area were produced. It should be noted that the numerical results stated are specific to these curves and may not necessarily apply to other data. Histograms of the distributions of the fit parameters and areas are estimations of the PDFs of the fit parameters and areas.

The functions used from NUKFIT were:

$$f_1(t) = A_1 \exp\left(\frac{-t\ln(2)}{t_{\text{phys}}}\right), \tag{5.9}$$

$$f_2(t) = A_1 \exp\left(\frac{-t\ln(2)}{t_{\text{eff}}}\right), \tag{5.10}$$

$$f_3(t) = A_1 \exp\left(\frac{-t\ln(2)}{t_{\text{eff}}}\right) + A_2 \exp\left(\frac{-t\ln(2)}{t_{\text{phys}}}\right), \tag{5.11}$$

$$f_4(t) = A_1 \exp\left(\frac{-t\ln(2)}{t_{\text{eff},1}}\right) + A_2 \exp\left(\frac{-t\ln(2)}{t_{\text{eff},2}}\right), \tag{5.12}$$

$$f_{4\text{a}}(t) = A_1 \left(\exp\left(\frac{-t\ln(2)}{t_{\text{eff},1}}\right) - \exp\left(\frac{-t\ln(2)}{t_{\text{eff},2}}\right)\right), \tag{5.13}$$

$$f_{4\text{b}}(t) = A_i f \exp\left(\frac{-t\ln(2)}{t_{\text{eff},1}}\right) + A_i(1-f) \exp\left(\frac{-t\ln(2)}{t_{\text{eff},2}}\right). \tag{5.14}$$

In Equations (5.9) to (5.14) t_{phys} is the physical half life of the isotope and t_{eff} is an effective half life which combines the physical half life and the biological half life of the organ being considered. It should be noted that Equation (5.13) is equivalent to Equation (5.8) and Equation (5.14) is equivalent to Equation (5.6).

Each curve was fitted in turn, using the method recommended by `lmfit` for fitting biexponential functions using non-linear least squares methods. This recommended method uses the Nelder-Mead minimisation algorithm to generate starting parameters for a fit using the Levenberg-Marquardt algorithm. Curves were selected as 'good' using criteria based on those used in NUKFIT. The criteria were that every correlation coefficient was in the range $(-0.8, 0.8)$ and the fractional standard error on each parameter was calculated and less than 0.5. This makes the assumption that the uncertainties estimated using the fitting function are good estimates of the actual confidence interval. Visual inspection, used in NUKFIT, is not possible for the amount of fits being examined. No metric of how close to one the value of R^2 should be was provided, but for all fits to one hundred thousand sets of data points for all functions R^2 was greater than 0.99. For each set of 'good' functions the AICcs and areas under the curves were calculated. The estimated area under the curve was then calculated as in NUKFIT.

The PDF of the area under the curve was generated as for the fitting of a single function. For all the fits done with the NUKFIT strategy used an initial value 500 for activities, 50 for times and 0.5 for f in Equation (5.14). Under the assumption that the restriction on the correlation between the parameters ensures symmetric confidence intervals the uncertainty on the final area under the curve was also calculated. Plotting histograms of the fit parameters shows that this may not necessarily be the case. The frequency of each function being suitable was examined.

The results for each organ are presented separately. For each organ the results for the fits using solely a biexponential function are presented, followed by the NUKFIT-style strategy.

5.2.3 Liver

5.2.3.1 Constant width, single function

Of the ten million fits of a biexponential function to points distributed according to the liver curve with a constant width, 1.4 % of the fits using a 5 % width failed to converge. A histogram of the ratio of the area under the fitted curve to the area under the true curve is shown in Figure 5.4. There is a significant peak at 1.2 in the ratio of fitted area to true area, which will be due to an increased likelihood of convergence to an incorrect curve. Histograms of the fit parameters are shown in Figure 5.5. It can be seen that for the majority of fits t_2 is set to be the largest value allowed by the fit boundaries. It is reasonable for f to be bimodal as the exponentials in Equation (5.6) can be written either way around. This would also lead to an expectation for the fitted values of t_1 and t_2 to be bimodal. The distribution of t_2 is bimodal, but with the main peak at the limit of the fitting boundary rather than the expected value of t_1. The t_1 values are spread out with four values preferred. These may be artefacts relating to the low number of data points used. Correlations between pairs of fit parameters are shown in Figure 5.6. It should be noted that all the parameters are correlated, so the histograms are all related. It is expected that the most values will be clustered around the true values of the fit parameters. This is not the case, and for the A_i vs. f, A_i vs. t_1 and f vs. t_1 have clusters of points which are not aligned with at least one of the true values. In the histograms involving t_2, most of the values are at the maximal value of t_2.

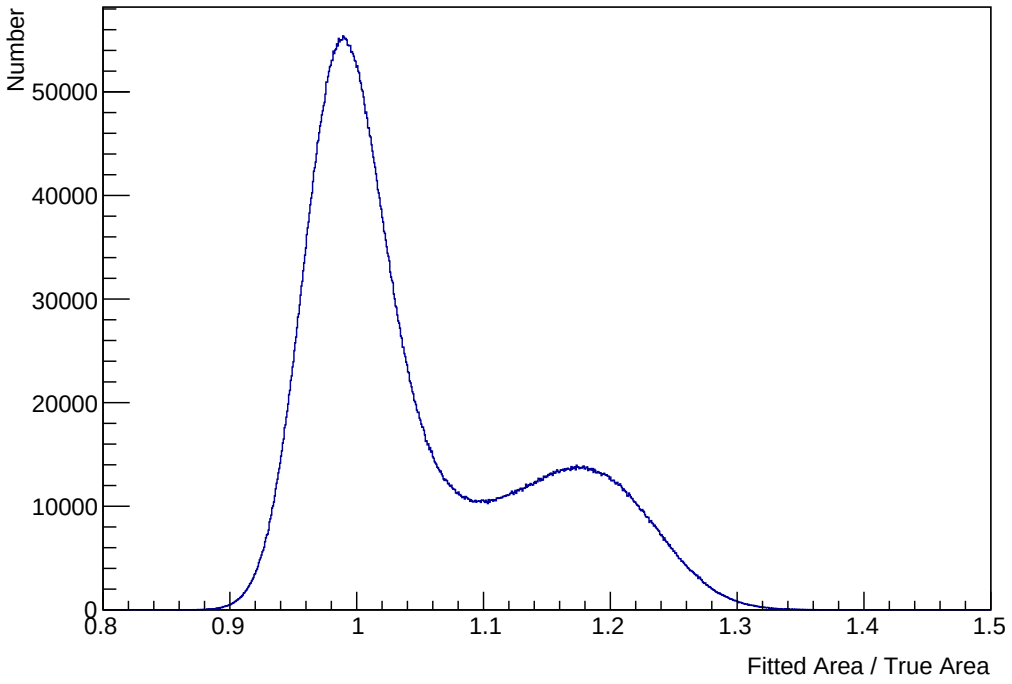

FIGURE 5.4: A histogram of the ratio of the area under the fitted curve and the area under the true curve for the liver with a constant perturbation width. The main peak of the histogram is around 1, but there is a secondary peak around 1.2. This likely indicates a local minimum of the optimisation function.

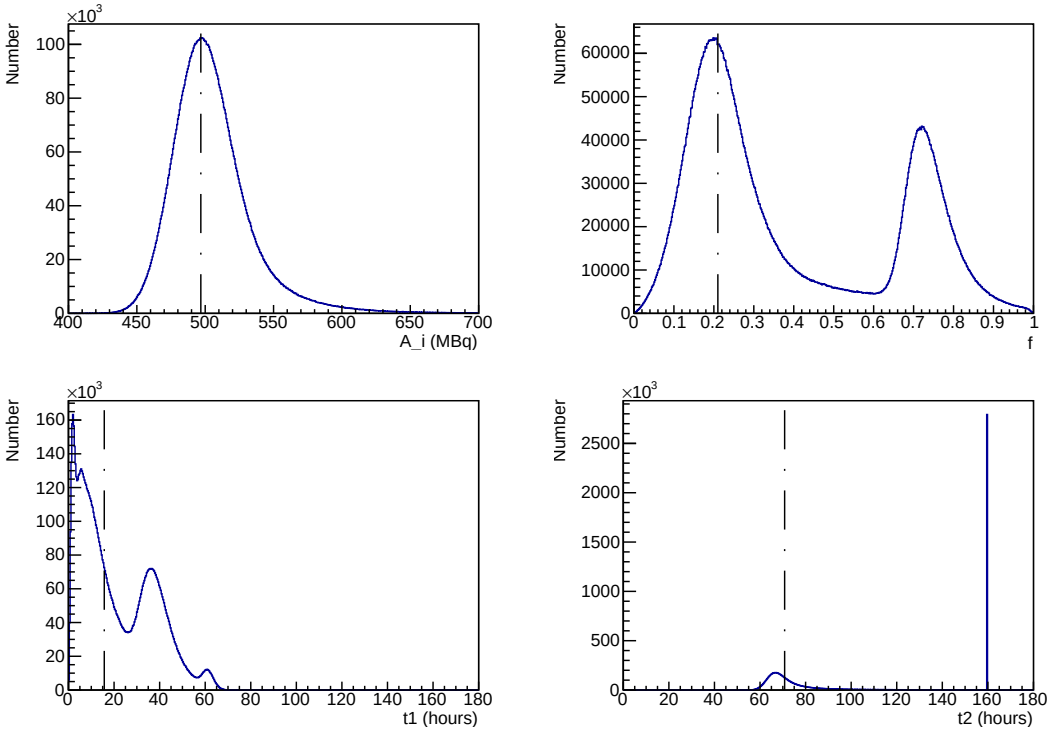

FIGURE 5.5: Histograms of the four fit parameters for ten million fits of the liver curve with a constant width. The true values of the parameters are indicated by vertical lines. The f values are bimodal as the biexponential in Equation (5.6) can be written either way around. Most of the fits result in t_2 being at the maximum allowed value.

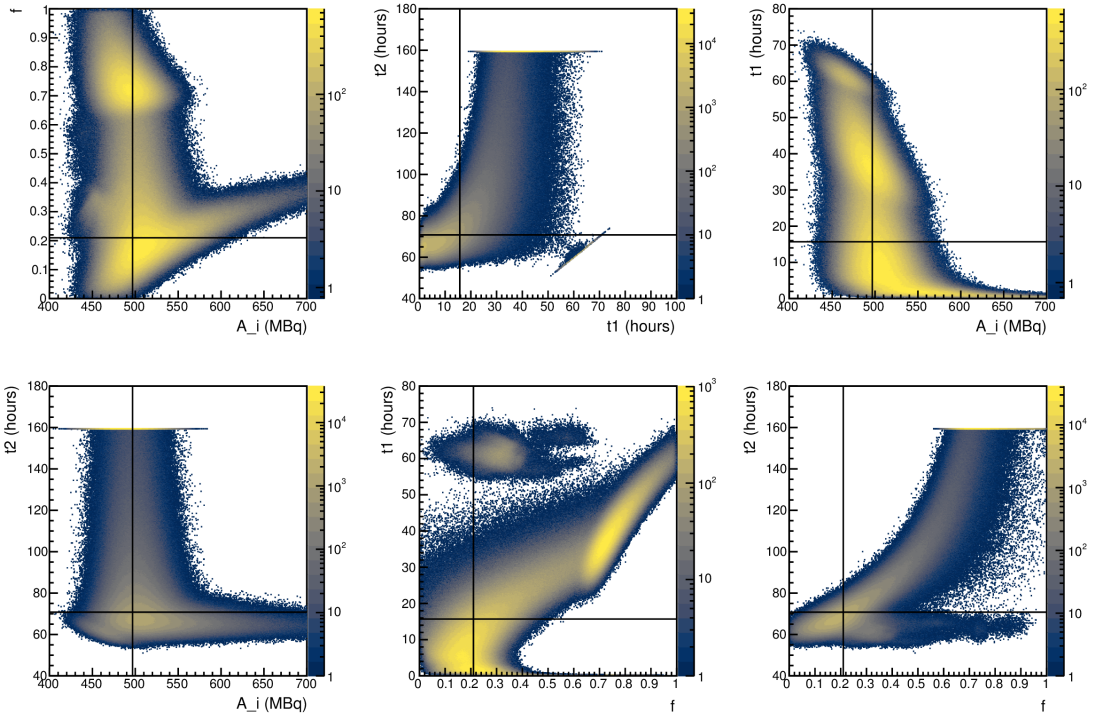

FIGURE 5.6: 2D histograms of the fit parameters for the liver curve with a constant width. The true values of the parameters are indicated with black lines. These histograms show the correlation between the fit parameters. Note the logarithmic colour scales.

5.2.3.2 Linearly scaled width, single function

Of the ten million fits of a biexponential function to points distributed according to the liver curve with a linearly scaled width, 2.2 % failed to converge. Figure 5.7 shows a histogram of the ratios of the fitted area under the curve to the fitted area under the curve. It can be seen that increasing the width of the distribution of the activity about the true value has increased the width of the histogram. The increase in likelihood of a ratio around 1.2 is still visible as a shoulder on the peak at 1. Histograms of the individual fit parameters are shown in Figure 5.8. The values of A_i are centred around the true value. The distribution of the f values is more strongly bimodal, with wider peaks. The t_1 values exhibit the same behaviour with multiple values being more likely, and most t_2 values are at the maximum allowed. Figure 5.9 again demonstrates the correlations between pairs of fit parameters. It can be seen that multiple combinations of f and t_1 are likely, with none being centred on the true values. In the histograms involving A_i, A_i is not obviously correlated with the other value.

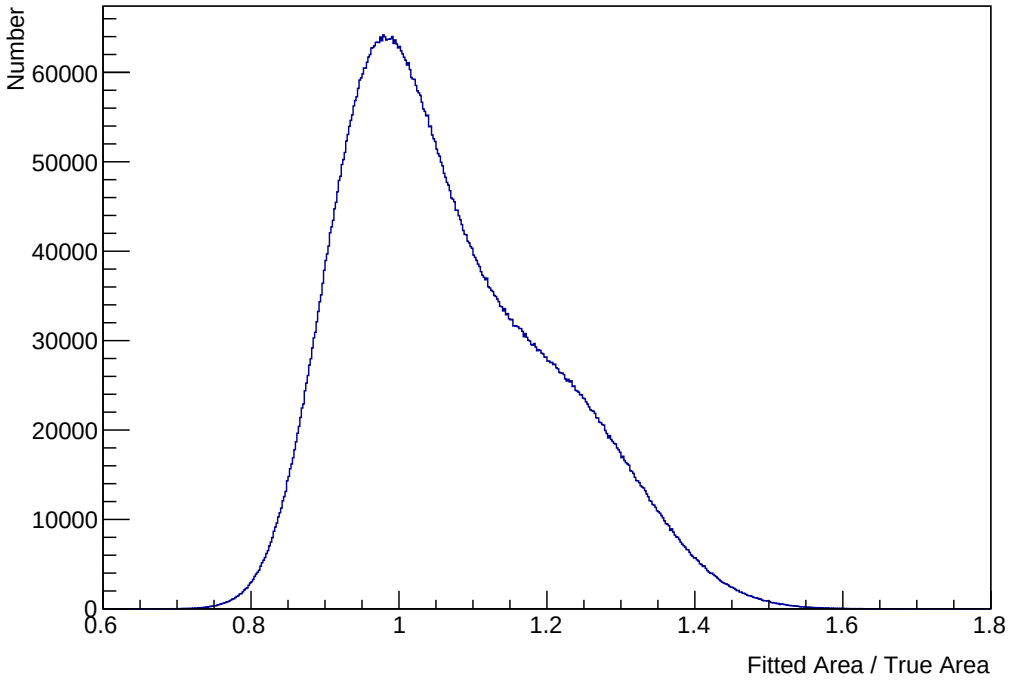

FIGURE 5.7: A histogram of the ratio of the area under the fitted curve and the area under the true curve for the liver with a linearly scaled width. The main peak of the histogram is around 1 and a shoulder can be seen near 1.2.

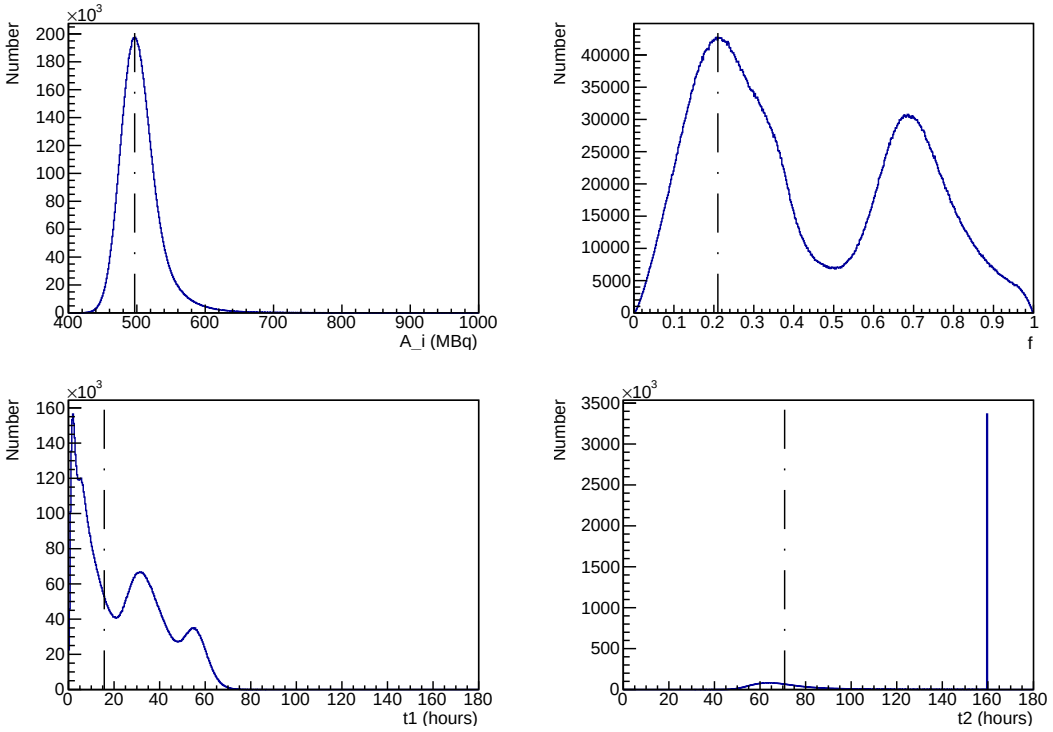

FIGURE 5.8: Histograms of the four fit parameters for ten million fits of the liver curve with a linearly scaled width. The true value of the parameters are indicated by vertical lines. The f values are bimodal as the biexponential in Equation (5.6) can be written either way around. Most of the fits result in t_2 being at the maximum value allowed by the fit constraints.

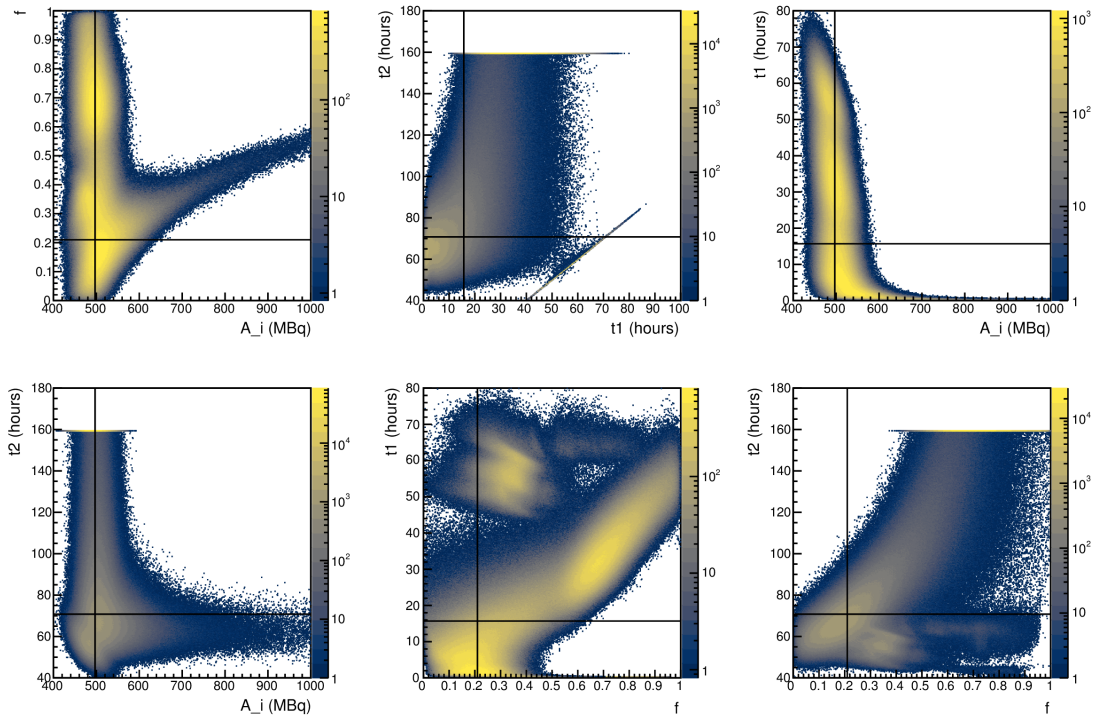

FIGURE 5.9: 2D histograms of the fit parameters for the liver curve with a linearly scaled width. The true values of the parameters are indicated with black lines. These histograms show the correlation between the fit parameters. Note the logarithmic colour scales.

5.2.3.3 Constant width, multiple functions

Figure 5.10 shows a histogram of the ratio of the fitted area under the curve to the true area for the liver TAC using the NUKFIT-style strategy and a 5 % width for all time points. Qualitatively the distribution is more Gaussian than those when only a biexponential is fitted. There is however a tail to higher ratios. This tail is visible in a histogram of the ratio and the percentage uncertainty, shown in Figure 5.11. The calculated uncertainty on points with ratios greater than 1.2 is lower than expected. It should be noted that the uncertainty is calculated based on the assumption that Gaussian error propagation can be used. The distributions of fit parameters for functions with 3 or 4 parameters which pass the quality control are not symmetric. The assumption that Gaussian error propagation can be used may not hold. Figure 5.12 shows the frequency with which functions passed the quality control. Functions f_1 and f_2 pass the quality control for all the sets of data points. Function f_3 passes less than 1 % of the time. Functions f_4 and f_{4a} pass for less than 0.1 % of the sets of data points. Function F_{4b} did not pass the quality control for any of the sets of data points.

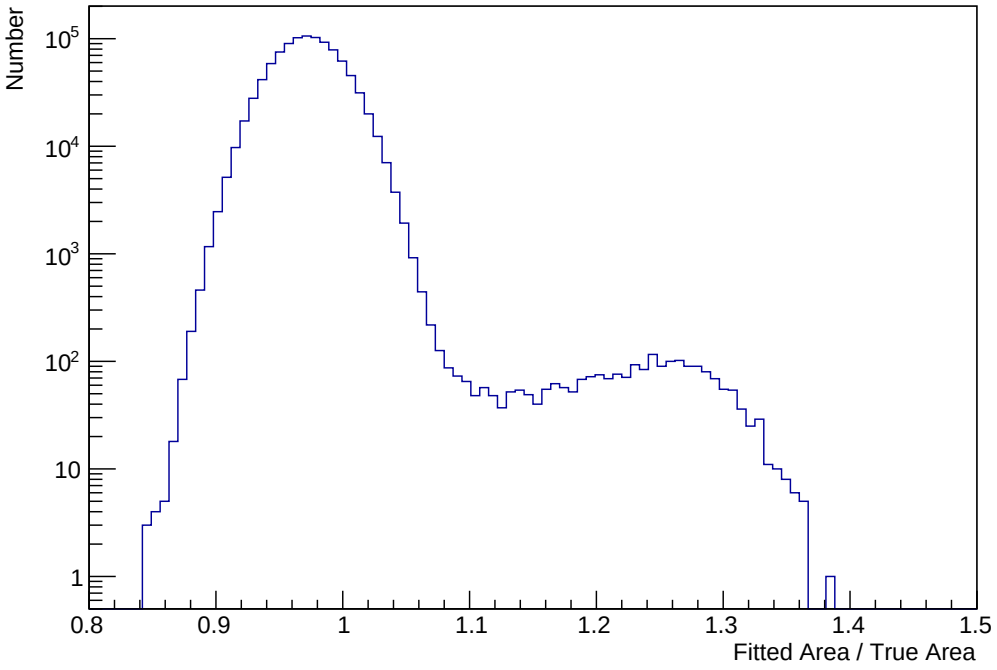

FIGURE 5.10: A histogram of the ratio of the area under the curve and the area under the true curve for the liver TAC with a constant width using the NUKFIT-style area calculation. There is tail of the distribution up to a ratio of around 1.4. This likely indicates a local minimum of the optimisation function. This distribution is an improvement on the results for a biexponential fitting function as many fewer fits result in an overestimate of the area under the curve. Note the logarithmic scale on the y-axis.

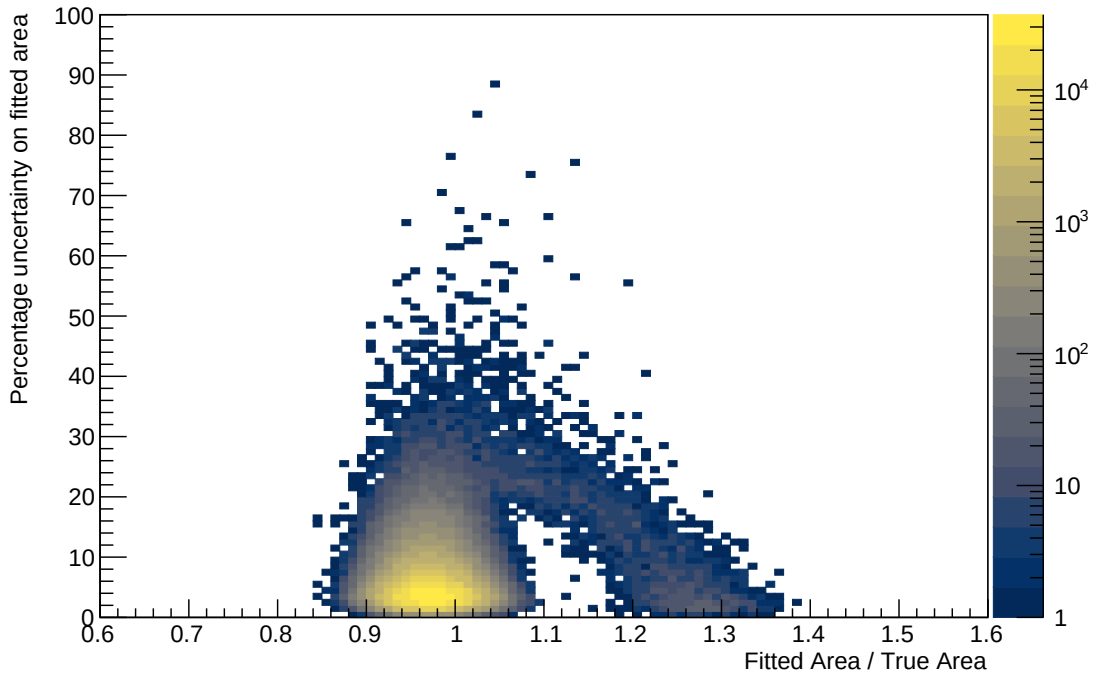

FIGURE 5.11: A histogram of the ratio of the area under the curve and the area under the true curve and the uncertainty on the area for the liver TAC with a constant width using the NUKFIT-style area calculation. Note the logarithmic colour scale.

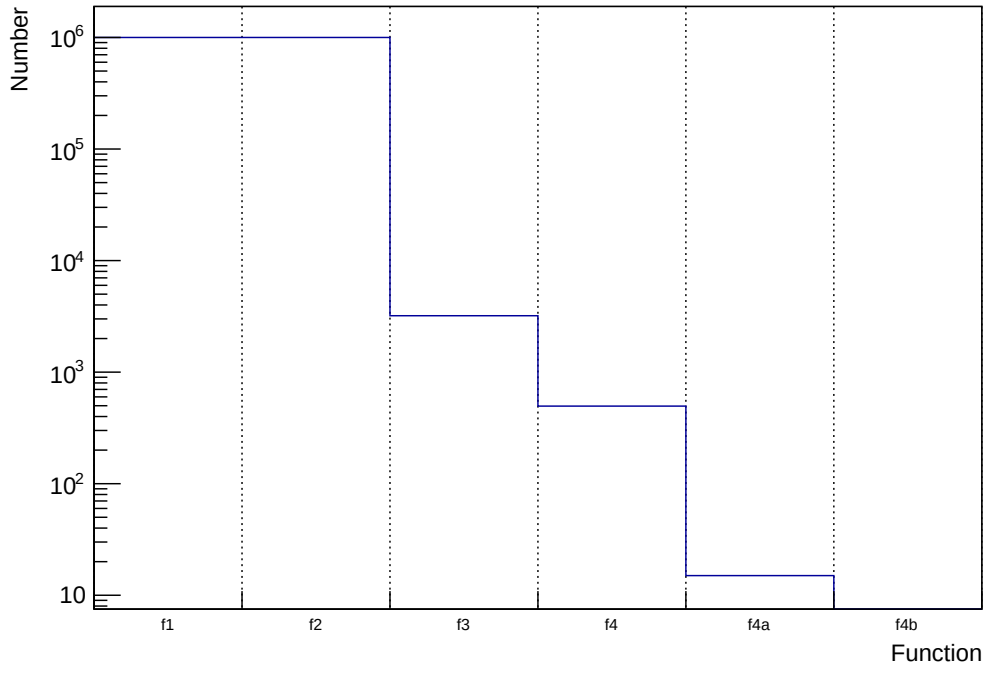

FIGURE 5.12: A histogram showing the frequency of each function passing the quality control for the liver TAC with a constant width using the NUKFIT-style area calculation. Functions with more than two parameters rarely pass the quality control.

5.2.3.4 Linearly scaled width, multiple functions

A histogram of the ratio of the fitted area to the true area for the liver TAC using the NUKFIT-style strategy and a linearly scaled width is shown in Figure 5.13. The distribution is broader than when a constant perturbation width is used but the tail at larger ratios is still evident. A histogram of the ratio and the percentage uncertainty, in Figure 5.14, again shows a possibility of overestimating the ratio with a small uncertainty. Again the appropriateness of using Gaussian error propagation is questionable. Figure 5.15 shows the frequency with which each function passes the quality control. As with the constant width functions f_1 and f_2 pass the quality control for all sets of data points. Function f_3 is more likely to pass the quality control, but still only passes for roughly 1 % of the sets of data points. Function f_4 is roughly ten times more likely to pass the quality control. Function f_{4a} again passes for less than 0.01 % of the sets of data points and function f_{4b} never passed the quality control.

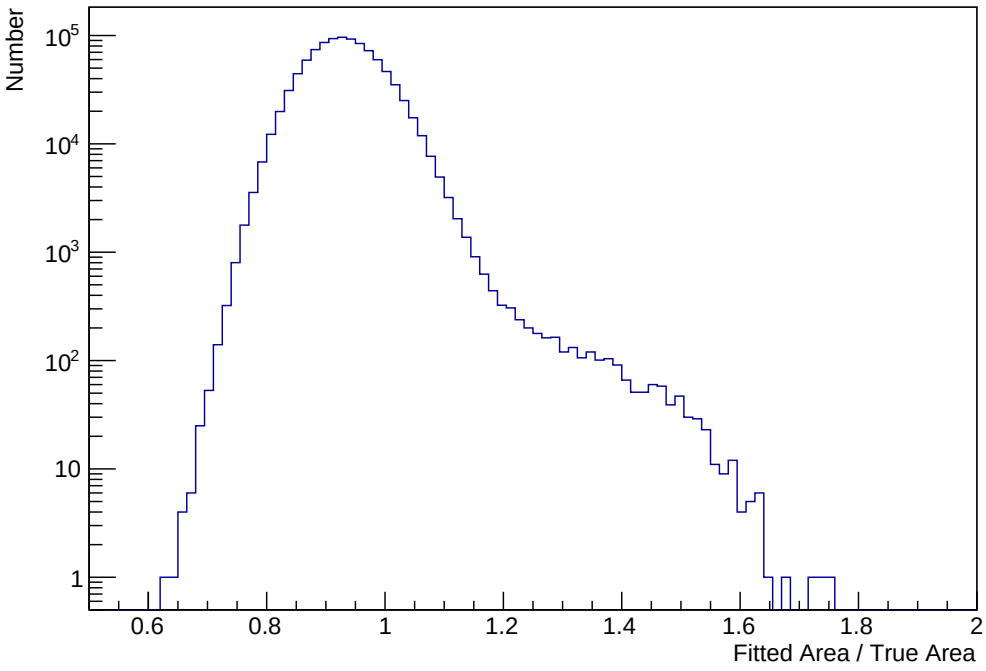

FIGURE 5.13: A histogram of the ratio of the area under the curve and the area under the true curve for the liver TAC with a linearly scaled width using the NUKFIT-style area calculation. Note the logarithmic scale. The distribution is broader than that for the fits using a constant width.

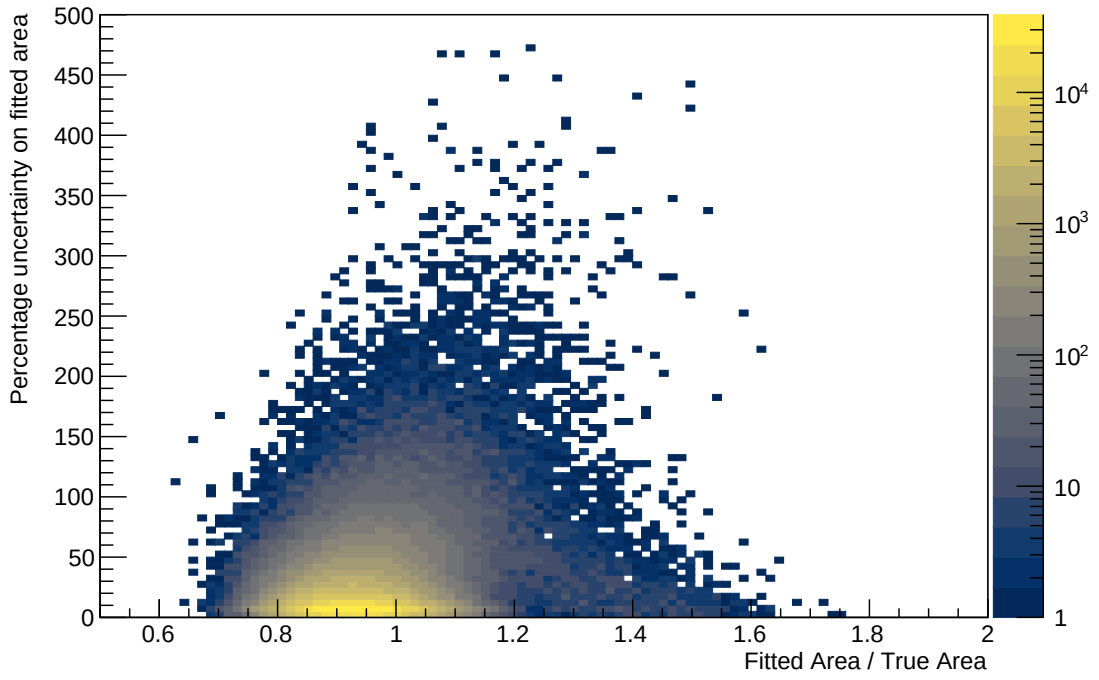

FIGURE 5.14: A histogram of the ratio of the area under the curve and the area under the true curve and the uncertainty on the area for the liver TAC with a varied width using the NUKFIT-style area calculation. Note the logarithmic colour scale.

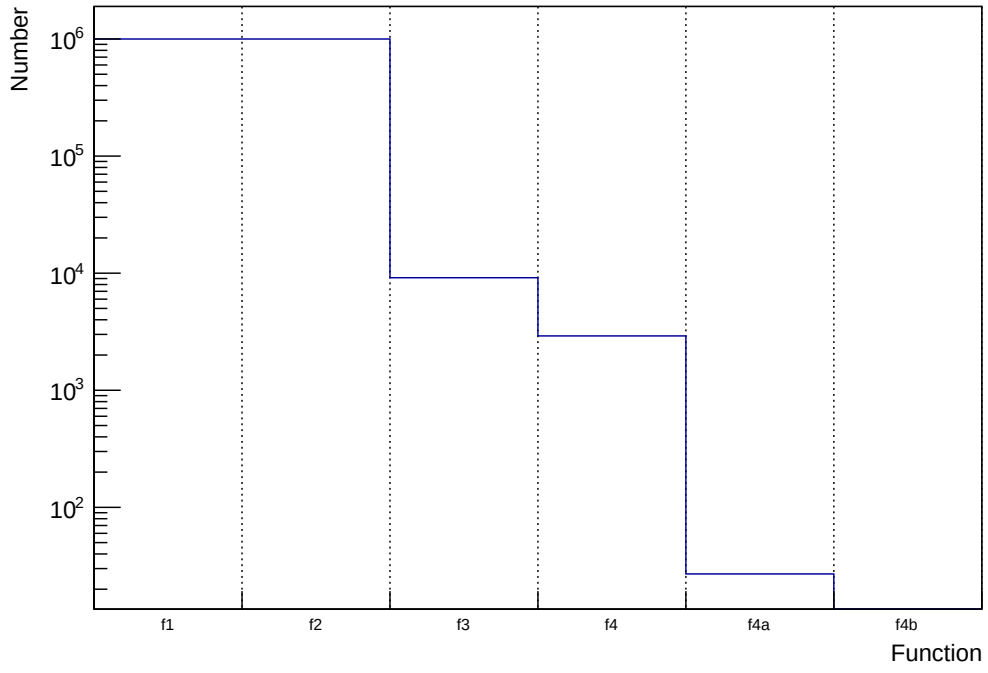

FIGURE 5.15: A histogram showing the frequency of each function passing the quality control for the liver TAC with a varied width using the NUKFIT-style area calculation. Functions with more than two parameters rarely pass the quality control.

5.2.4 Kidney

As for the liver, the results for fitting a single function are presented first, followed by the results for the NUKFIT-style strategy.

5.2.4.1 Constant width, single function

Of the ten million fits of a biexponential function to points distributed according to the kidney curve with a constant width, 0.54 % failed to converge. It is evident that the fits to the kidney curve were more successful than the fits to the liver curve. The t_1 and t_2 parameters are more different for the kidney than for the liver. This reduces the impact of parameter redundancy. A histogram of the ratio of the fitted area under the curve is shown in Figure 5.7. Most of the values are centred around one, but a small secondary peak is visible above 1.2. In Figure 5.17 it can be seen that the values of the fit parameters are centred on the true values. For a minority of the fits, t_1 is set to the maximum value allowed. Figure 5.18 shows histograms of pairs of the fit parameters. For all the histograms the values are centred on the true values. However, the shapes of the histograms are far from 2D Gaussians.

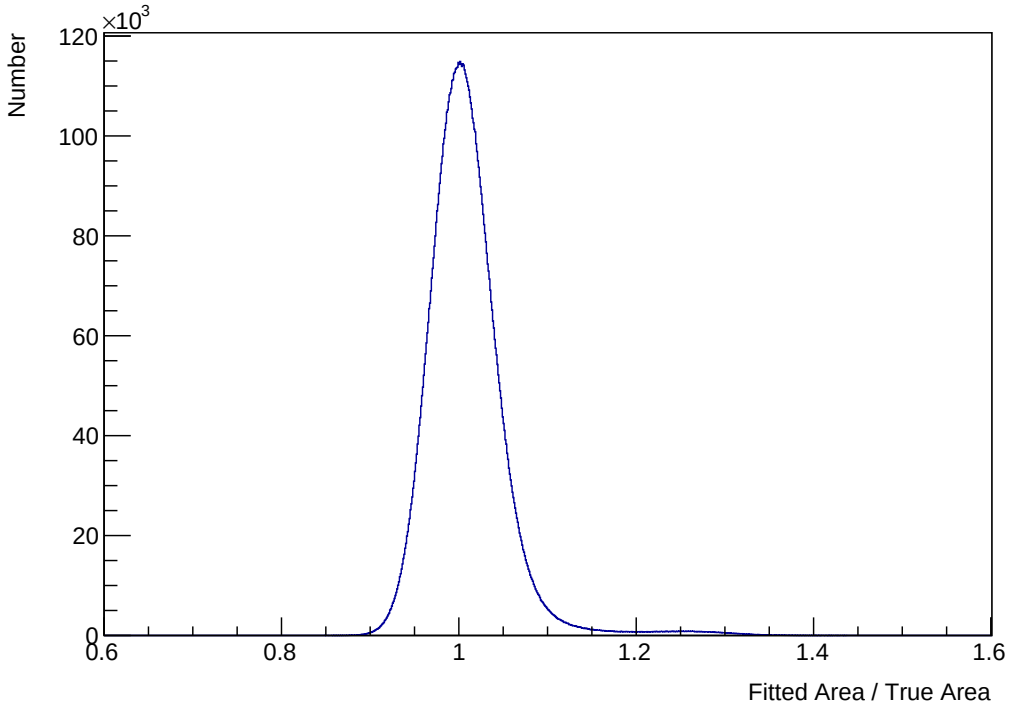

FIGURE 5.16: A histogram of the ratio of the area under the fitted curve and the area under the true curve for the kidney with a constant width. The main peak of the histogram is around 1, but there is a small likelihood of overestimation.

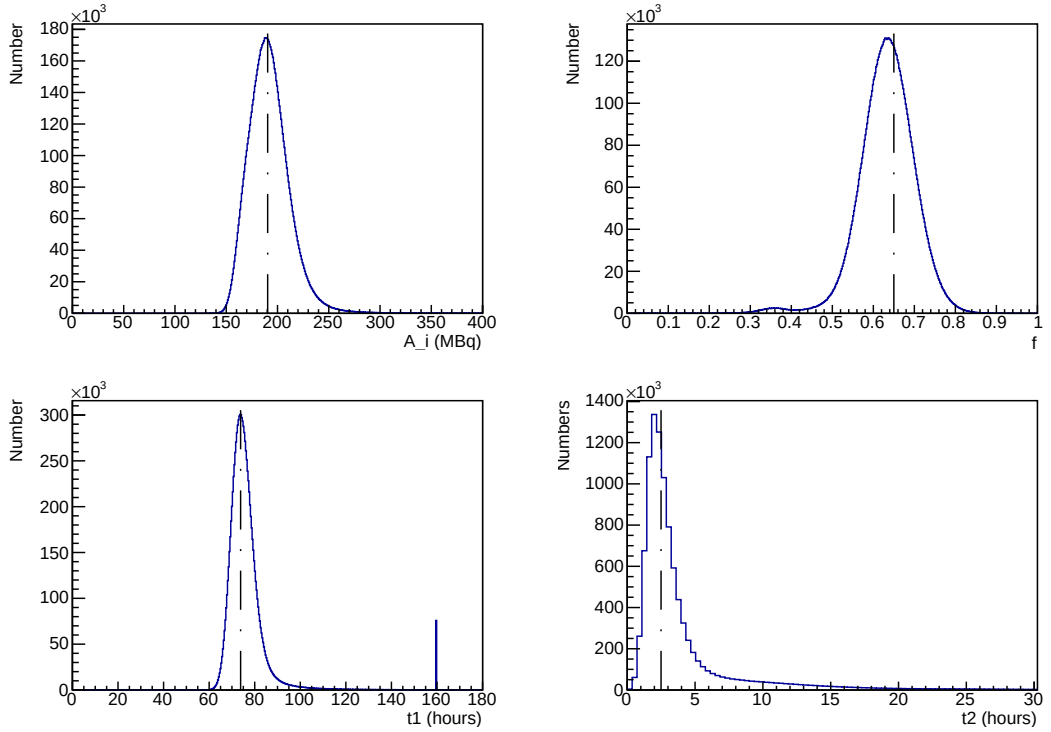

FIGURE 5.17: Histograms of the four fit parameters for ten million fits of the kidney curve with a constant width. The true value of the parameters are indicated by vertical lines. The histogram for the values of t_2 is not symmetric.

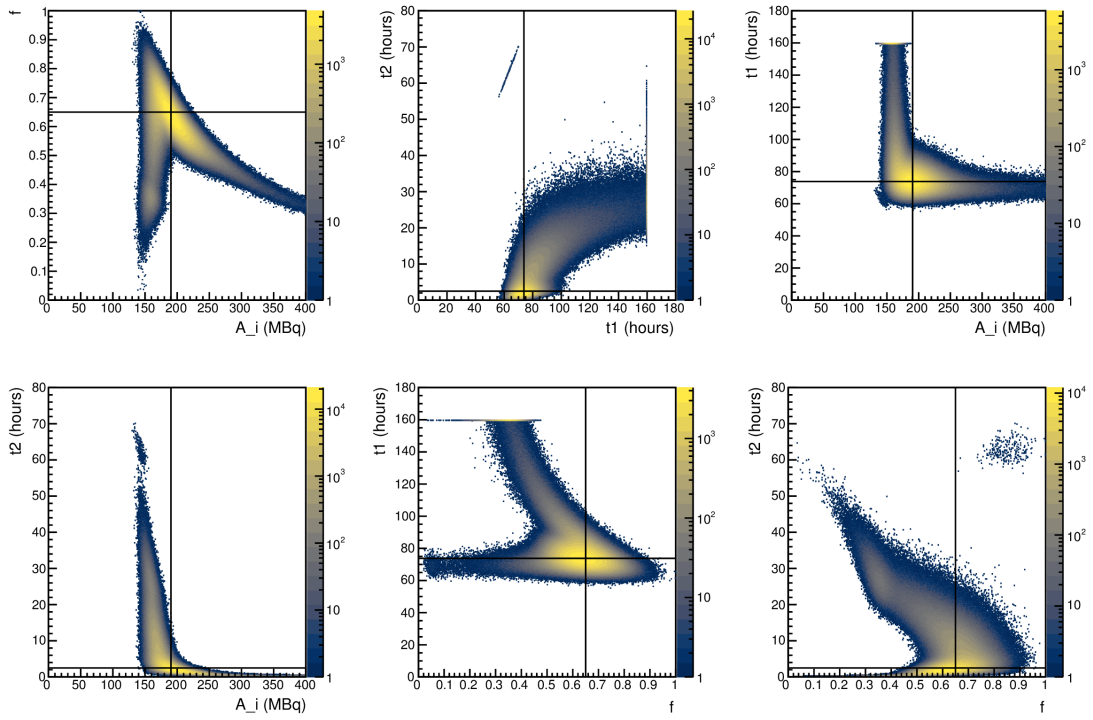

FIGURE 5.18: 2D histograms of the fit parameters for the kidney curve with a constant width. The true values of the parameters are indicated with black lines. These histograms show the correlation between the fit parameters. Note the logarithmic colour scales.

5.2.4.2 Linearly scaled width, single function

Of the ten million fits of a biexponential function to points distributed according to the kidney curve with a linearly scaled width 2.24 % resulted in a failure of the fit to converge. Figure 5.19 shows a histogram of the ratio of the fitted area under the curve to the true area. The main peak is much broader than with a constant width of perturbation and a tail at higher ratios can be seen. Histograms of the fit parameters are shown in Figure 5.20. It can be seen that the values of A_i, f and t_2 are generally correct but do not follow simple Gaussian distributions. Further, t_1 is often the largest value allowed by the fit. In Figure 5.21 2D histograms of the fit parameters are shown. While the distributions are generally centred on the true values, incorrect values may be correlated. However the distributions are not the expected ellipses which would indicate correlated variables following a Gaussian distribution.

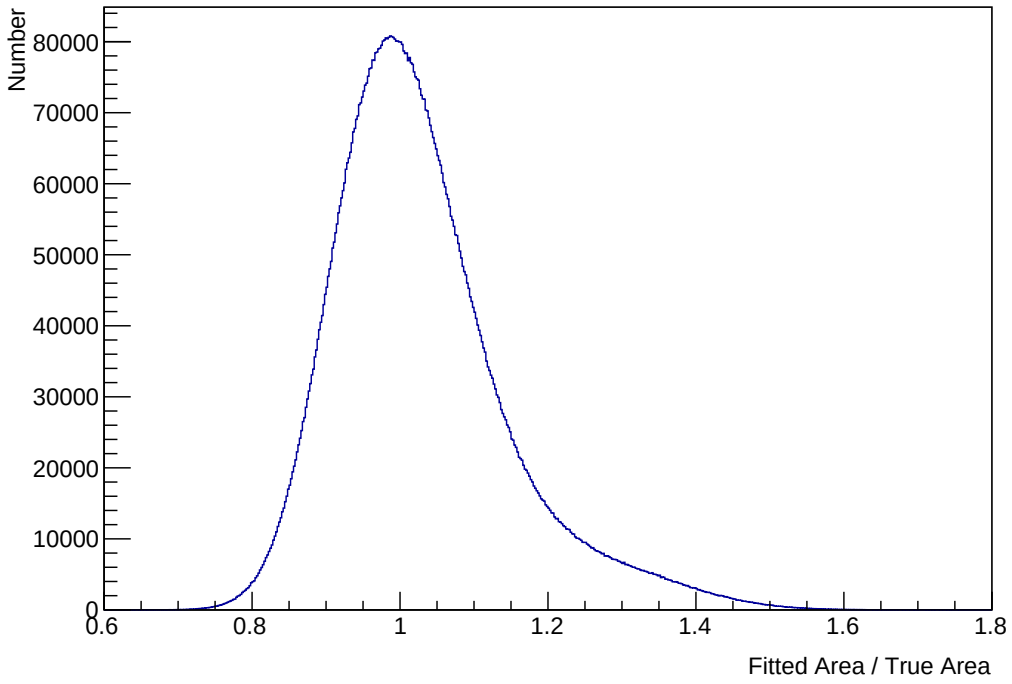

FIGURE 5.19: A histogram of the ratio of the area under the fitted curve and the area under the true curve for the kidney with a linearly scaled width. The main peak of the histogram is around 1, but the distribution is skewed towards higher ratios.

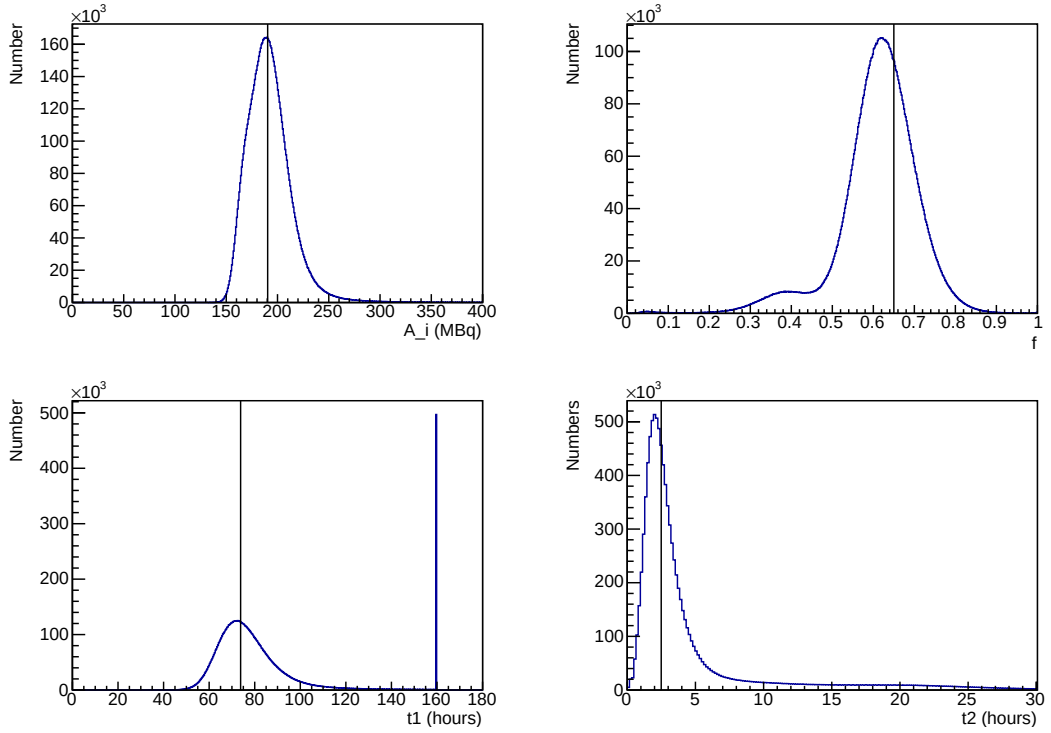

FIGURE 5.20: Histograms of the four fit parameters for ten million fits of the kidney curve with a linearly scaled width. The true value of the parameters are indicated by vertical lines.

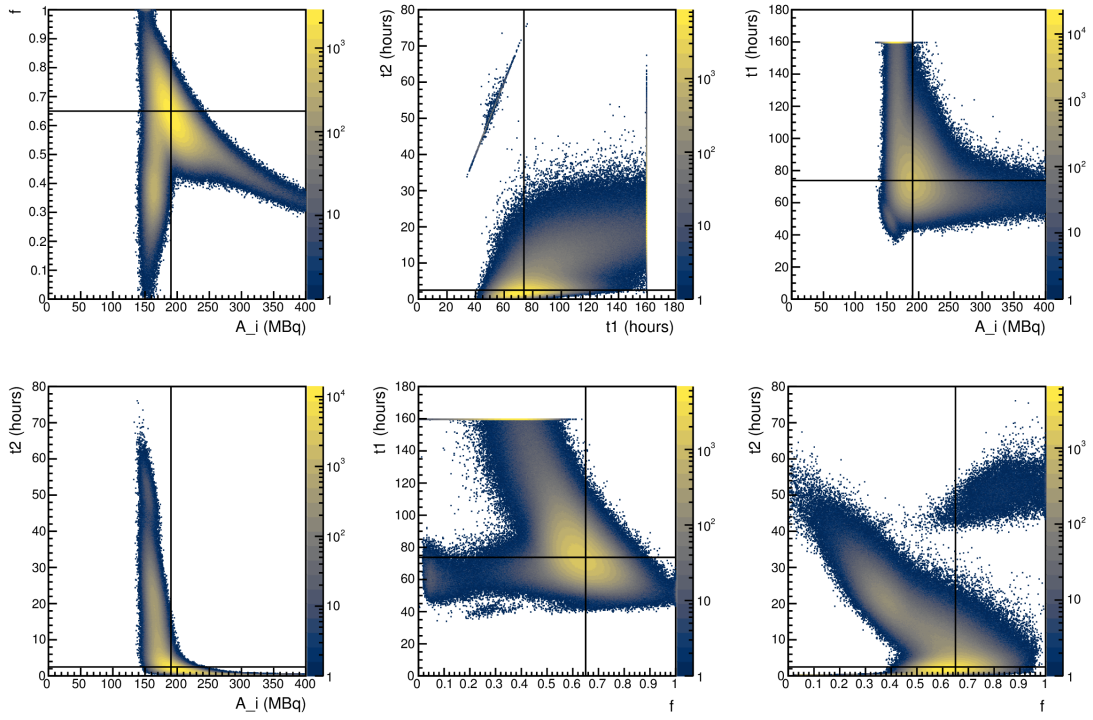

FIGURE 5.21: 2D histograms of the fit parameters for the kidney curve with a linearly scaled width. The true values of the parameters are indicated with black lines. These histograms show the correlation between the fit parameters. Note the logarithmic colour scales.

5.2.4.3 Constant width, multiple functions

Figure 5.22 shows a histogram of the ratios of the area under the fitted curve and the true area under the curve for the kidney TAC using the NUKFIT-style method and a constant width. The distribution is clearly not Gaussian or symmetric so describing it with a mean and width is unlikely to be suitable. In Figure 5.23 a histogram of the percentage uncertainty on the area under the curve and the ratio shows a possibility of overestimating the area while estimating a low uncertainty. Figure 5.24 shows the frequency of fits passing the quality control. Unlike for the liver, function f_3 passes the quality control for roughly 20 % of the sets of data points. Functions f_4 and f_{4a} only pass the quality control for approximately 0.001 % of the sets of data points.

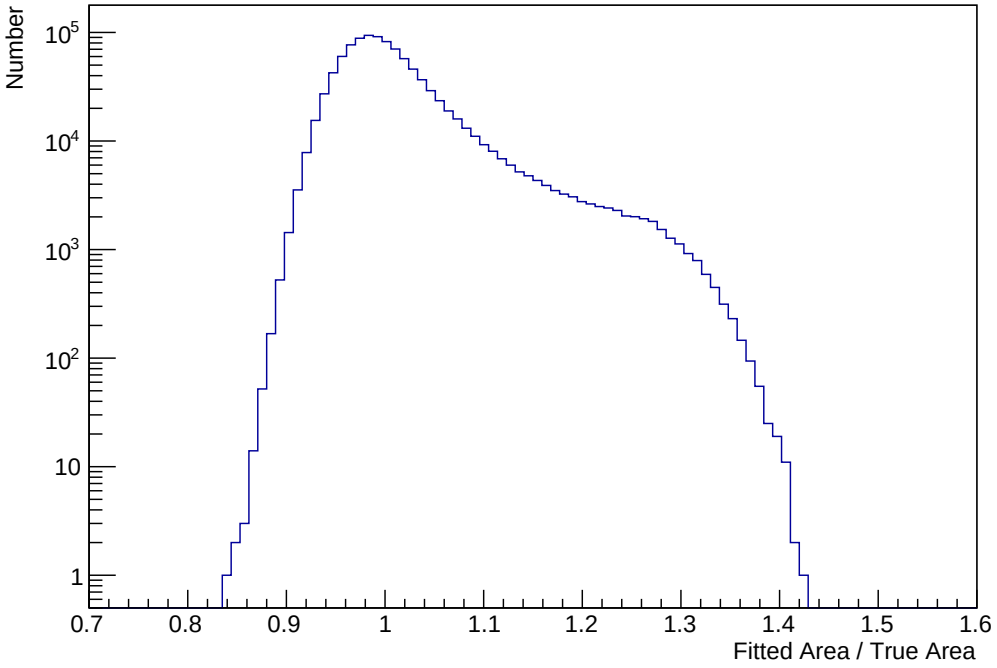

FIGURE 5.22: A histogram of the ratio of the area under the curve and the area under the true curve for the kidney TAC with a constant width using the NUKFIT-style area calculation. Note the logarithmic scale. There is a shoulder around 1.2, but this is small.

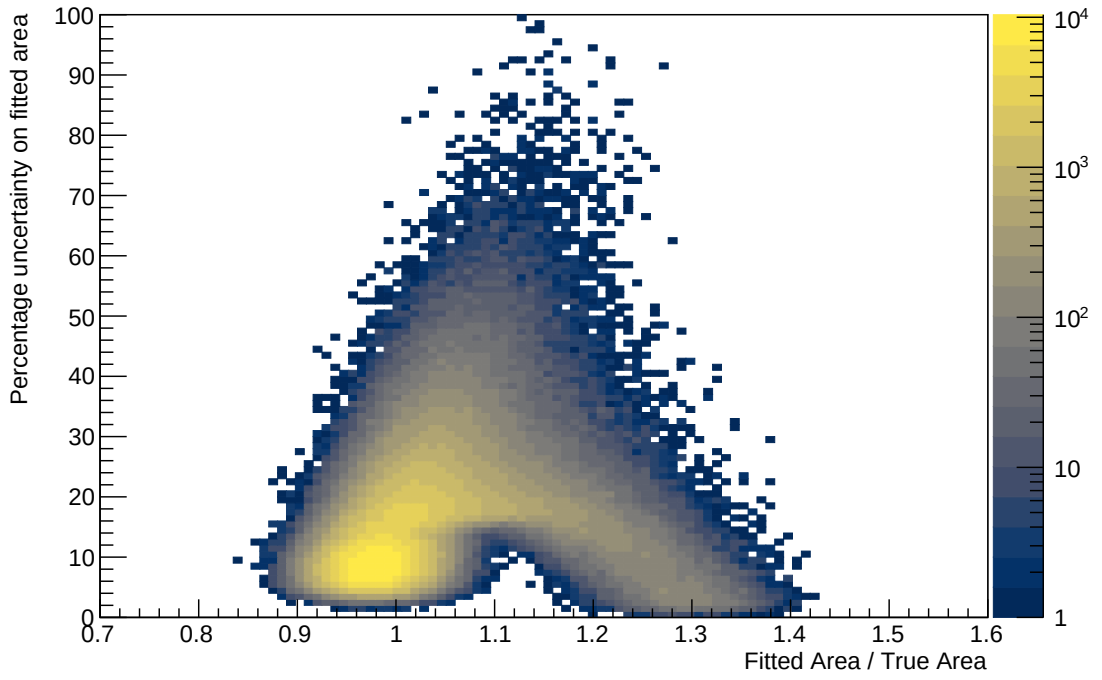

FIGURE 5.23: A histogram of the ratio of the area under the curve and the area under the true curve and the uncertainty on the area for the kidney TAC with a constant width using the NUKFIT-style area calculation. Note the logarithmic colour scale.

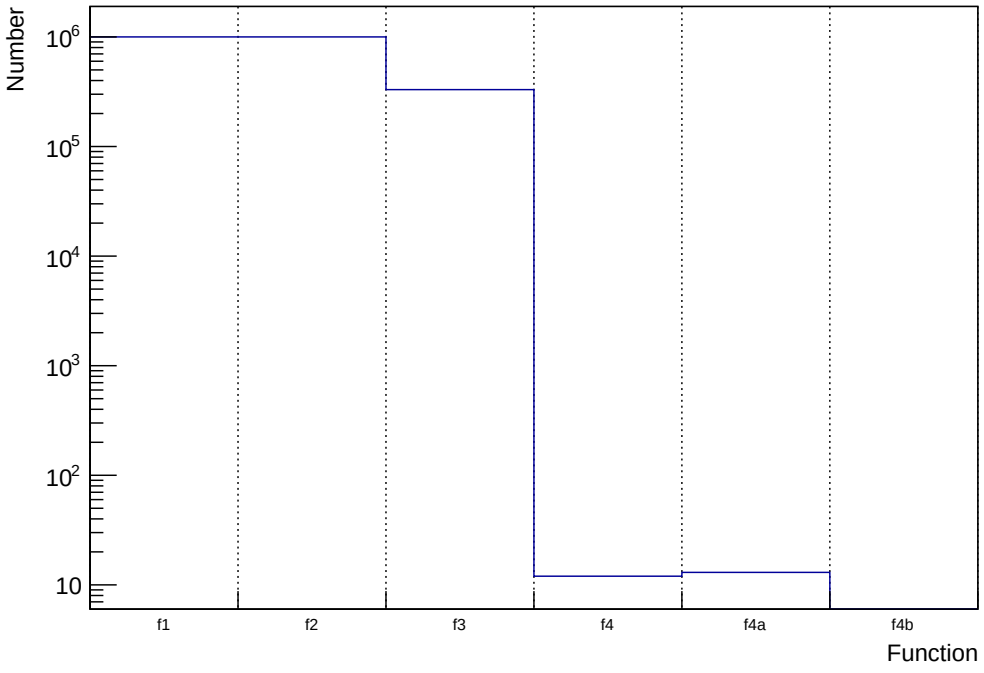

FIGURE 5.24: A histogram showing the frequency of each function passing the quality control for the kidney TAC with a constant width using the NUKFIT-style area calculation. Functions with more than two parameters rarely pass the quality control.

5.2.4.4 Linearly scaled width, multiple functions

Figure 5.25 shows a histogram of the ratio of the fitted area under the curve and the true area under the curve for the kidney TAC using the NUKFIT-style method and a linearly scaled width. The distribution is broader than when a constant perturbation width was used, and is still not Gaussian. A histogram of the percentage uncertainty on the fitted area and the ratio, shown in Figure 5.26, again shows the possibility of overestimating the area under the curve while underestimating the uncertainty if Gaussian error propagation is used. The frequencies with which each function passes the quality control are shown in Figure 5.27. Functions f_1, f_2 and f_3 pass the quality control for approximately the same number of data sets as with a constant width. Functions f_4 is more likely to pass the quality control, passing for roughly 0.2 % of sets of data points. While this is a large increase, it is still a small percentage of all sets of data points.

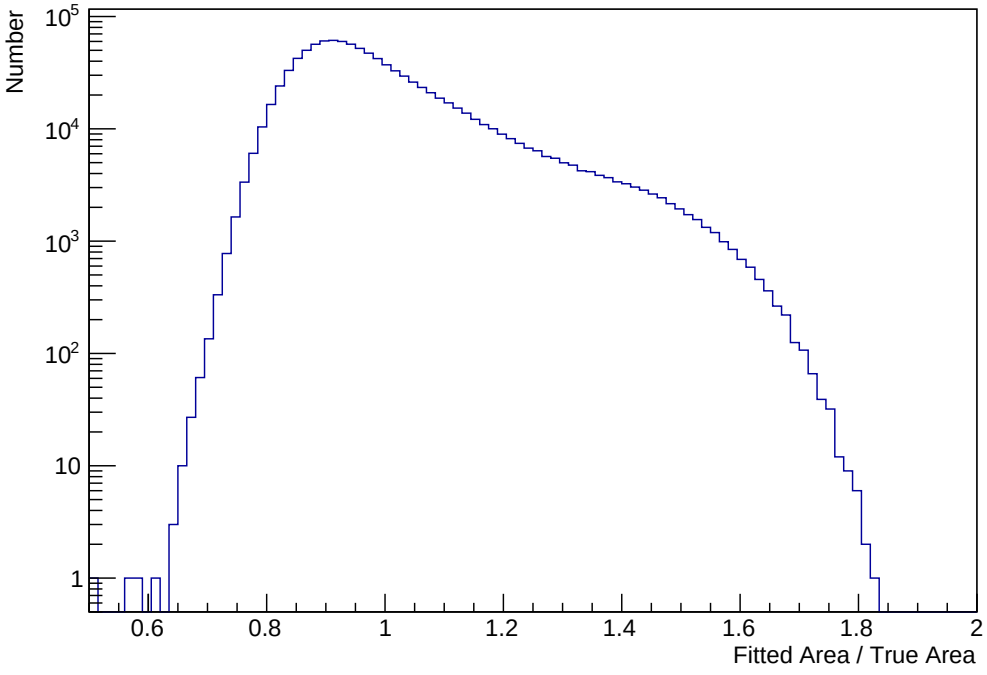

FIGURE 5.25: A histogram of the ratio of the area under the curve and the area under the true curve for the kidney TAC with a linearly scaled width using the NUKFIT-style area calculation. Note the logarithmic scale. The shape is broader than that for the fits with a constant width.

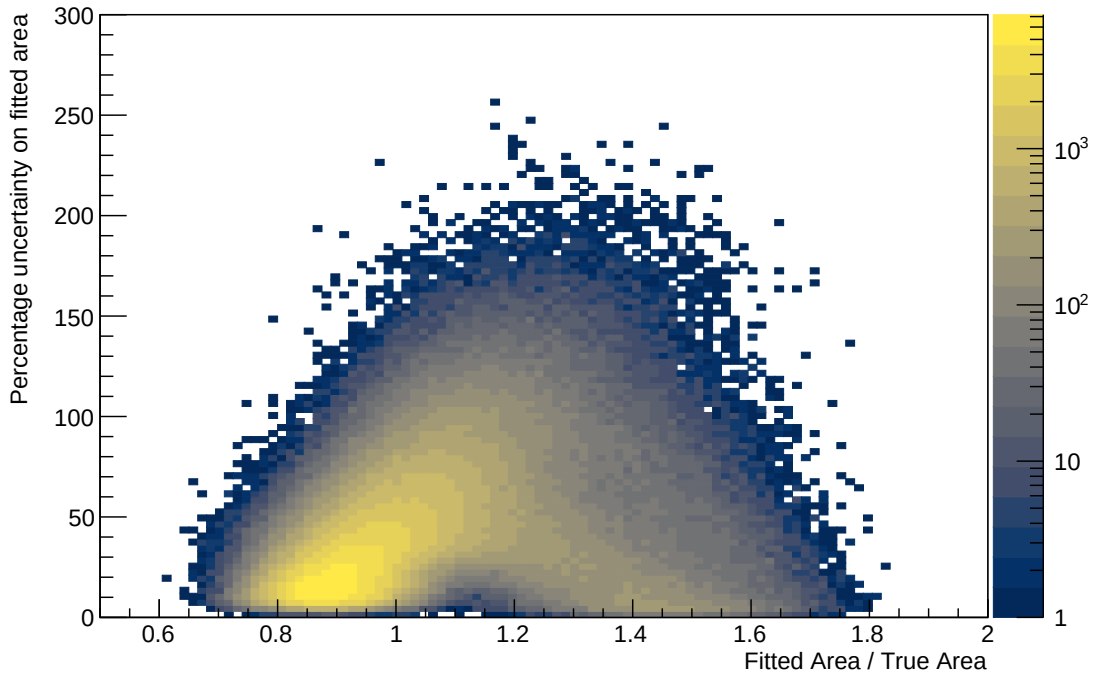

FIGURE 5.26: A histogram of the ratio of the area under the curve and the area under the true curve and the uncertainty on the area for the kidney TAC with a linearly scaled width using the NUKFIT-style area calculation. Note the logarithmic colour scale.

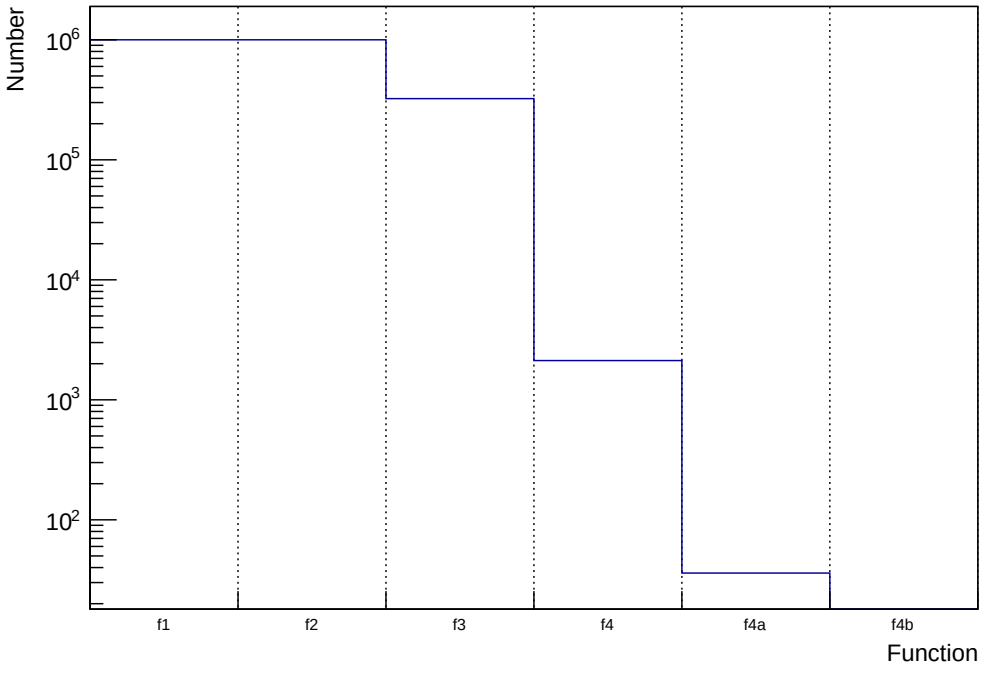

FIGURE 5.27: A histogram showing the frequency of each function passing the quality control for the kidney TAC with a linearly scaled width using the NUKFIT-style area calculation. Functions with more than two parameters rarely pass the quality control.

5.2.5 Spleen

Two different functions were fitted to points generated for the spleen. The first function is shown in Equation (5.7), and all the parameters were allowed to vary. It should be noted that the parameters were not constrained such that the function was positive for all time. As a result the best fit to the data may be un-physical. The second function is shown in Equation (5.8). This method forces the function to pass through the origin, and is therefore more strongly constrained. In addition there are only three fit parameters with six data points. Results are shown for both functions using a constant perturbation width and a time-dependent width. Results using the NUKFIT-style strategy are then presented.

5.2.5.1 Free activities, constant width

Out of the ten million fits performed using a free biexponential to the spleen TAC with a constant width, only 19 failed to converge. While most of the fits result in areas within 20 % of the true area, as shown in Figure 5.31, it can be seen in Figure 5.29 that the fit rarely converges to the correct value for A_2 and t_2. It can also be seen that there are significant peaks at the limits of the fit for A_1 and t_1. The correlations between the parameters are shown in Figure 5.30. The distributions are far from the expected clumps near the true values.

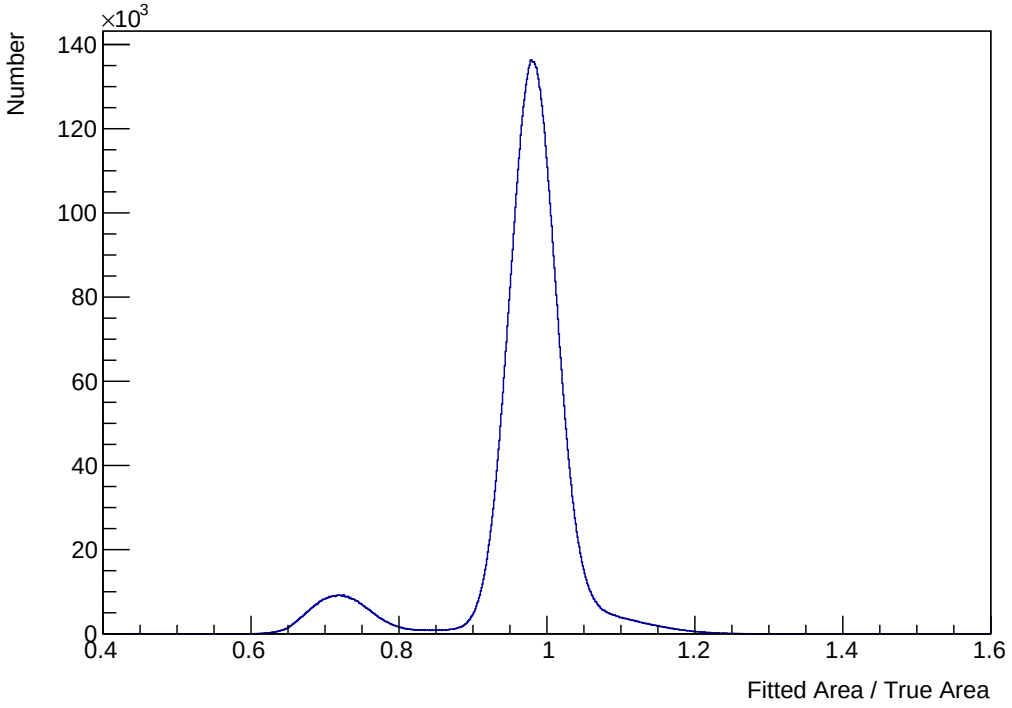

FIGURE 5.28: A histogram of the ratio of the area under the fitted curve and the area under the true curve for the spleen using Equation (5.7) and a constant width. The main peak of the histogram is around 1, but there is a secondary peak around 0.7. This likely indicates a local minimum of the optimisation function.

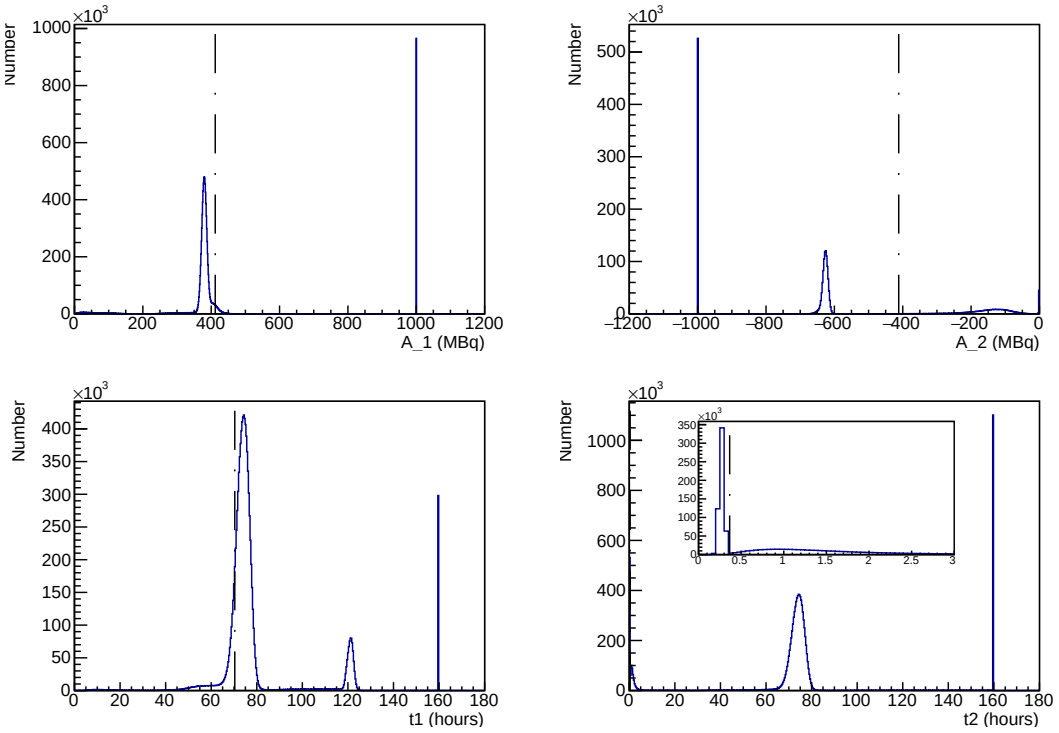

FIGURE 5.29: Histograms of the four fit parameters for ten million fits of the spleen curve using Equation (5.7) and a constant width. The true value of the parameters are indicated by vertical lines. It can be seen that A_1 and A_2 tend to be a the fit limits. The inset in the t_2 plot shows the region near the true value. It can be seen that few of the fits result in a value of t_2 close to the true value.

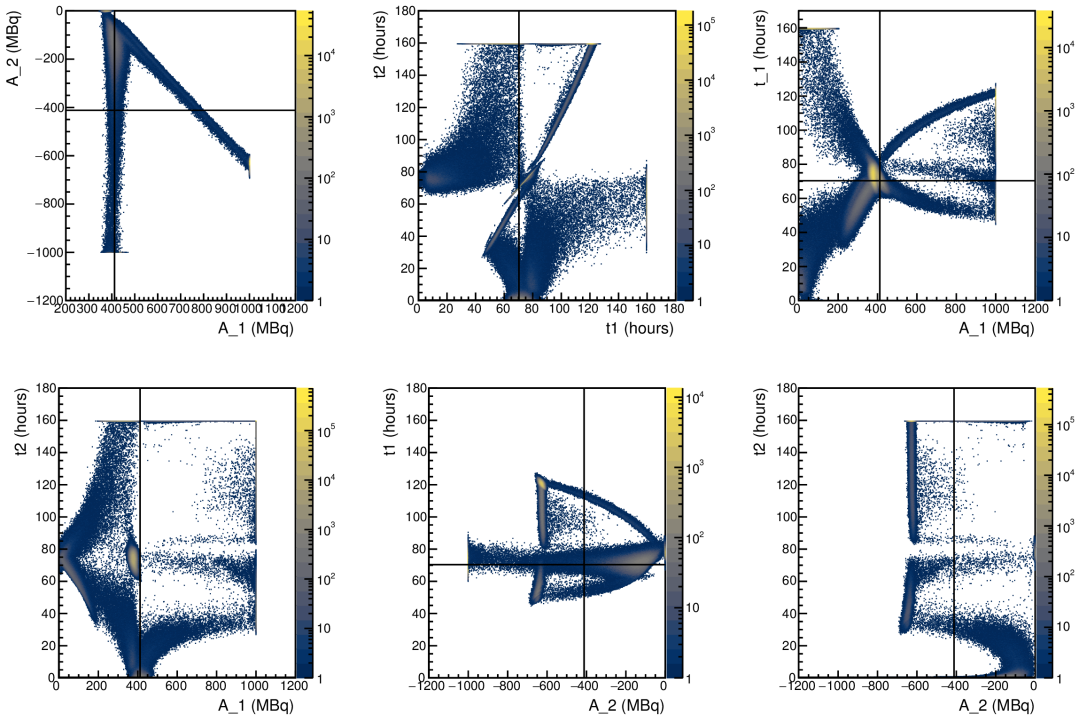

FIGURE 5.30: 2D histograms of the fit parameters for the spleen curve using Equation (5.7) and a constant width.. The true values of the parameters are indicated with black lines. These histograms show the correlation between the fit parameters. Note the logarithmic colour scales.

5.2.5.2 Single A_i, constant uncertainty

When the fit is constrained to pass through the origin by using Equation (5.8), the results greatly improve. None of the ten million fits to data distributed according to the spleen TAC using a constant width failed to converge. A histogram of the ratio of the fitted area to the true area has a single peak and is distributed around 1. It can be seen in Figure 5.32 that the values of the fit parameters are centred on the true values. Figure 5.33 shows the expected 2D distribution of the fit parameters. The histograms are centred on the true values of the true parameters, as expected from the individual distributions of the parameters.

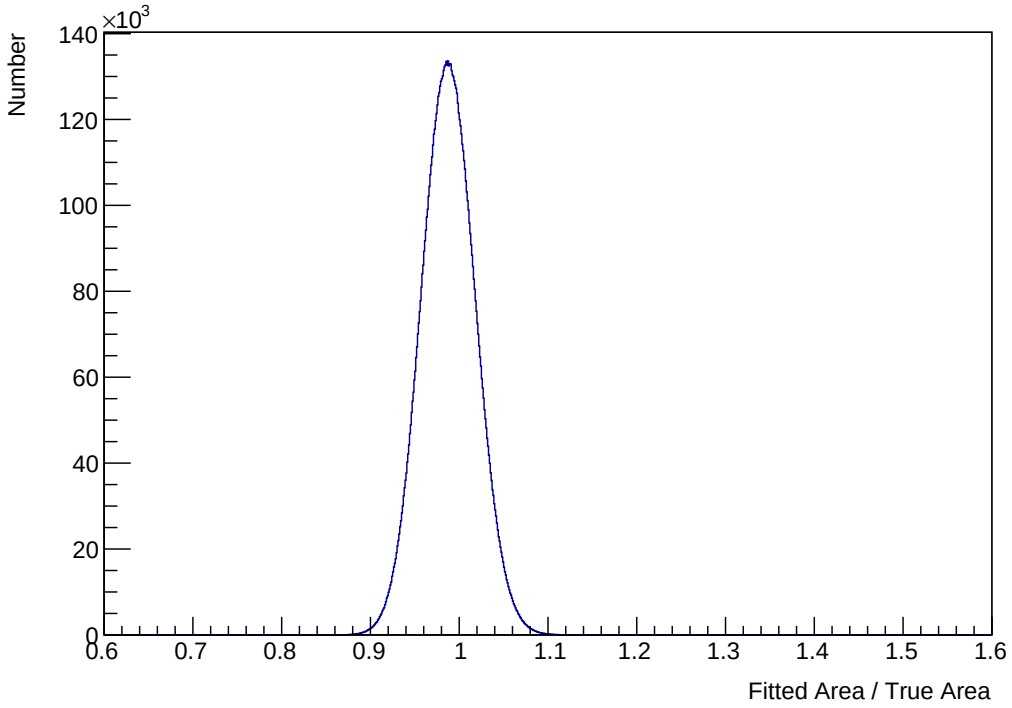

FIGURE 5.31: A histogram of the ratio of the area under the fitted curve and the area under the true curve for the spleen using Equation (5.8) and a constant width. The main peak of the histogram is around 1.

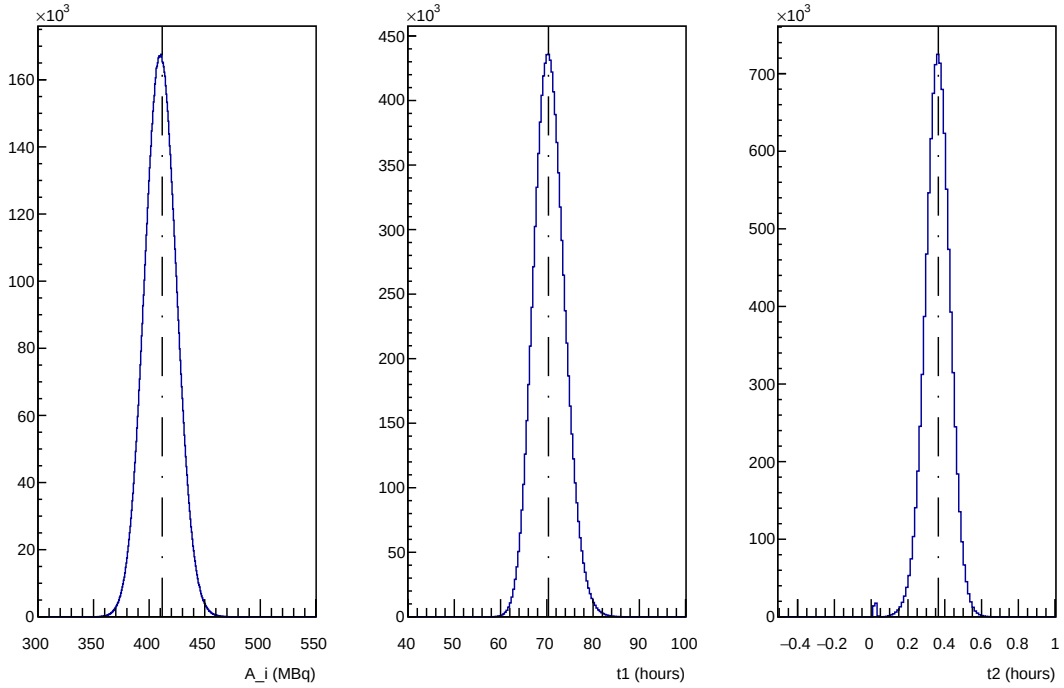

FIGURE 5.32: Histograms of the three fit parameters for ten million fits of the spleen using Equation (5.8) and a constant width. The true value of the parameters are indicated by vertical lines. It can be seen that the histograms are centred on the true values.

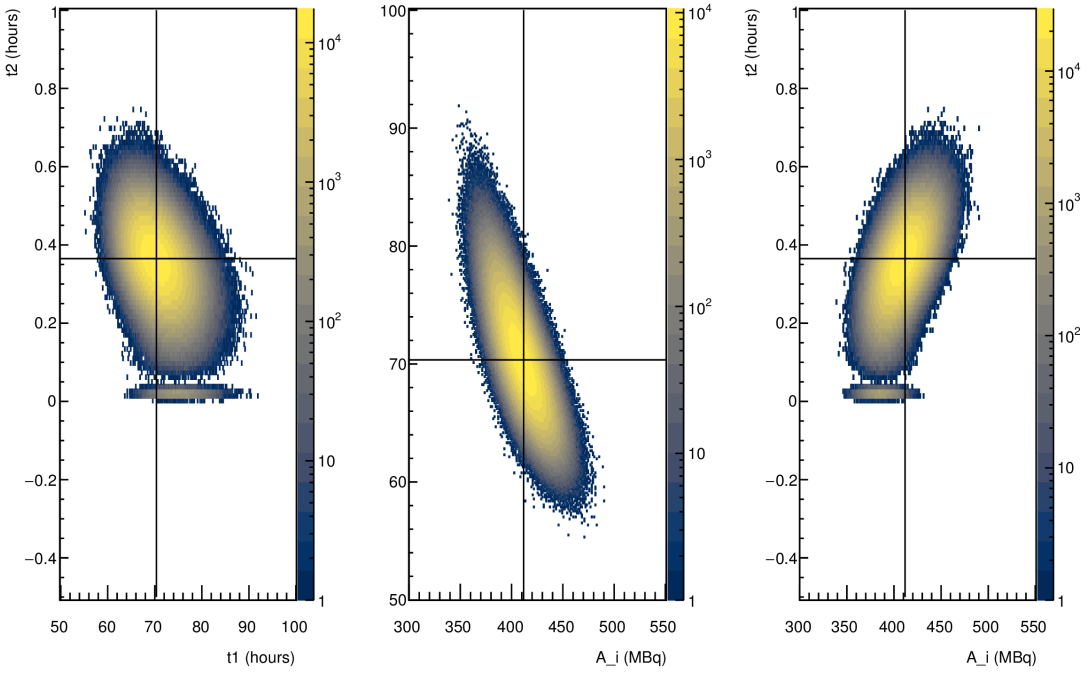

FIGURE 5.33: 2D histograms of the fit parameters for the spleen using Equation (5.8) and a constant width. The true values of the parameters are indicated with black lines. These histograms show the correlation between the fit parameters. These are close to the expected 2D Gaussisans. Note the logarithmic colour scales.

5.2.5.3 Single A_i, linearly scaled width

None of the ten million fits performed to data distributed according to the spleen TAC using a linearly scaled width failed to converge in the allowed time. The histogram of the ratios of the fitted area to the true area, shown in Figure 5.34, is broader than the histogram for a constant width but is still centred near one. As shown in Figure 5.35 the distributions of the values of the fit parameters around the true values are broader than those for the fits with a constant width. The peak of the distribution of the fitted t_1 values is also below the true value. Figure 5.36 shows 2D histograms of the fit parameters. As expected these are centred on the true values of the parameters.

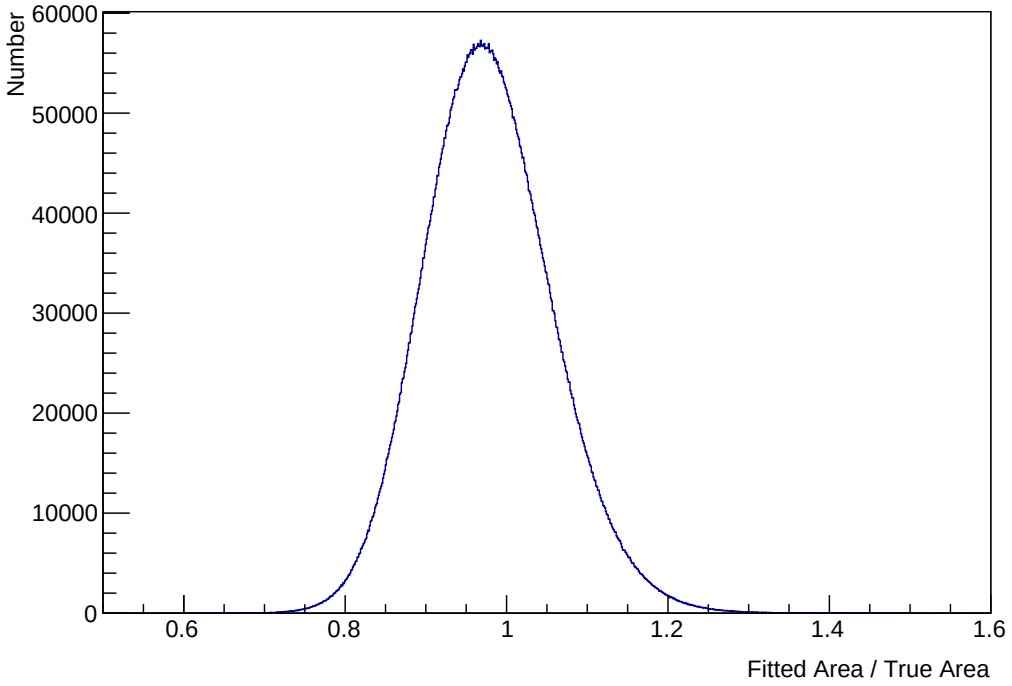

FIGURE 5.34: A histogram of the ratio of the area under the fitted curve and the area under the true curve for the spleen using Equation (5.8) and a linearly scaled width. The main peak of the histogram is around 1.

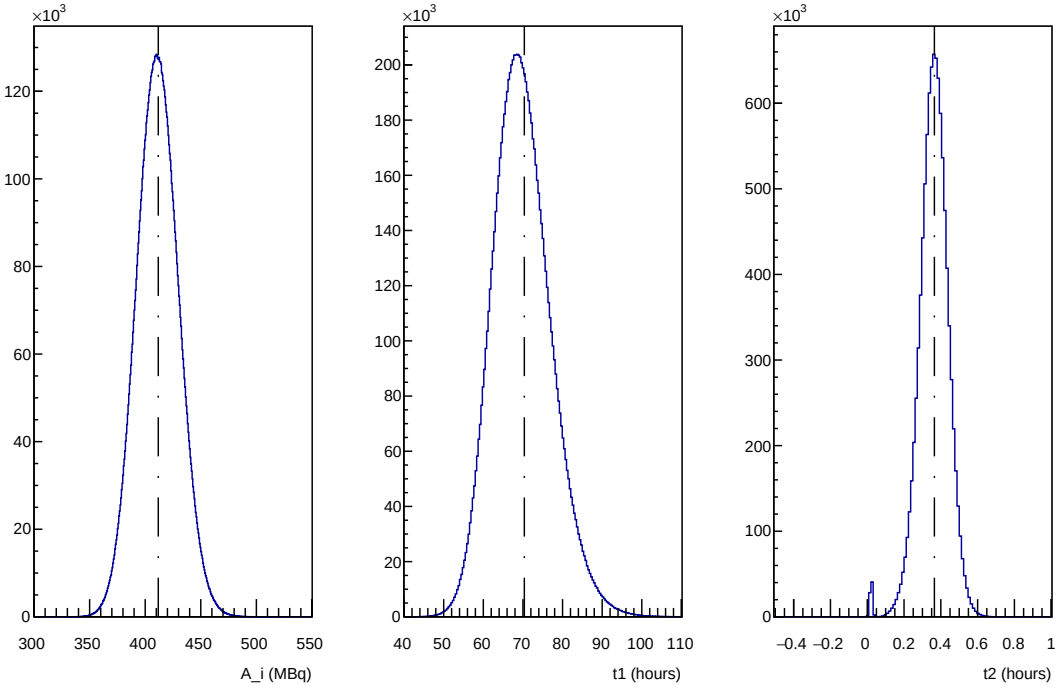

FIGURE 5.35: Histograms of the three fit parameters for ten million fits of the spleen curve using Equation (5.8) and a linearly scaled width. The true value of the parameters are indicated by vertical lines. It can be seen that the histograms are centred on the true values of the parameters.

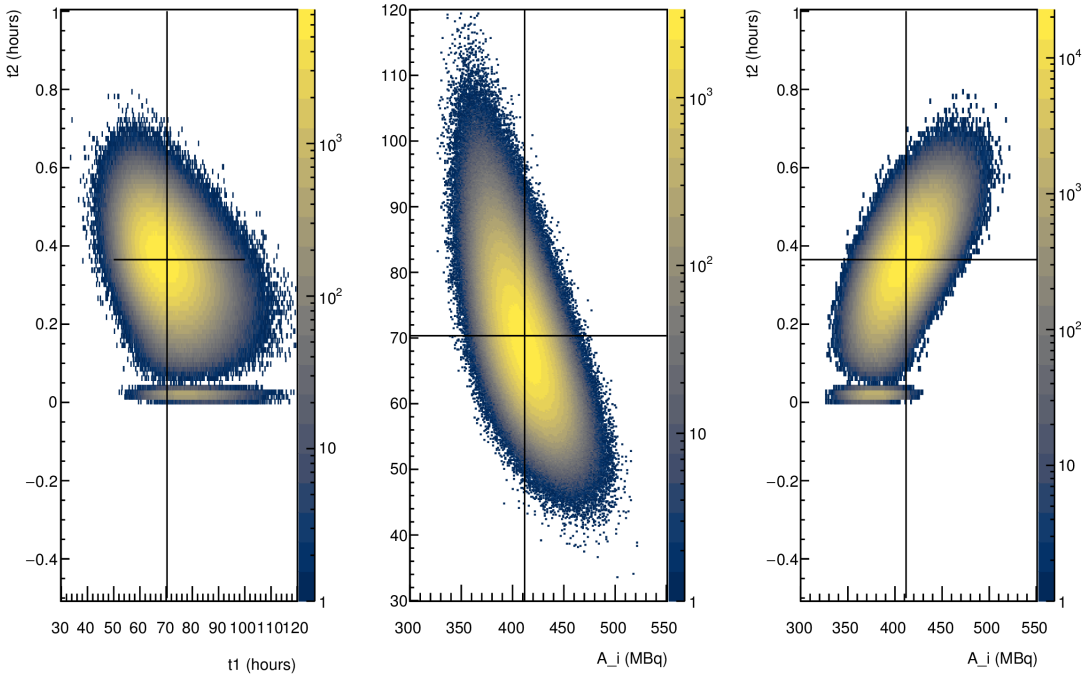

FIGURE 5.36: 2D histograms of the fit parameters for ten million fits of the spleen curve using Equation (5.8) and a linearly scaled width. The true values of the parameters are indicated with black lines. These histograms show the correlation between the fit parameters. Note the logarithmic colour scales.

5.2.5.4 Constant width, multiple functions

A histogram of the ratio of the fitted area to the true area for the spleen TAC using the NUKFIT-style method with a constant width is shown in Figure 5.37. The distribution is roughly Gaussian, but skewed towards higher ratios. The skewness is more evident in Figure 5.38 which shows a histogram of the percentage uncertainty on the fitted area and the ratio. In this case higher ratios lead to larger uncertainties. Figure 5.39 shows the frequency with which functions pass the quality control. As for the other organs functions f_1 anf f_2 pass for all the sets of data points. Function 4_{4a} passes for approximately 20 % of the sets of data points and f_4 passes for roughly 2 % of the sets. Functions f_3 and f_{4b} do not pass for any of the sets of data points.

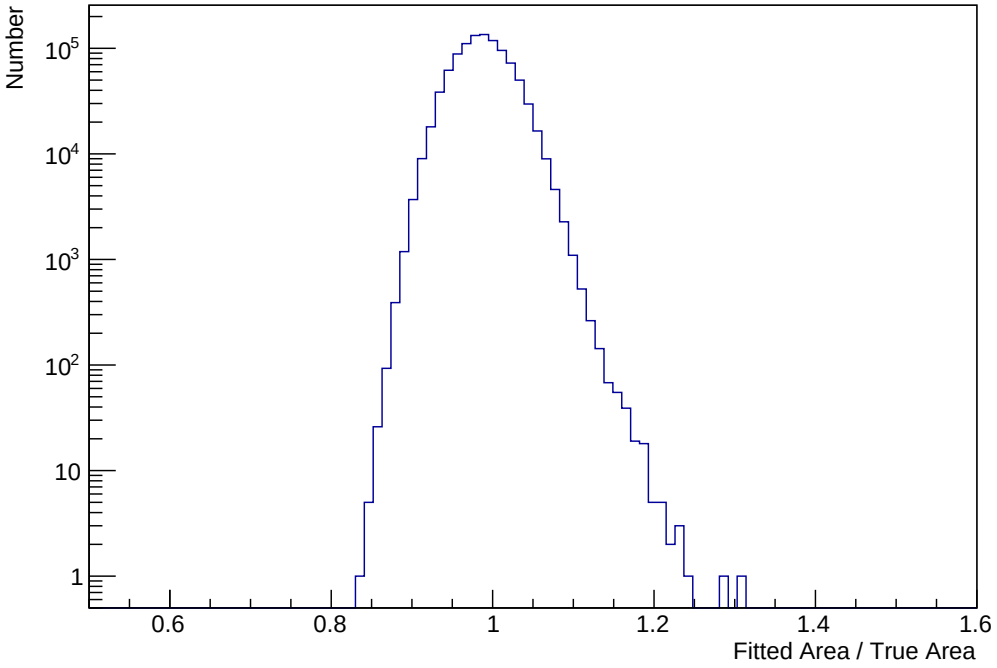

FIGURE 5.37: A histogram of the ratio of the area under the curve and the area under the true curve for the spleen TAC with a constant width using the NUKFIT-style area calculation. Note the logarithmic scale, used to show the small distortion of the distribution.

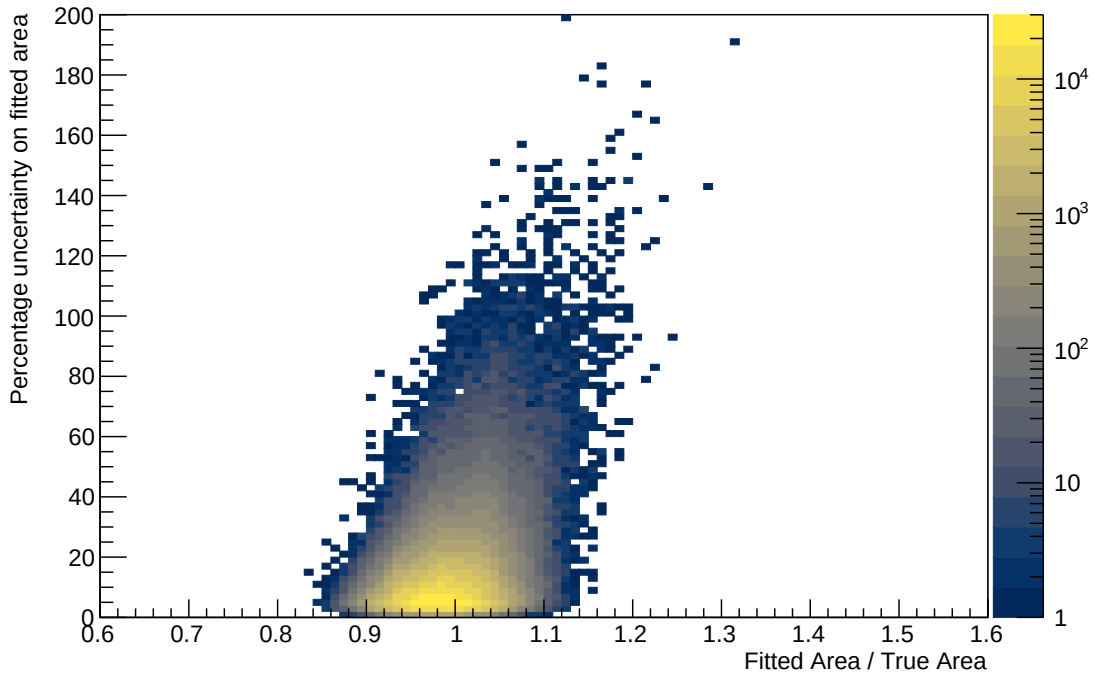

FIGURE 5.38: A histogram of the ratio of the area under the curve and the area under the true curve and the uncertainty on the area for the spleen TAC with a constant width using the NUKFIT-style area calculation. Note the logarithmic colour scale.

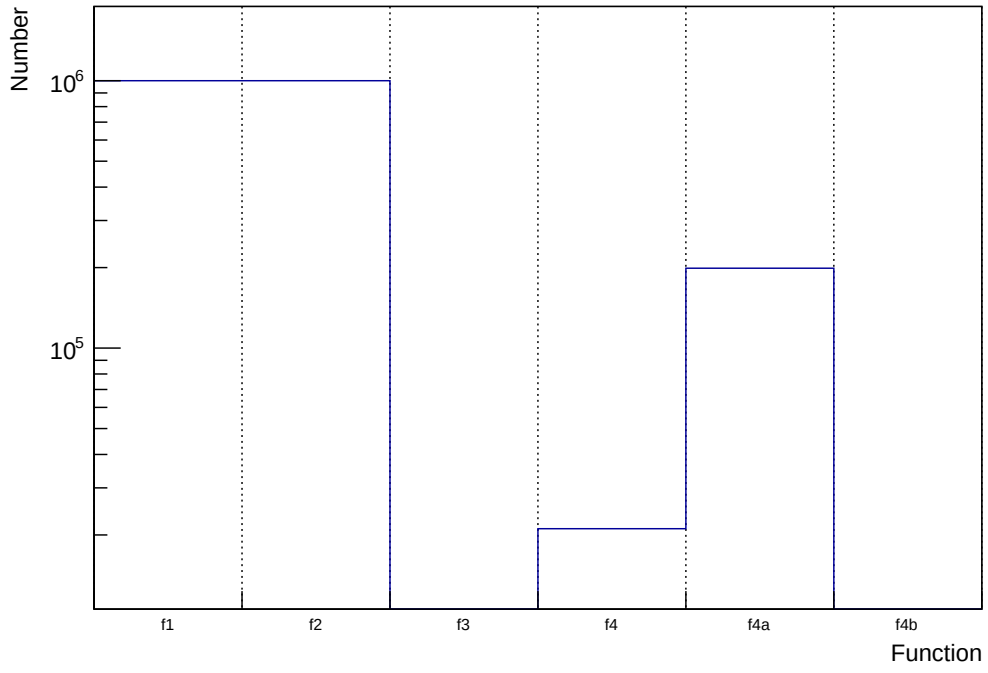

FIGURE 5.39: A histogram showing the frequency of each function passing the quality control for the spleen TAC with a constant width using the NUKFIT-style area calculation. Functions f_3 and f_{4b} never pass the quality control.

5.2.5.5 Linearly scaled width, multiple functions

Figure 5.40 shows a histogram of the ratio between the fitted area under the curve and the true area for the spleen TAC using the NUKFIT-style method with a linearly scaled width. The distribution is clearly not Gaussian, in contrast to that in Figure 5.37. A histogram, in Figure 5.41, of the percentage uncertainty on the fitted area and the ratio shows the possibility of large estimated uncertainty if Gaussian error propagation is used. The frequency with which each function passes the quality control is shown in Figure 5.42. Again, functions f_1 and f_2 pass the quality control for all the sets of data points. Function f_4 passes for roughly the same number of sets, but the fraction for which f_{4a} passes is reduced to approximately 2.5 %. Functions f_3 and f_{4b} again do not pass the quality control for any of the tested sets of data points.

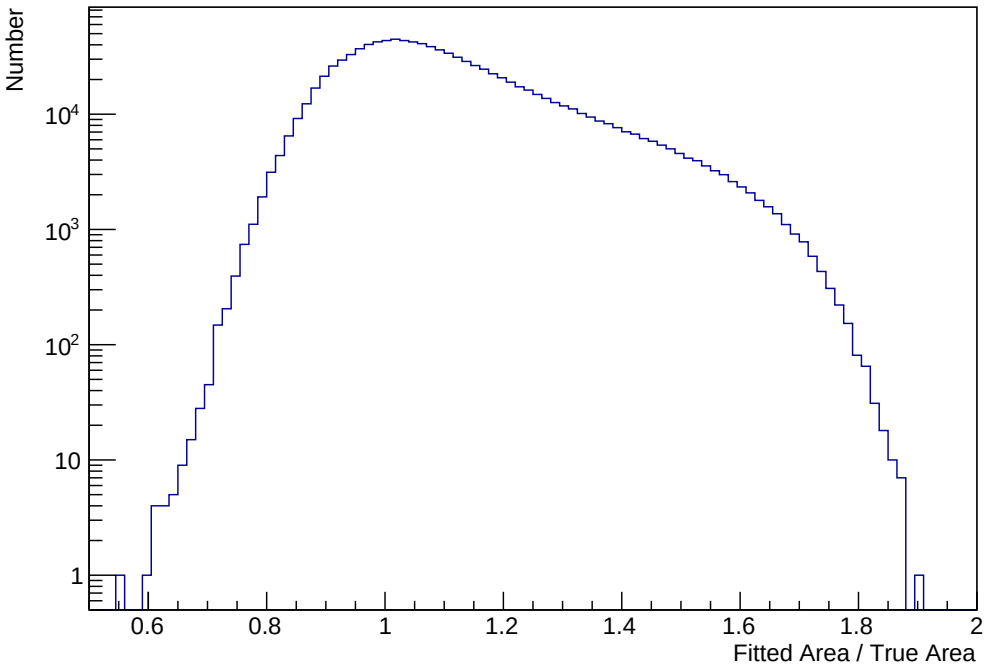

FIGURE 5.40: A histogram of the ratio of the area under the curve and the area under the true curve for the spleen TAC with a linearly scaled width using the NUKFIT-style area calculation. The distribution is broad and asymmetric.

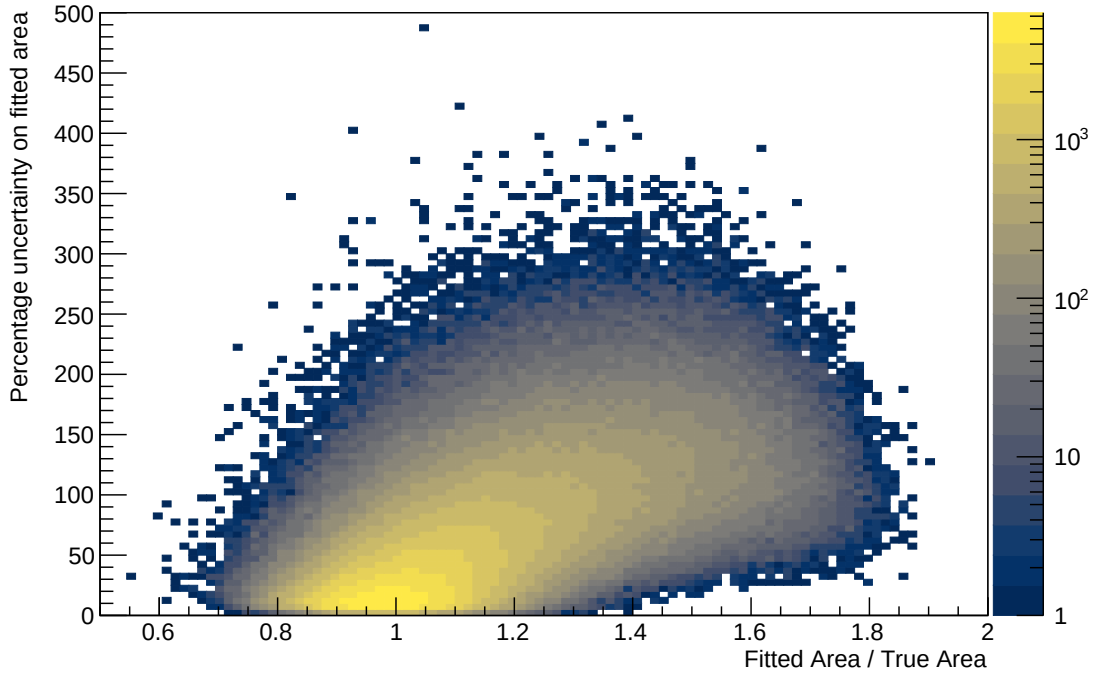

FIGURE 5.41: A histogram of the ratio of the area under the curve and the area under the true curve and the uncertainty on the area for the spleen TAC with a linearly scaled width using the NUKFIT-style area calculation. Note the logarithmic colour scale. It can be seen that an overestimate of the ratio is accompanied with a larger uncertainty.

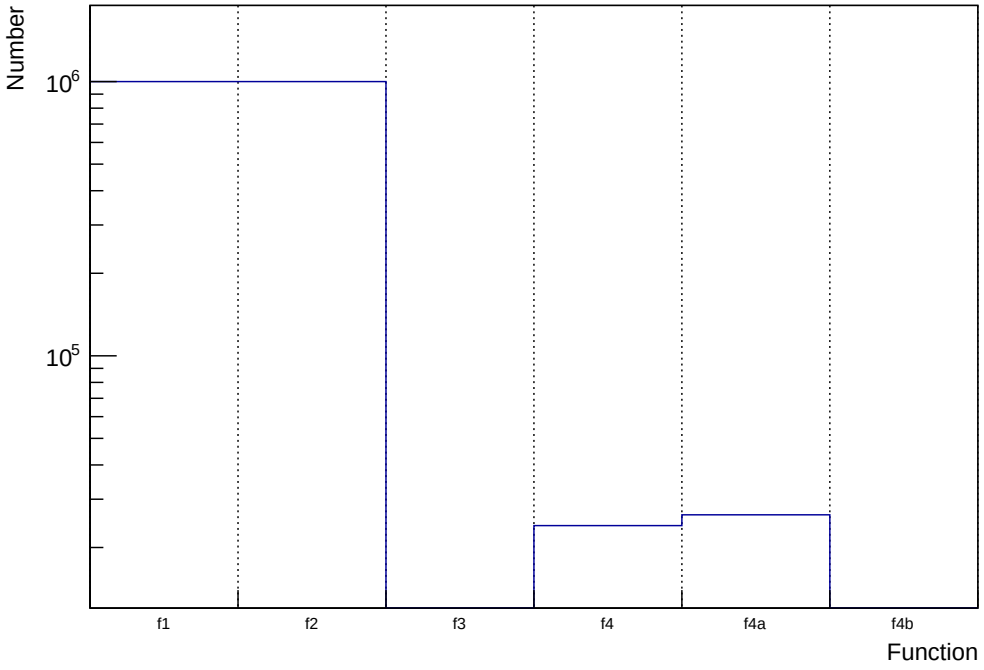

FIGURE 5.42: A histogram showing the frequency of each function passing the quality control for the spleen TAC with a linearly scaled width using the NUKFIT-style area calculation. Functions f_3 and f_{4b} never pass the quality control.

5.3 Calculation of patient-specific S-factors

Patient-specific S-factors for the CATIE patient were calculated for ^{177}Lu and ^{131}I. These were compared to the S-factors used in OLINDA/EXM versions 1.0 and 2.0. The simulations were performed as described in Section 3.3. Patient-specific S-factors for ^{177}Lu were compared with OLINDA/EXM 1.0 in Figures 3.4 and 3.5 in units of dose. These results are presented again in this section with the addition of S-factors from OLINDA/EXM 2.0. The S-factors from OLINDA/EXM versions 1.0 and 2.0 are derived from the output of calculations with the organ masses scaled. No uncertainty information is provided for the S-factors in OLINDA/EXM 2.0 which is problematic as no uncertainty can then be calculated for the final dose. A lower limit of uncertainty can at least be calculated using the other components.

Figures 5.43 and 5.44 show S-factors for gamma and beta emissions from ^{177}Lu from OLINDA/EXM 1.0, OLINDA/EXM 2.0 and the patient specific Monte Carlo simulation. Note the different orders of magnitude for the self and cross S-factors for gamma emissions in Figure 5.43. The S-factors for self-dose from gamma rays are two orders of magnitude smaller than those for self-dose from beta-particles. The S-factors for beta particles are consistent between OLINDA/EXM 1.0 and the patient specific simulation. As discussed in Section 3.5, this is to be expected as beta particles do not travel far enough for the organ morphology to have a large impact on the S-factor. The gamma S-factors are inconsistent for some source-target combinations but are so much smaller that this will have a negligible impact on the total dose. Figures 5.45 and 5.46 show S-factors for gamma and beta emissions from ^{131}I calculated in a similar way. The self S-factors for gamma rays are approximately 20 % of those for beta particles and the cross S-factors for gamma rays are approximately 10 % of the beta self S-factors for adjacent organs. The inconsistencies of the cross gamma S-factors in these cases will have an impact on the calculated total dose to the organs.

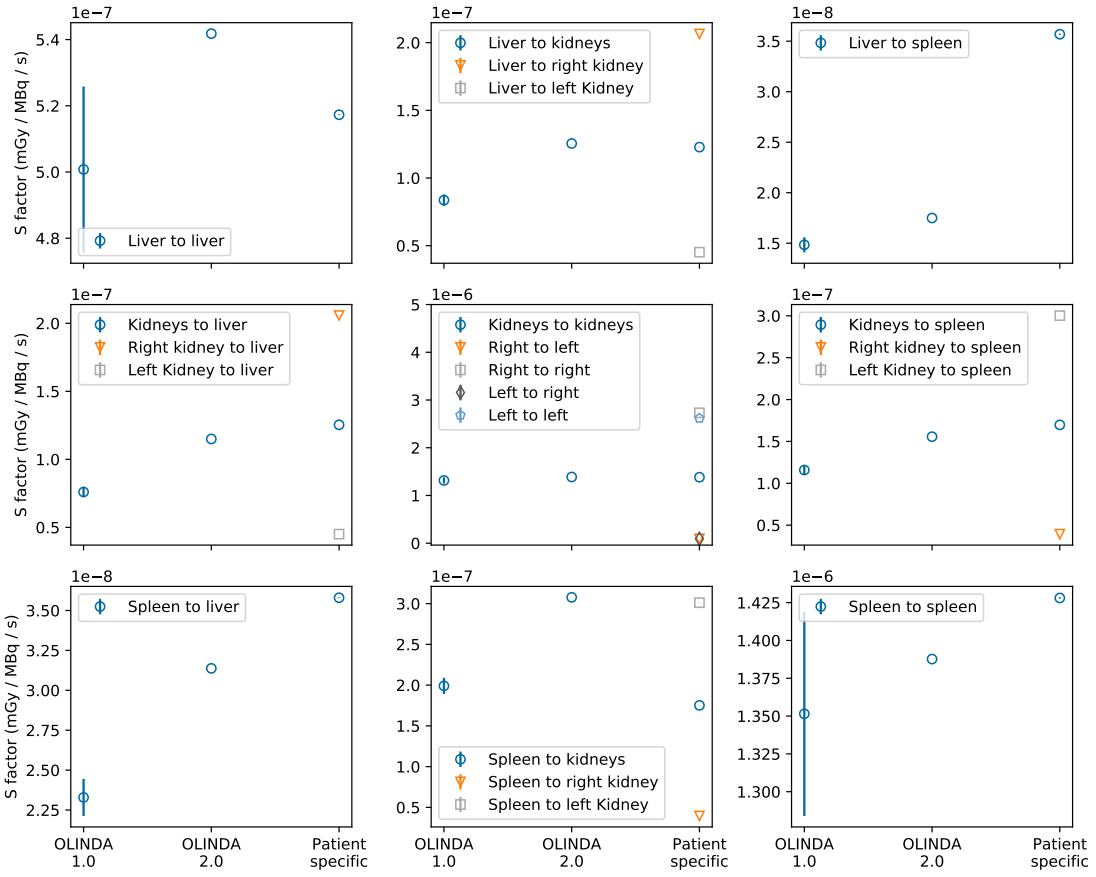

FIGURE 5.43: Figure showing S-factors for gamma rays from ^{177}Lu, from OLINDA/EXM 1.0, OLINDA/EXM 2.0 and a patient-specific Monte Carlo simulation. No uncertainty information is provided for the S-factors used in OLINDA/EXM 2.0. Note the different orders of magnitude for the self- and cross-doses. For some source-target pairs the patient-specific S-factors are not consistent with generic S-factors.

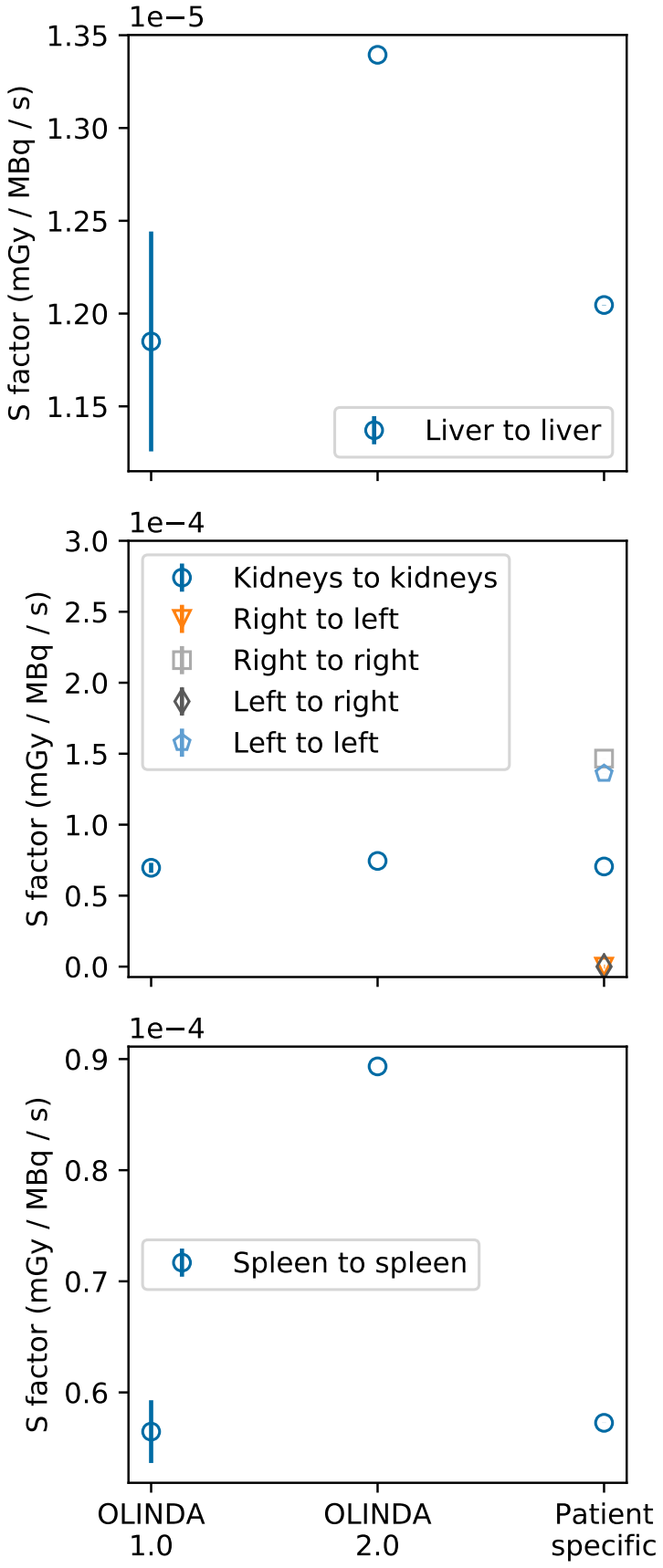

FIGURE 5.44: Figure showing S-factors for beta particles from ^{177}Lu, from OLINDA/EXM 1.0, OLINDA/EXM 2.0 and a patient-specific Monte Carlo simulation. No uncertainty information is provided for the S-factors used in OLINDA/EXM 2.0. The cross S-factors for beta particles are negligible so are not shown. The patient-specific S-factors are consistent with those from OLINDA/EXM 1.0 for all three organs.

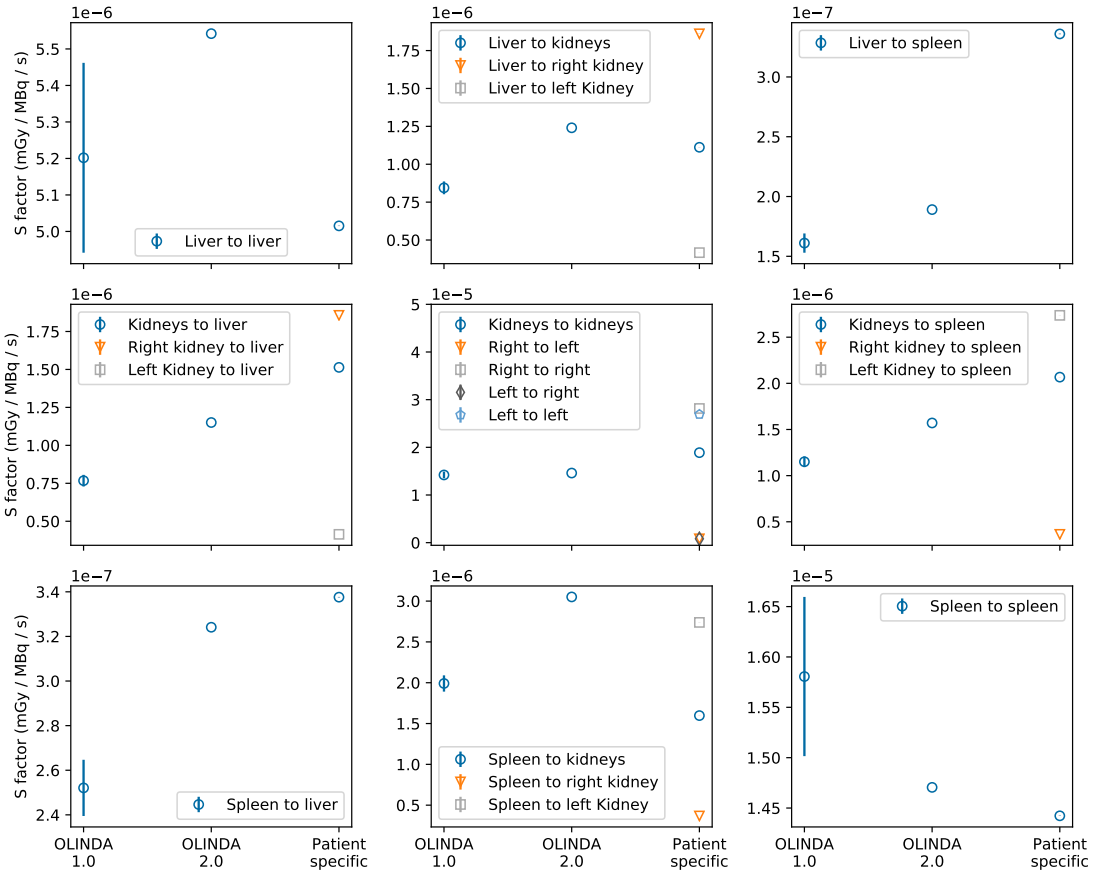

FIGURE 5.45: Figure showing S-factors for gamma rays from ^{131}I, from OLINDA/EXM 1.0, OLINDA/EXM 2.0 and a patient-specific Monte Carlo simulation. No uncertainty information is provided for the S-factors used in OLINDA/EXM 2.0. Note the different orders of magnitude for the self- and cross-doses. For some source-target pairs the patient-specific S-factors are not consistent with generic S-factors.

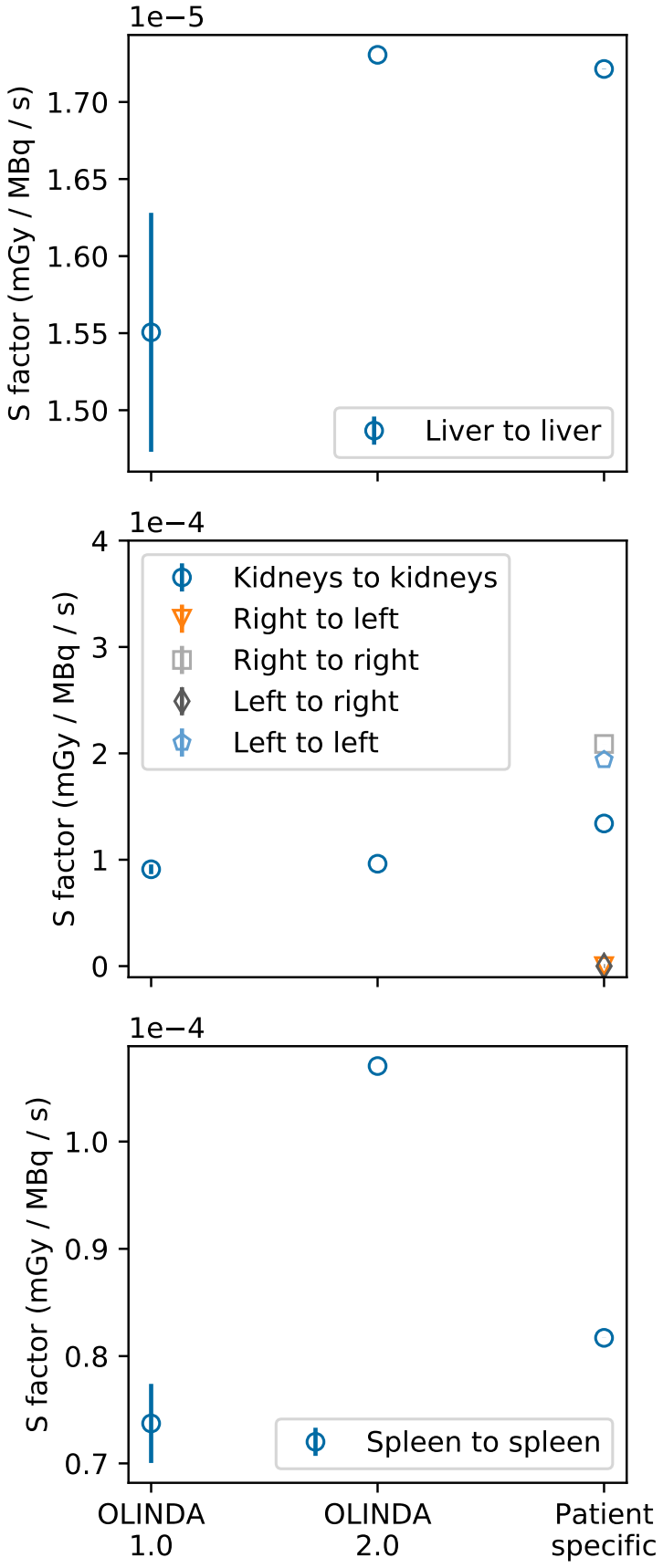

FIGURE 5.46: Figure showing S-factors for beta particles from ^{131}I, from OLINDA/EXM 1.0, OLINDA/EXM 2.0 and a patient-specific Monte Carlo simulation. No uncertainty information is provided for the S-factors used in OLINDA/EXM 2.0. The cross S-factors for beta particles are negligible so are not shown.

5.4 Assessment of impacts on calculated dose

There are two linked problems in the clinical calculation of dose: the closeness of the calculated value to the true value and the uncertainty on the calculated value. It is important to note that the calculated uncertainty may not reflect the closeness to the true value if there are systematic errors. As shown in Figure 3.3 the recovery factors for the liver and spleen are greater than 1.3 when the 113 ml sphere calibration factor is used. This is a systematic offset which is not reflected in the calculated uncertainty. The offset is due to the use of an inappropriate calibration factor. The results in Figure 4.10 show that for the EM2 data the calibration factors for the 113 ml sphere and the CATIE spleen, both positioned centrally, are (13 ± 2.8) % different. The difference between the central sphere and the CATIE spleen positioned anatomically is (23.7 ± 2.5) %. These percentage differences will propagate through to the calculated dose as shown in Equation (5.2). As discussed in Chapter 3, calibration factors of similar volumes are required to give accurate activity quantification. Further work is required to assess how similar the volumes must be and to what extent the shape of the organ must be accounted for. The behaviour of attenuation correction during the reconstruction process must be understood. Assuming that a suitable calibration factor is used, the quantified activities for this patient are within 10 % of the true value with uncertainties of approximately 5 %. These uncertainties are smaller than those suggested as being achievable in reference [10]. However, in clinical practice the uncertainty associated with organ segmentation will be greater than that associated with insert segmentation.

From the plots of the ratios of the area under the fitted curves to the true area, using a single fitting function, for the liver and kidney shown in Figures 5.4, 5.7, 5.16 and 5.19 it can be seen that the PDF of the area under the curve given the PDFs of measurements is not Gaussian. There are secondary peaks or broadening corresponding to a likelihood of overestimating the area under the curve. Describing such distributions using a mean and a width is clearly inappropriate. As a result propagating uncertainties forward from an experimental fit to a single set of data points would be challenging. The histograms of the fit parameters in Figures 5.5, 5.8, 5.17 and 5.20 show that the fits do not reliably converge to the true functions. As such, use of individual fit parameters is not reliable. Directly calculated confidence intervals of the fit parameters for individual sets of data points are highly asymmetric and often contain infinities. Two-dimensional histograms of pairs of fit parameters, shown in Figures 5.6, 5.9, 5.18 and 5.21, demonstrate the correlations between the fit parameters. It can be seen the distributions are far from two-dimensional Gaussian distributions. Clearly fitting a biexponential is not a reliable way to calculate the area under the curve and its uncertainty even when a biexponential describes the

distribution of measured points exactly. Using a greater perturbation width results in a broader distribution of areas under the fitted curves and fit parameters.

The histogram of ratios of areas under the curve for the fits for the spleen with the fitting function defined in Equation (5.7), shown in Figure 5.28, shows a peak centred on one with a secondary peak near 0.7. While this is a more successful estimate of the area under the curve, histograms of the fit parameters in Figure 5.29 show that it is unlikely that the fit will converge to the correct values. Two dimensional histograms of pairs of the fit parameters, in Figure 5.30, show that the correlations between the parameters are far from two dimensional Gaussian distributions. The fits of this functional form involving uptake were not constrained to be positive for all time, resulting in un-physical fits being possible. This can be resolved by using a different functional form or introducing more constraints to the fitting process.

Using the function in Equation (5.8) to fit the spleen curve is more successful. The histograms of the ratios of fitted area to true area, shown in Figures 5.31 and 5.34, are roughly Gaussian when a constant and time dependent perturbation width are used. One dimensional histograms of the fit parameters show single peaks centred on the true values of the fit parameters. However in two dimensional histograms of pairs of the fit parameters, shown in Figures 5.33 and 5.36, distortions are visible.

In the histogram of the ratios of the fitted areas and true areas for the liver curve using the NUKFIT method with a constant perturbation width, shown in Figure 5.10, it can be seen that the shape of the distribution is still not Gaussian. The distortion is however small, and it is unlikely that a set of data points will give an overestimation of the area under the curve. The percentage uncertainty was calculated on the fitted area under the assumption that the covariance matrix was usable and that Gaussian error propagation could be used. It can be seen that there is correlation in the distribution of area and percentage uncertainty, shown in Figure 5.11, and that it is possible to overestimate the area under the curve but calculate a small uncertainty. In Figure 5.12 it can be seen that functions f_1 and f_2 pass the quality control criteria for every set of data points. Function f_4 passes the criteria approximately 1 % of the time. Function f_3 passes approximately 0.5 % of the time and function f_{4a} passes only approximately ten times. Function f_{4b} never passes. Similar behaviour is seen when the perturbation width is time dependent. In Figure 5.13 the distribution of areas is broad. The likelihood of overestimation is still small. The histogram of area ratio and percentage uncertainty in Figure 5.14 shows an increased likelihood of large uncertainties, along with the same problem that an overestimates of area may have small uncertainties. It can be seen in Figure 5.15 that functions f_1 and f_2 pass the quality control for all the generated sets of points. With the

time dependent perturbation width more sets of data points result in function f_3 passing the quality control.

For the kidney fits with a constant perturbation width the distribution of areas, shown in Figure 5.22, again shows an increased likelihood to overestimate the area. The height of the distribution above 1.2 is greater for the kidney than for the spleen. There is a similar correlation to that for the liver in the histogram of the area ratio and the percentage uncertainty, shown in Figure 5.23. As for the liver there is a possibility of overestimating the area and calculating a small uncertainty. There is a greater likelihood of calculating a large uncertainty compared to the liver. Unlike the liver function f_3 is more likely to pass the quality control than function f_4, as shown in Figure 5.24. When the perturbation width is scaled with time the distribution of areas broadens as shown in Figure 5.25. The correlation in the histogram of the area ratio and the area under the curve, shown in Figure 5.26, is similar to that with a constant perturbation width but with an increased likelihood of large uncertainties. Both functions f_3 and f_4 are more likely to pass the quality control as shown in Figure 5.27.

For the spleen fits with a constant perturbation width the distribution of area ratios is closer to a Gaussian, as shown in Figure 5.37. The histogram of the area ratio and percentage uncertainty, in Figure 5.38 shows an increase in uncertainty as the ratio increases. The distribution is however still skewed towards overestimation. The data in Figure 5.42 show that functions describing biexponential decay rarely pass the quality control. The monoexponentials, functions f_1 and f_2, pass the quality control for all the sets of data points as shown in Figure 5.39. Function f_{4a}, which describes uptake and then clearance passes the quality control for approximately 20 % of sets of the data points. However, when the perturbation width is scaled with time the distribution of area ratios in Figure 5.40 is broad with an increased likelihood of overestimating the area under the curve. The distribution of area ratios and percentage uncertainties in Figure 5.41 reflects this but does not have the same correlation as the liver and spleen. Increased areas do have larger uncertainties. In Figure 5.42 it can be seen that function f_4 passes the quality control approximately 1 % of the time. Function $f_{4\mathrm{a}}$ is less likely to pass the quality control than for the data sets with a constant perturbation width.

The overestimates of the area under the curve shown in this chapter are likely due to convergence of the fitting algorithm to a local minimum. Other optimisation methods may avoid this. An alternative strategy is to consider the organs as coupled and fit a compartmental model as discussed in [78].

The provision of uncertainties for S-factors is limited. The uncertainty on the S-factors included in OLINDA/EXM 1.0 is stated to be 5 %, and no information is provided for the S-factors in OLINDA/EXM 2.0. This lack of information makes it difficult to compare

the S-factors in OLINDA/EXM 2.0 to patient specific S-factors. The uncertainty on the S-factors calculated using GATE is small. 150 million decays were simulated in GATE, with the each simulation taking a time of the order of days to run on a desktop machine with an Intel core i7 with a 3.6 GHz clock speed. It has been shown in Section 5.3 that the cross S-factors are only important if the isotope in question has a major gamma emission. It can be seen in Figures 5.44 and 5.46 that for the beta component of dose the S-factors in OLINDA/EXM 1.0 are consistent if mass scaling is applied. For the spleen and liver with ^{177}Lu and the spleen with ^{131}I the OLINDA/EXM 2.0 beta S-factors are not consistent within the uncertainties on the patient-specific simulation. Depending on the uncertainties on the S-factors in OLINDA/EXM 2.0 the results may be consistent. The cross S-factors for ^{131}I in OLINDA/EXM 1.0 and 2.0 are generally inconsistent with the patient-specific S-factors. However the cross S-factors are only 10 % of the beta self S-factors for adjacent organs. Differences in cross S-factors of 40 % therefore only result in a change of the overall S-factor and hence dose of 4 %. Using more suitable S-factors is challenging as it is not yet feasible to perform a patient-specific Monte Carlo simulation for all patients. Users must be aware that scaling the density of organs while keeping the volume constant is not always a suitable substitute for changing the volume while keeping the density constant.

5.5 Conclusion

As discussed in Chapter 3 patient specific calibration factors give quantified activities within 10 % of the true activity. For this patient, the C&E calibration factors give similar recovery for the liver and kidneys. The C&E spleen phantom overestimates the activity by more than 20 %. However the calibration factor for the C&E spleen was calculated with the insert positioned centrally. As discussed in Chapter 4 the position of an insert in a phantom can have an impact on the calibration factor. The behaviour of the attenuation correction during a reconstruction must be understood before calibrating images.

The fitting of a biexponential function to data distributed according to a biexponential function did not reliably produce symmetric distributions of areas under the fitted curves. For the liver function, the parameters estimated by the fitting process were not reliable estimates of the true parameters. For the kidney the estimates were more reliable but the correlations between the parameters were still far from symmetric. In both cases the covariance matrix was not a reliable estimate of the confidence intervals on the fit parameters. When the confidence intervals were estimated directly using `lmfit` they were asymmetric and often contained infinities for the 95 % and even 68 % confidence levels. Such fits would not be usable.

For all the curves examined using the NUKFIT style method, the quality control applied does not guarantee a Gaussian distribution of areas under the fitted curve for many possible sets of data points. It should however be noted that the deviations are small so in practice the assumption that the distribution is Gaussian may hold. If the measured points at late times have a larger error than those at early times the problems are increased. Further work is required to assess whether additional quality control criteria would improve the results. For a set of data points it is possible to estimate the confidence intervals by varying parameters in turn rather than using the covariance matrix. It is possible that this could be used as the basis for further quality control. Alternatively a fitting method other than non-linear least squares could be used.

Generic S-factors as used in OLINDA/EXM 1.0 are shown to be suitable for the patient considered if the radiation dose is dominated by beta particles and mass scaling is used. The S-factors used in OLINDA/EXM 2.0 are not suitable for this patient. If gamma rays are a significant source of the radiation dose, then generic S-factors are not appropriate for this patient.

Quantification of the activity distribution at each time point has been demonstrated to result in a deviation from the true value and uncertainty of a few percent, provided a suitable calibration factor is used. If an unsuitable calibration factor is used, the calculated uncertainty in the quantified activity may not represent the accuracy of the calculated value. Over-estimations of activity of up to 35 % were observed. Fitting time activity curves in a manner which allows further propagation of the uncertainty on the area under the curve is challenging. If the dose resulting from an isotope is mostly due to beta particles, the S-factors are not a major source of error. However the uncertainty on the calculated dose may not be available. If the dose has a significant gamma component then patient-specific S-factors result in a lower error in the dose.

Chapter 6

Summary and conclusions

6.1 Summary

This thesis has examined the impact of patient geometry on quantitative SPECT and radiation dosimetry. The uncertainties associated with the stages of the clinical dosimetry chain were assessed. Chapter 3 discussed the use of 3D printed patient-specific organ models and patient-specific dosimetry. The 3D printed models were used to calculate patient-specific calibration factors for the liver, spleen and both kidneys. The inserts were assembled in a patient-representative phantom and imaged using a clinical SPECT system. The activity in the organs in these images was quantified using calibration factors for a 113 ml sphere, a mathematical organ model and the patient-specific organ model. All three calibration factors were suitable for the kidneys. The calibration factor for the 113 ml sphere was unsuitable for the liver while the organ- and patient-specific calibration factors were suitable. For the spleen only the patient-specific calibration factor was suitable. However a positional dependence of calibration factor was observed, which was discussed in detail in Chapter 4. The use of a calibration factor for an inappropriate shape and volume was shown to result in over-estimations of the activity in an organ of up to 35 %. In this case the uncertainty on the recovery factor was only approximately ±5 %. These over-estimations will remain even if the uncertainty in the calculation of the calibration factor is reduced. Dose calculations for ^{177}Lu using clinical software and the three calibration factors were compared to the results of patient-specific Monte Carlo simulations. The self-doses were found to be consistent provided a suitable calibration factor was used. The cross-doses were generally inconsistent, but sufficiently small relative to the self-doses that there was not a significant impact on the total doses. Chapter 4 investigated the origin of the observed positional dependence of calibration factor. A combination of Monte Carlo simulation and experimental imaging was used to isolate

possible causes of the effect. SPECT images were reconstructed on two different systems to see if the effect was platform dependent. The cause of the positional dependence was found to be the attenuation correction during the reconstruction process. The dependence was observed using the manufacturer specific system, GE Xeleris, for both ^{177}Lu and ^{99m}Tc images. No positional dependence was observed using a manufacturer independent system, Hermes HybridRecon. It should be noted that a similar dependence for different combinations of scanner and reconstruction platform has been reported in the literature.

The uncertainties and errors in the clinical dosimetry chain were discussed in Chapter 5. First the difficulties inherent in the fitting of biexponential functions using non-linear least squares were discussed, and the impact on calculating the area under artificial sets of data points. The refitting of a biexponential function was found not to be reliable. A strategy of fitting multiple functions, similar to that used in the NUKFIT code was assessed. This strategy provided improved results, but does not eliminate the problems of asymmetric probability distributions of the areas under the fitted curves. In practice the improvements may be sufficient to allow the uncertainty on the area under the curve to be calculated. Patient-specific S-factors for ^{177}Lu and ^{131}I were then discussed. Most of the radiation dose from ^{177}Lu is due to beta particles and so the self-dose is the dominant component. As such, the organ shape has little impact on the total dose and generic S-factors are suitable provided they are scaled based on the organ mass. The gamma rays emitted from ^{131}I are sufficiently high energy that the gamma self S-factor is approximately 20 % of the beta self S-factor. The range of gamma rays in tissue is such that the shape of the organ matters and mass scaling alone is not sufficient to correct generic S-factors. The provision of uncertainty information for the S-factors used in commercial systems is a challenge if the uncertainty in the final dose is to be calculated.

6.2 Outlook

The work in Chapter 3 demonstrated the benefits of using organ- or patient-specific calibration factors for a particular patient. Clearly further work is required to understand how these results generalise to patient populations. Similarly the degree of patient specificity needed for S-factors needs to be understood. Multiple clinical reconstruction systems have been shown in Chapter 4 of this work and in reference [64] to apply attenuation correction in an inconsistent manner. While it is possible to correct for this behaviour with a position dependent calibration it is preferable to avoid introducing more complexity to calibration.

The difficulties involved in fitting summed exponential functions as used in nuclear medicine were examined in Chapter 5. This work has only examined data distributed

according to a biexponential function. In real patients, the TAC will not follow a perfect biexponential curve. Further work is required to understand the best method of determining the area under such a curve. A metric is required to assess the suitability of using the covariance matrix for a particular fit. Work has also been reported in the literature investigating the use of imaging data and blood measurements to constrain a compartmental model of the body [78]. Such a method provides a way of calculating the area under a TAC while avoiding the fitting of summed exponential functions.

The remainder of this page was intentionally left blank.

Bibliography

[1] Y. Dewaraja et al. "MIRD pamphlet No. 23: quantitative SPECT for patient-specific 3-dimensional dosimetry in internal radionuclide therapy." In: *J. Nucl. Med.* 53.8 (2012), pp. 1310–25.

[2] C. A. Hoefnagel. "Radionuclide therapy revisited". In: *Eur. J. Nucl. Med.* 18.6 (June 1991), pp. 408–431.

[3] B. J. McParland. *Nuclear Medicine Radiation Dosimetry — Advanced Theoretical Principles*. Springer, 2010.

[4] R. S. Lawson. *The Gamma Camera — A Comprehensive Guide*. Institute of Physics and Engineering in Medicine, 2013.

[5] D. L. Bailey et al., eds. *Positron Emission Tomography: Basic Sciences*. Springer, 2005.

[6] *CTRad: Identifying opportunities to promote progress in molecular radiotherapy research in the UK*. National Cancer Research Institute, 2016.

[7] M. Ljungberg et al. "MIRD Pamphlet No. 26: Joint EANM/MIRD Guidelines for Quantitative 177Lu SPECT Applied for Dosimetry of Radiopharmaceutical Therapy". In: *J. Nucl. Med.* 57.1 (2016), pp. 151–162.

[8] M. Garkavij et al. "177Lu-[DOTA0,Tyr3] octreotate therapy in patients with disseminated neuroendocrine tumors: Analysis of dosimetry with impact on future therapeutic strategy". In: *Cancer* 116.S4 (2010), pp. 1084–1092.

[9] J. I. Gear et al. "EANM practical guidance on uncertainty analysis for molecular radiotherapy absorbed dose calculations". In: *Eur. J. Nucl. Med. Mol. Imaging* 45.13 (Dec. 2018), pp. 2456–2474.

[10] M. G. Stabin. "Uncertainties in Internal Dose Calculations for Radiopharmaceuticals". In: *J. Nucl. Med.* 49.5 (2008), pp. 853–860.

[11] P. F. Sharp, H. G. Gemmell, and A. D. Murray, eds. *Practical Nuclear Medicine*. Springer-Verlag London, 2005.

[12] Data Spectrum Corporation.

[13] *NEMA NU 2-2007 Performance measurements of positron emission tomographs.* Standard. 1300 N. 17th Street, Suite 1752, Rosslyn, VA 22209: National Electrical Manufacturers Association, 2007.

[14] N. Calvert. private communication.

[15] T. D. Ngo et al. "Additive manufacturing (3D printing): A review of materials, methods, applications and challenges". In: *Composites Part B: Engineering* 143 (2018), pp. 172–196.

[16] M. A. Miller and G. D. Hutchins. "Development of anatomically realistic PET and PET/CT phantoms with rapid prototyping technology". In: *IEEE Nuclear Science Symposium Conference Record* 6 (2007), pp. 4252–4257.

[17] D. C. Hunt, H. Easton, and C. B. Caldwell. "Design and construction of a quality control phantom for SPECT and PET imaging". In: *Medical Physics* 36.12 (2009), pp. 5404–5411.

[18] J. I. Gear et al. "Development of patient-specific molecular imaging phantoms using a 3D printer". In: *Medical Physics* 41.8 (2014).

[19] M. F. Bieniosek, B. J. Lee, and C. S. Levin. "Technical Note: Characterization of custom 3D printed multimodality imaging phantoms". In: *Medical Physics* 42.10 (2015), pp. 5913–5918.

[20] J. I. Gear et al. "Abdo-Man: a 3D-printed anthropomorphic phantom for validating quantitative SIRT". In: *EJNMMI Physics* 3.1 (2016).

[21] J. Tran-Gia, S. Schlogl, and M. Lassmann. "Design and Fabrication of Kidney Phantoms for Internal Radiation Dosimetry Using 3D Printing Technology". In: *J. Nucl. Med.* 57.12 (2016), pp. 1998–2005.

[22] A. P. Robinson et al. "Organ-specific SPECT activity calibration using 3D printed phantoms for molecular radiotherapy dosimetry". In: *EJNMMI Phys.* 3.12 (2016).

[23] E. Price et al. "Improving molecular radiotherapy dosimetry using anthropomorphic calibration". In: *Physica Medica* 58 (2019), pp. 40–46.

[24] O. Dancewicz et al. "Radiological properties of 3D printed materials in kilovoltage and megavoltage photon beams". In: *Physica Medica* 38 (2017), pp. 111–118.

[25] K. S. Krane. *Introductory Nuclear Physics.* John Wiley & Sons, 1988.

[26] E. Browne and J. Tuli. "Nuclear Data Sheets for A=99". In: *Nuclear Data Sheets* 145 (2017), pp. 25–340.

[27] F. Kondev. "Nuclear Data Sheets for A = 177". In: *Nuclear Data Sheets* 98.4 (2003), pp. 801–1095.

[28] Y. Khazov, I. Mitropolsky, and A. Rodionov. "Nuclear Data Sheets for A = 131". In: *Nuclear Data Sheets* 107.11 (2006), pp. 2715–2930.

[29] M. Berger et al. *XCOM Photon Cross Section Database (version 1.5)*. National Institute of Standards and Technology, Gaithersburg, MD. 2010. URL: `http://physics.nist.gov/xcom` (visited on 04/25/2018).

[30] G. F. Knoll. *Radiation Detection and Measurement*. John Wiley & Sons, 1979.

[31] D. W. Jones, P. Hogg, and E. Seeram, eds. *Practical SPECT/CT in Nuclear Medicine*. Springer, 2013.

[32] S. Webb. *The Physics of Medical Imaging*. Taylor & Francis, 1988.

[33] T. M. Buzug. *Computed Tomography*. Springer, 2008.

[34] GE. *GE Infinia data sheet*. 2006.

[35] R. S. Lawson. "Gamma Camera SPECT". In: *Practical SPECT/CT in Nuclear Medicine*. Ed. by D. W. Jones, P. Hogg, and E. Seeram. Springer, 2013, pp. 47–75.

[36] H. M. Hudson and R. S. Larkin. "Accelerated Image Reconstruction Using Ordered Subsets of Projection Data". In: *IEEE Transactions on Medical Imaging* 13.4 (Dec. 1994), pp. 601–609.

[37] B. F. Hutton, H. M. Hudson, and F. J. Beekman. "A clinical perspective of accelerated statistical reconstruction". In: *Eur. J. Nucl. Med.* 24.7 (July 1997), pp. 797–808.

[38] R. J. Jaszczak et al. "Improved SPECT Quantification Using Compensation for Scattered Photons". In: *J. Nucl. Med.* 25.8 (1984), pp. 893–900.

[39] K. Ogawa et al. "A Practical Method for Position-Dependent Compton-Scatter Correction in Single Photon Emission CT". In: *IEEE Transactions on Medical Imaging* 10.3 (1991), pp. 408–412.

[40] T. Ichihara et al. "Compton Scatter Compensation Using the Triple-Energy Window Method for Single- and Dual-Isotope SPECT". In: *J. Nucl. Med.* 34.12 (1993), pp. 2216–2221.

[41] G. B. Saha. *Physics and Radiobiology of Nuclear Medicine*. Springer, 2001.

[42] W. E. Bolch et al. "MIRD Pamphlet No. 21: A Generalized Schema for Radiopharmaceutical Dosimetry — Standardization of Nomenclature". In: *J. Nucl. Med.* 50.3 (Mar. 2009), pp. 477–484.

[43] W. S. Snyder et al. *MIRD Pamphlet No. 11: 'S', Absorbed Dose per Unit Cumulated Activity for Selected Radionuclides and Organs*. Society of Nuclear Medicine, 1975.

[44] W. E. Bolch et al. "MIRD pamphlet No. 17: the dosimetry of nonuniform activity distributions — radionuclide S values at the voxel level. Medical Internal Radiation Dose Committee". In: *J. Nucl. Med.* 40.1 (Jan. 1999), 11S–36S.

[45] M. G. Stabin and J. A. Siegel. "Physical models and dose factors for use in internal dose assessment". In: *Health Phys* 85.3 (Sept. 2003), pp. 294–310.

[46] M. G. Stabin, R. B. Sparks, and E. Crowe. "OLINDA/EXM: The Second-Generation Personal Computer Software for Internal Dose Assessment in Nuclear Medicine". In: *J. Nucl. Med.* 46.6 (2005), pp. 1023–1027.

[47] M. Stabin and A. Farmer. "OLINDA/EXM 2.0: The new generation dosimetry modeling code". In: *J. Nucl. Med.* 53.supplement 1 (2012), p. 585.

[48] M. Chauvin et al. "Abstract ID: 155 OpenDose: A collaborative effort to produce reference dosimetric data with Monte Carlo simulation software". In: *Physica Medica* 42 (2017). Abstracts of the MCMA2017, pp. 32–33.

[49] M. Cristy and K. Eckerman. *Specific absorbed fractions of energy at various ages from internal photon sources*. Oak Ridge National Laboratory, 1987.

[50] H. Zaidi and G. Sgouros, eds. *Therapeutic Applications of Monte Carlo Calculations in Nuclear Medicine*. Institute of Physics Publishing, 2003.

[51] C. J. Werner et al. *MCNP6.2 Release Notes*. LA-UR-18-20808. 2018.

[52] I. Kawrakow. "Accurate condensed history Monte Carlo simulation of electron transport. I. EGSnrc, the new EGS4 version". In: *Medical Physics* 27.3 (2000), pp. 485–498.

[53] J. Baró et al. "PENELOPE: An algorithm for Monte Carlo simulation of the penetration and energy loss of electrons and positrons in matter". In: *Nuclear Instruments and Methods in Physics Research Section B: Beam Interactions with Materials and Atoms* 100.1 (1995), pp. 31–46.

[54] S. Agostinelli et al. "Geant4 - a simulation toolkit". In: *Nuclear Instruments and Methods in Physics Research Section A: Accelerators, Spectrometers, Detectors and Associated Equipment* 506.3 (2003), pp. 250–303.

[55] G. Santin et al. "GATE: a Geant4-based simulation platform for PET and SPECT integrating movement and time management". In: *IEEE Transactions on Nuclear Science* 50.5 (Oct. 2003), pp. 1516–1521.

[56] R. Brun and F. Rademakers. "ROOT - An Object Oriented Data Analysis Framework". In: *Proceedings AIHENP'96 Workshop, Lausanne, Sep. 1996*. 1997.

[57] R. Gadd et al. *Measurement Good Practice Guide No. 93: Protocol for Establishing and Maintaining the Calibration of Medical Radionuclide Calibrators and their Quality Control*. Tech. rep. National Physical Laboratory, Teddington, Middlesex, United Kingdom TW11 0 LW: National Physical Laboratory, May 2006.

[58] *JCGM 100:2008 Evaluation of measurement data — Guide to the expression of uncertainty in measurement*. Tech. rep. Bureau International des Poids et Mesures, 2008.

[59] B. He and E. Frey. "The impact of 3D volume of interest definition on accuracy and precision of activity estimation in quantitative SPECT and planar processing methods". In: *Phys. Med. Biol.* 55.12 (2010), p. 3535.

[60] M. D'Arienzo and M. Cox. "Uncertainty Analysis in the Calibration of an Emission Tomography System for Quantitative Imaging". In: *Comput. Math. Methods Med.* (2017).

[61] D. Villoing et al. "Internal dosimetry with the Monte Carlo code GATE: validation using the ICRP/ICRU female reference computational model". In: *Phys. Med. Biol.* 62.5 (2017), pp. 1885–1904.

[62] M. Pacilio et al. "Differences among Monte Carlo codes in the calculations of voxel S values for radionuclide targeted therapy and analysis of their impact on absorbed dose evaluations". In: *Med. Phys.* 36.5 (2009), pp. 1543–1552.

[63] A. Parach and H. Rajabi. "A comparison between GATE4 results and MCNP4B published data for internal radiation dosimetry." In: *Nuklearmedizin* 50.3 (2011), pp. 122–133.

[64] J. Wevrett et al. "Development of a calibration protocol for quantitative imaging for molecular radiotherapy dosimetry". In: *Radiat. Phys. Chem.* 140 (2017), pp. 355–360.

[65] E. Price et al. "Positional dependence of activity determination in SPECT". In: *Nucl. Med. Commun.* 40.8 (2019).

[66] A. P. Robinson et al. "The influence of triple energy window scatter correction on activity quantification for ^{177}Lu molecular radiotherapy". In: *Phys. Med. Biol.* 61.14 (2016), pp. 5107–5127.

[67] C. Lanczos. *Applied analysis*. eng. New York: Dover Publications, 1988.

[68] G. A. F. Seber and C. J. Wild. *Nonlinear regression*. eng. Wiley series in probability and mathematical statistics. Wiley, 1989.

[69] F. S. Acton. *Numerical methods that work*. eng. Washington, D.C: Mathematical Association of America, 1990.

[70] D. W. Kammler. "Least Squares Approximation of Completely Monotonic Functions by Sums of Exponentials". In: *SIAM Journal on Numerical Analysis* 16.5 (Oct. 1979), pp. 801–818.

[71] J. M. Varah. "On Fitting Exponentials by Nonlinear Least Squares". In: *SIAM Journal on Scientific and Statistical Computing* 6.1 (1985), pp. 30–44.

[72] J. G. Reich. "On Parameter Redundancy in Curve Fitting of Kinetic Data". In: *Kinetic Data Analysis : Design and Analysis of Enzyme and Pharmacokinetic Experiments*. Ed. by L. Endrenyi. New York: Plenum, 1981.

[73] P. Kletting et al. "Molecular radiotherapy: The NUKFIT software for calculating the time-integrated activity coefficient". In: *Med. Phys.* 40.10 (2013).

[74] G. Glatting et al. "Choosing the optimal fit function: Comparison of the Akaike information criterion and the F-test". In: *Medical Physics* 34.11 (2007), pp. 4285–4292.

[75] K. P. Burnham and D. R. Anderson. *Model Selection and Multimodel Inference: A Practical Information-Theoretic Approach*. eng. 2nd ed. New York: Springer, 2002.

[76] E. Jones, T. Oliphant, P. Peterson, et al. *SciPy: Open source scientific tools for Python*. 2001–.

[77] M. Newville et al. *LMFIT: Non-Linear Least-Square Minimization and Curve-Fitting for Python*. Sept. 2014.

[78] D. Hardiansyah et al. "Time-integrated activity coefficient estimation for radionuclide therapy using PET and a pharmacokinetic model: A simulation study on the effect of sampling schedule and noise". In: *Medical Physics* 43.9 (2016), pp. 5145–5154.